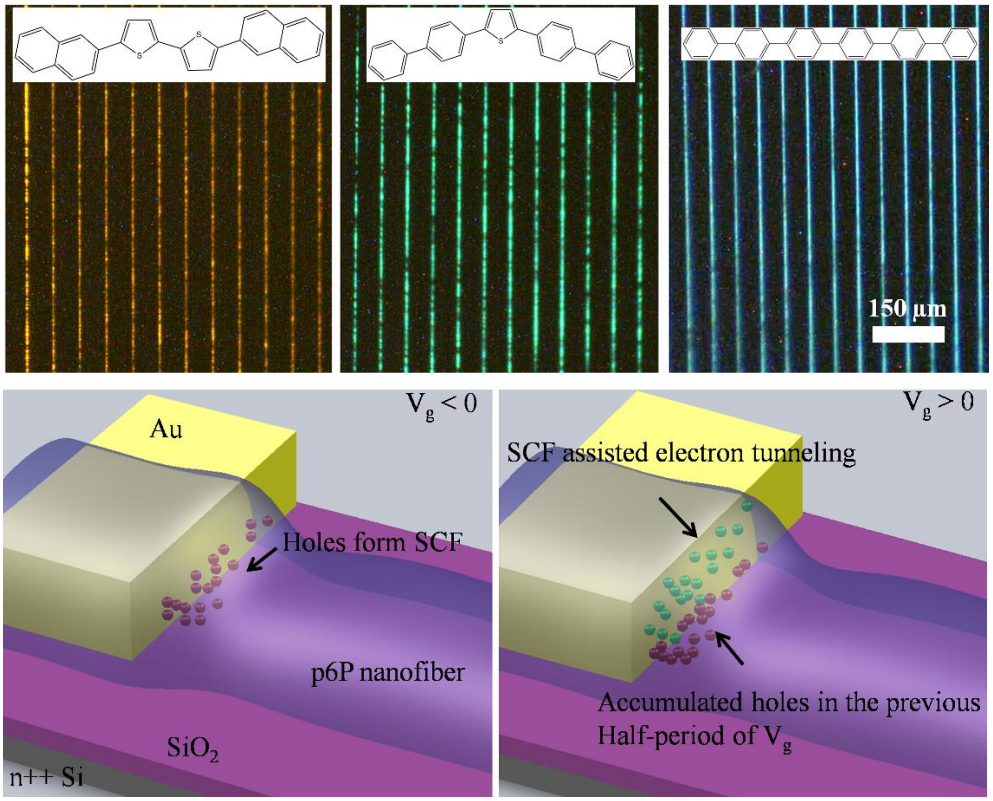

Micro- and nano-scale organic light-emitting devices driven by alternating-current voltage

Ph.D. thesis
NanoSYD
Mads Clausen Institute
University of Southern Denmark

Supervisors:
Assoc. Prof. Jakob Kjelstrup-Hansen
Prof. Horst-Günter Rubahn

Xuhai Liu

March 15, 2013

Front cover image captions

Image 1: Electroluminescence from AC-driven light-emitting transistors based on different organic thin films.

Image 2: Schematic illustration of the operating mechanism of AC-driven light-emitting transistors based on organic nanofibers.

Curriculum vitae

Xuhai Liu was born in 1985 in Qingdao, China. In 2007, he received a Bachelor of Science degree in Mechanical Design and Automation from Northwestern Polytechnical University in Xi'an, China. Afterwards, he came to Denmark to study Embedded Software and one year later shifted his research interest to nanotechnology. In 2009, he received a Master of Science in Engineering degree in Mechatronics from University of Southern Denmark, Sønderborg. He then pursued his doctorate degree in Functional Materials and Nanotechnology in the same research group under the supervision of Assoc. Prof. Jakob Kjelstrup-Hansen and Prof. Horst-Günter Rubahn. His research interests include organic light-emitting devices in a transistor configuration and charge transport properties of organic materials.

Preface

This Ph.D. thesis regarding organic light-emitting devices is based on my theoretical study and experimental research carried out from March 15th, 2010 to March 15th, 2013 at NanoSYD at the Mads Clausen Institute, University of Southern Denmark. During the project period I mainly worked on light-emitting devices based on organic thin films and nanofibers, and also contributed in other experimental investigations with colleagues in our group and visiting international researchers. A number of publications have been made during this project and they are listed in Appendix A.

Apart from the research project, I also took part in other academic activities. Firstly, I succeeded in all the mandatory courses covering 30 ECTS, including two individual courses about microfabrication and computational chemistry. This provided me with solid theoretical background and a better vision of my experimental plan and outcome. Secondly, I contributed in building a probe station for electrical characterization of semiconductor devices, and a vacuum chamber system for thermal evaporation of organic materials. This improved my experimental skills and allowed me to better understand the experimental tools and facilities. Thirdly, I participated in four nanotechnology related conferences and gave one oral presentation and three poster presentations, which provided me with an excellent platform to meet talented researchers from around the world and improve my academic communicating skills. Next, I had two pleasant research stay in Institute of Electrical and Information Engineering of Christian-Albrechts-University of Kiel, and National Center for Nanoscience and Technology (NCNST) of the Chinese Academy of Sciences. During the visiting period, I experienced different research habits and surroundings and it strengthened my capability to quickly adapt to new academic environment. Last but not least, I delivered lectures regarding Elasticity and COMSOL simulation to Master students.

I sincerely hope that this thesis will be helpful for the readers.

Xuhai Liu
NanoSYD, Mads Clausen Institute
University of Southern Denmark
Alsion 2, 6400 Sønderborg, Denmark
March, 2013

Acknowledgements

First and foremost, I would like to thank my project supervisor Prof. Jakob Kjelstrup-Hansen. I have been studying and working under his supervision for four years in terms of experimental work and theoretical discussion, as well as the preparation of manuscripts for journals. I would not grow into the scientist I am today without him. His example of being sincere, diligent, persistent, meticulous in scientific details has inspired me a great deal. I would also like to thank my main supervisor Horst-Günter Rubahn for helpful and critical discussion and guidance in many aspects of my Ph. D. work. His great personality and academic success will always inspire me to pursue a successful career. Also special thanks should go for the visiting professor, Henri Boudinov, from UFRGS Brazil. It was a pleasant experience to work with him for several months.

I am grateful to other collaborators of journal and conference articles. Dr. Henrik Hartmann Henrichsen helped me a lot with initial experimental setup. Dr. Ivonne Wallmann, Andreas Osadnik and Prof. Arne Lützen from University of Bonn together with our previous group member Dr. Manuela Schiek synthesized and provided important organic materials which are essential to the semiconductor devices in my work. Prof. Jacob Kongsted from Department of Physics, Chemistry and Pharmacy of University of Southern Denmark taught me computational chemistry and helped me in great details regarding the output analysis of Gaussian calculations. Dr. Roana Melina de Oliveira Hansen initially taught me electron beam lithography, and she also assisted me in many aspects of my experimental work. I would also like to thank Mr. Fei Liu, who is currently a Ph.D. student in University of Twente, for his important work on self-assembled monolayer modified organic devices. Many thanks are also due to Mr. Henrik Høyer and Prof. Matti Knaapila from NTNU Norway for the pleasant cleanroom work.

I am also very grateful to Prof. Martina Gerken for allowing me to stay in her research group in Christian-Albrechts-University of Kiel for a short visit. It was my great pleasure to work with her Ph.D. student Christian Kluge on experimental setup and optical measurements. Also, I would like to thank Prof. Chao Jiang from Chinese Academy of Sciences in Beijing for offering me a short visit to his group. A lot of gratitude is due to his colleagues and students, such as Dr. Dexing Li, Nan Ai, and Mr. Yiwei Zhang, Jieze Wang, and Miss Misbah Mirza.

I would like to acknowledge other colleagues in our group for their direct and indirect help. In particular, I wish to thank the technician team, Dr. Kasper Thilsing-Hansen, Mogens Melskens Petersen, and Reiner Hübel for their excellent

maintenance of all the experimental equipment in different laboratories. Also kind thanks are due to our group secretary Ms. Zora Milde for her administrative help.

Finally, I would like to thank my family for their unconditional support and encouragement.

Abstract

Organic optoelectronics has experienced significant development and success both in research and on the market level during the past decade. The concept of optical-to-electrical or electrical-to-optical energy conversion, together with property tunability of organic materials via chemical synthesis as well as advanced micro- and nano-scale fabrication processes on various substrates, enable a great number of novel applications in our daily life. For instance, organic light-emitting diodes (OLEDs) have been widely used in portable consumer electronics and large flat panel displays. Also, the integration of light sources such as OLEDs, and light detectors such as organic phototransistors (OPTs), can enable novel lab-on-a-chip system for medical diagnosis.

The main purpose of this thesis is to describe the result of investigations on novel organic light-emitting devices driven by alternating-current (AC) gate voltage on a transistor platform, as well as to present light detectors based on organic crystals in the same transistor configuration, so as to illustrate the possibility to integrate organic light sources and detectors in micro- and nano-scale devices.

Organic small molecule-based thin films were mainly used as the active materials to study the charge carrier injection, transport and light generation mechanism on a micro-scale transistor platform operated by AC gate voltage. Combining time-resolved experiments, low-temperature investigations as well as corresponding calculations, an operating model mainly involving space-charge field assisted charge carrier injection was proposed. This operating mechanism was subsequently implemented in more crystalline organic nanofiber-based nano-scale transistor platform, and corresponding electroluminescence from these nano-scale devices were obtained.

Density functional theory (DFT) calculations have been carried out to estimate the device properties related to charge transport and photon absorption. Micro-scale OPTs based on organic nanofibers and thin films have been fabricated and subsequently characterized in darkness and under illumination. The obvious superior photoresponsivity of the nanofiber-based OPTs compared with thin film OPTs demonstrates that nanofibers have great potential for high-performance photosensitive devices, mainly attributed to the highly ordered molecular packing in the crystalline structures.

Dansk resumé

Organisk optoelektronik har oplevet en betydelig udvikling og succes både i forskningsverdenen og på markedsniveau i løbet af det seneste årti. Konceptet om optisk-til-elektrisk eller elektrisk-til-optisk energi konvertering kombineret med muligheden for at tilpasse egenskaberne af organiske materialer ved kemisk syntese samt avancerede mikro-og nano-skala fremstillingsprocesser på forskellige substrater muliggør et stort antal nye applikationer i vores daglige liv. For eksempel har organiske lysdioder (OLED) været meget anvendt i bærbar forbrugerelektronik og store fladskærme. Desuden kan integration af lyskilder såsom OLED'er og lysdetektorer såsom organiske fototransistorer (OPT) muliggøre nye lab-on-a-chip systemer til medicinsk diagnose.

Hovedformålet med denne afhandling er at beskrive resultatet af undersøgelser af nye organiske lys-udsenende komponenter drevet af vekselspænding (AC) på gate-kontakten af en transistor platform, samt at præsentere lysdetektorer baserede på organiske krystaller i en lignende transistor-konfiguration for at illustrere muligheden for at integrere organiske lyskilder og -detektorer i mikro-og nano-skala enheder.

Organiske tyndfilm baserede på små molekyler blev hovedsagelig benyttet som det aktive materiale til at undersøge ladningsbærer-injektion og -transport og mekanismen hvorved lys bliver genereret på en mikroskala transistor platform drevet af en AC gatespænding. Ved at kombinere tidsopløste eksperimenter, lav-temperatur undersøgelser samt tilsvarende beregninger blev en model udviklet, som hovedsageligt involverer et rumladningsfelt som bidrager til ladningsbærerinjektion. Den virkningsmåde blev efterfølgende implementeret i mere krystallinske, organisk nanofiber-baserede, nano-skala transistorer, og tilsvarende elektroluminescens fra disse nano-skala komponenter blev opnået.

Density Functional Theory (DFT) beregninger er blevet udført for at vurdere komponentens egenskaber relateret til at ladningstransport og foton-absorption. Mikro-skala OPT'er baseret på organiske nanofibre og tyndfilm er blevet fremstillet og efterfølgende karakteriseret både i mørke og under belysning. Den væsentligt højere fotoresponsivitet af de nanofiber-baserede OPT'er sammenlignet med tyndfilm OPT'er viser, at nanofibrene har et stort potentiale som højtydende lysfølsomme komponenter, hvilket primært tilskrives den meget ordnede molekylære pakning i de krystallinske strukturer.

Contents

Abbreviations

6T	Sexithiophene
AC voltage	Alternating-Current voltage
ADF	Amsterdam density functional
AFM	Atomic force microscope
Alq3	Tris(8-hydroxyquinolinato) aluminum
BC/BG	Bottom Contact/Bottom Gate
BC/TG	Bottom Contact/Top Gate
BPE	N,N´-bis(2-phenylethyl)-perylene-3,4:9,10-tetracarboxylic diimide
CCDs	Charge-coupled devices
CI	Configuration interaction
CMOS	Complementary metal-oxide semiconductor
DC voltage	Direct-Current voltage
DFT	Density functional theory
DZP	Double zeta polarization
EBL	Electron beam lithography
EL	Electroluminescence
EML	Light emitting layer
EQE	External quantum efficiency
F-N	Fowler-Nordheim
HIL	Hole injection layer
HOMO	Highest Occupied Molecule Orbital
HTL	Hole transport layer
ITO	Indium tin oxide
KCL	Potassium chloride
LUMO	Lowest Unoccupied Molecule Orbital
MP2	Second-order Møller-Plesset

NaT	2,5-bis(naphthyl)-thiophene
NaT2	5,5-bis(naphthyl)-2,2′-bithiophene
NaT3	5,5’’-bis(naphtha-2-yl)-2,2’:5’,2’’-terthiophene
ODT	Octadecanethiol
OFET	Organic field-effect transistor
OLED	Organic light-emitting diode
OLET	Organic light-emitting transistor
OPT	Organic phototransistor
OTS	Octadecylchlorosilane
P3HT	Poly-3-hexylthiophene
p6P	Para-hexaphenylene
PFDT	1H,1H,2H,2H-Perfluorodecanethiol
PL	Photoluminescence
PMMA	Poly(methyl methacrylate)
PMT	Photomultiplier tube
PPTPP	2,5-bis (4-biphenylyl) thiophene
PPTTPP	5,5’-di-4-biphenylyl-2-2’-bithiophene
PPV	Poly(*p*-phenylene vinylene)
PTCDI-C8	N,N ´-dioctyl-3,4,9,10-perylene tetracarboxylic diimide
RT	Room temperature
SAMs	Self-assembled monolayers
SCF	Space-charge field
SEM	Scanning electron microscope
TC/BG	Top Contact/Bottom Gate
TTPPTT	4,4’-di-2,2’-bithienylbiphenyl
UV	Ultraviolet

Chapter 1: Introduction

Optoelectronics, which is the study of the electronic devices that source and detect light, constitutes a vibrant research field due to its wide applications and its huge potential to lead to novel devices. The past decades have witnessed a great number of fully commercialized optoelectronic products, which include light-emitting diodes (LEDs) for lighting and as display components, photodiodes as detectors, photovoltaic cells as a renewable energy technology, photomultiplier tubes (PMTs) as ultra-sensitive detectors, charge-coupled devices (CCDs) for imaging, high power laser diodes for industrial machining and so on. Intensive investigations on optoelectronics are continuing, particularly in an attempt for minimization into micro- and nano-scale for more power efficient devices [1-4].

The above mentioned optoelectronic devices are all typically based on inorganic semiconductors, e.g. silicon, germanium, gallium arsenide, etc. In inorganic semiconductors, electrons can be excited from the valence band (formed due to valence electrons bound to atoms) onto the conduction band (formed due to conduction electrons, which can move freely among the atomic lattice) via external stimuli, and these electrons subsequently become free moving charge carriers. The vacancies in the valence band are treated also as free mobile charge carriers, namely holes. The resulting electrons and holes can move as highly delocalized waves, and with mean free paths on the order of three magnitudes higher compared with the lattice constant of the inorganic semiconductor, which can result in charge carrier mobility as high as ~10^3 $cm^2V^{-1}s^{-1}$ [5].

The high charge carrier mobility of inorganic semiconductors is the vital factor to lay the foundation of modern computing era, which requires higher processing speed in complementary metal-oxide semiconductor (CMOS) logic. However, such high charge carrier mobility is not crucial to many optoelectronic applications. For instance, thin-film amorphous silicon (a-Si), which is widely used in current display applications, only possesses a carrier mobility of ~1 $cm^2V^{-1}s^{-1}$ [6]. On the other hand, the inorganic semiconductor-based optoelectronic devices generally require complex processing and fabrication techniques, which result in high product cost, especially in large-area applications [7-8].

Organic semiconductors, which have been improved to have comparable carrier mobility to a-Si, have attracted great research attention due to their potential for more efficient, large-area, low-cost, light weight, and mechanical flexible optoelectronic

devices [9-14]. The organic materials can be roughly classified into small molecules which are mainly deposited by vacuum evaporation [15-16], and semiconducting polymers which are usually solution processed [17-18].

In the consumer market view, organic light-emitting sources, such as OLEDs, have been implemented in various prototypes and commercialized large-area display applications. For instance, Kodak and Sanyo introduced the prototype of a full color display based on white OLED with integrated color filters in 2002. Epson produced a 40 inch OLED display in 2004, demonstrating a serious candidate to replace conventional large-area displays. Sony introduced the world's first OLED television, 11 inch XEL-1, in 2007. Both Samsung and LG showcased their 55 inch super OLED television with full 3D support in 2012. In the small display market, various displays based on less expensive passive-matrix OLED have been integrated into watch, cell phone, walkman, MP3 player, etc. The consumer market can also envisage novel applications, such as 'electronic paper' which integrates flexible and even stretchable optoelectronics [19-21], and bio-compatible devices which can be implemented in the medical field [22-23].

Investigations on organic optoelectronics are continuing to further optimize the device structure and system configuration, to increase the power efficiency, and to explore the integration possibility of different optoelectronic devices. This thesis focuses on the AC-driven OLETs, as well as nanofiber-based OPTs. They act as light sources and detectors, respectively, and they have great potential to be integrated into novel lab-on-a-chip system [24-25]. Since the operating mechanism of OLETs in this project can be regarded as the mixture of OLED and conventional direct-current (DC) voltage-driven OLET, the background information of all these devices are provided in the following introduction. The active organic materials are also elaborated in this section. In this work, we focus on the organic materials based on small molecules. The morphology of the small molecule-based materials can be divided into amorphous-like thin films [26-28] and crystalline nanofibers [29-31].

1.1 Devices

1.1.1 Organic light-emitting diodes (OLEDs)

This thesis focuses on AC-driven light-emitting transistors, and interestingly, the first investigations on electroluminescence from organic materials were also driven by AC voltage in a diode configuration. In 1950s, Bernanose et al. firstly obtained electroluminescence from thin films of acridine orange and quinacrine, which was driven by a high AC field [32-34]. Later in 1963, Pope et.al utilized DC voltage as high as 400 V as well as AC voltage and observed electroluminescence from a thin layer of single crystal anthracene [35]. The requirement of high electric field could be due to unsuitable electrodes used, e.g. silver paste electrode and simple electrolyte

electrode, and the inserted dielectric layer could also be responsible for the strict operating conditions. These first investigations on organic electroluminescence did not draw much research attention, and industrial interests were also lacking due to the high voltage requirement.

The critical breakthrough showing practical importance of OLED was achieved by Tang et al. in 1987 [36]. They initiated the utilization of a transparent hole injection electrode of indium tin oxide (ITO), which was aimed to improve the extraction efficiency of electroluminescence, and the electron injection electrode of magnesium:silver (Mg:Ag) was employed to facilitate the injection of electrons. They also firstly utilized a vapor deposited double layer of small molecule materials sandwiched between the metal electrodes, i.e. aromatic diamine as the hole transporting layer and tris(8-hydroxyquinolinato) aluminum (Alq3) as the electron transporting layer. The properly chosen electrodes and organic materials together with a suitable device configuration enabled an external quantum efficiency of 1%, luminous efficiency of 1.5 lm W^{-1}, and brightness larger than 1000 cd m^{-2} at a driving voltage of below 10 V. This landmark work paved the way for the currently commercialized OLED displays, which are mostly based on small-molecule organic materials.

Instead of small-molecule materials, Burroughes et al. implemented the conjugated polymer poly(*p*-phenylene vinylene) (PPV) as the single active organic layer sandwiched between metal electrodes of bottom indium oxide and top aluminum (Al) in early 1990 [37]. They demonstrated that large-area organic light-emitting displays could be fabricated using the easily prepared solution-processed polymer. This work on polymer OLED was followed immediately by Braun et al. using a soluble derivative of PPV [38-40]. Based on these initial investigations on polymer OLEDs, novel television display fabricated by polymer-printing techniques are nowadays on the verge of becoming fully commercialized [41-42].

The standard OLED structure, both for small-molecule and polymer based devices, consists of the organic material sandwiched between two electrodes with different work functions. Take the polymer OLED for instance, the basic device configuration is illustrated in Figure 1.1. Based on the outcoupling direction of the light, the device configuration can be classified as the bottom emission device (a) and the top emission device (b). In the bottom emission configuration for example, a hole injection layer (HIL) is deposited onto the anode ITO with glass as the substrate. A hole transport layer (HTL) is made on top of the HIL layer, and over the HTL layer is applied the light emitting layer (EML), which also acts as the electron transport layer. A cathode with a low work function is finally prepared on top to provide the electron injection. The easily fabricated bottom emission device normally possess a smaller

external quantum efficiency η_{ext} as a component in a display system, compared with the top emission device [43].

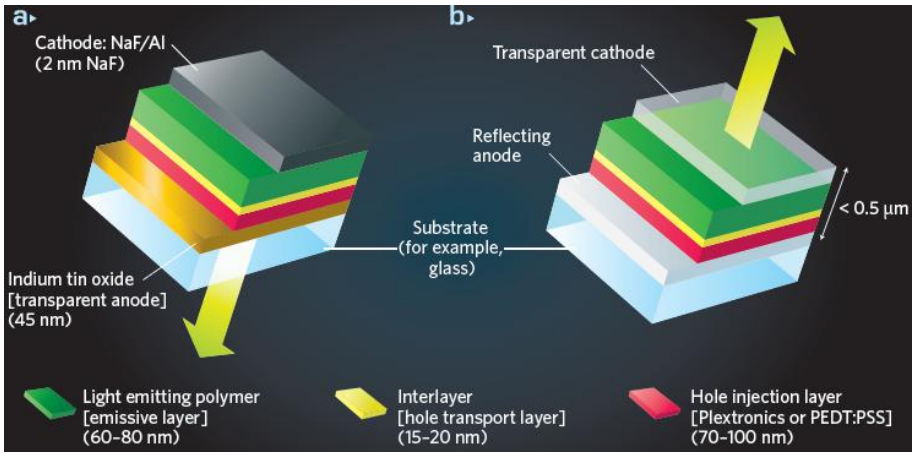

Figure 1.1: Device configuration of a polymer OLED. (a) Bottom-surface emission design. (b) Top-surface emission design. Reproduced from [43].

The external quantum efficiency (EQE) of an OLED can be described by [44]:

$$\eta_{ext} = R_{st} \cdot \gamma \cdot \Phi_{PL} \cdot \Phi_{outc} \qquad \text{Eq. (1.1)}$$

where R_{st} is the singlet to triplet ratio, γ is the charge balance factor, Φ_{PL} is the intrinsic quantum efficiency of radiative decay, Φ_{outc} is the outcoupling efficiency. For fluorescent materials, R_{st} is normally 0.25, because the injection holes and electrons recombine to form singlet to triplet excitons in a ratio of 1:3 and only the singlet excitons can yield fluorescence [45]. Unlike fluorescent materials, phosphorescent materials can make use of both singlet and triplet excited states, which means that the value of R_{st} is not necessary to be considered for phosphorescence [44,46]. Recently, a method for promoting spin up-conversion from triplet states to singlet states was proposed by Adachi et al., and this novel technique involving delayed fluorescence has great potential to break the conventional limit of internal quantum efficiency of fluorescent materials [47-49].

1.1.2 Organic light-emitting transistors (OLETs)

Organic field-effect transistors (OFETs) are usually used as the driving circuit components for OLEDs in the organic active matrix display technology [50-51]. The integration of OFETs normally leads to higher complexity of the components and circuitry. Therefore, OLETs, which combine the electrical switching functionality of OFETs and the light-emitting capability, could simplify the circuit design of an active matrix display system [52-53]. Intensive investigations have been carried out since the report of the first OLET in 2003 [54], and OLETs have recently been shown to outperform OLEDs in terms of efficiency and brightness, mainly because the exciton-charge annihilation and electrode photon losses can be prevented in the

planar transistor configuration illustrated in Figure 1.2 [55]. These advantages of OLETs render them as the potential new components for the next generation of displays.

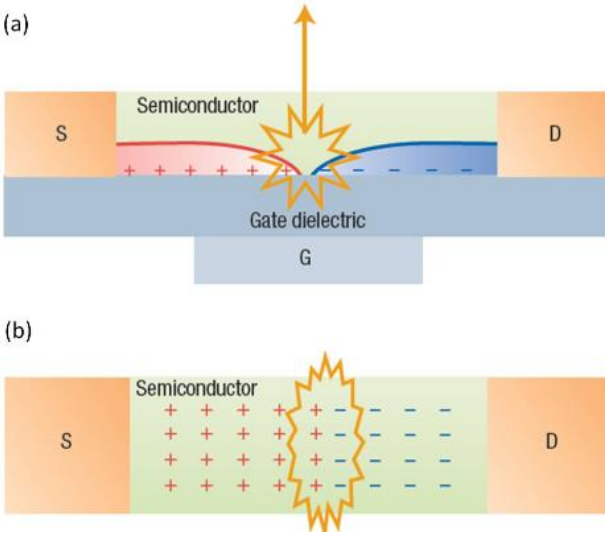

Figure 1.2: Schematic illustration of an OLET in a side view (a) and a top view (b). Reproduced from [52].

The device structure and operating mechanism of a conventional DC-biased OFET should be introduced in the beginning, in order to later present the operation principle of the OLET device. An OFET consists of an active organic material, a dielectric layer and the three electrical terminals, i.e. source, drain and gate electrode. The OFET configuration can be grouped into Bottom Contact/Bottom Gate (BC/BG), Top Contact/Bottom Gate (TC/BG), and Bottom Contact/Top Gate (BC/TG) [53]. This thesis focuses on the BC/BG configuration, as illustrated in Figure 1.3 (a), in which the source and drain electrodes are beneath the active organic materials, hence the designation of Bottom Contact.

In the linear operation regime shown in Figure 1.3 (b), with the biasing of the gate voltage, the charges at the source can inject into the organic semiconductor with an appropriated drain voltage, and the injected charge carries spread over the dielectric/semiconductor interface. When the drain to source voltage V_{ds} is much smaller than the gate voltage V_g, the potential in the channel increases linearly from source (V = 0 V) to drain ($V = V_{ds}$), the drain to source current I_{ds} is proportional to V_{ds}, and I_{ds} is determined by Eq. (1.2).

$$I_{ds} = \frac{W}{L} \cdot C_i \cdot \mu_{lin} \cdot \left(V_g - V_t\right) \cdot V_{ds} \qquad \text{Eq. (1.2)}$$

where W and L are channel width and channel length, respectively, C_i is the dielectric capacitance per unit area, μ_{lin} is the charge mobility in linear operation regime, and V_t is the threshold voltage.

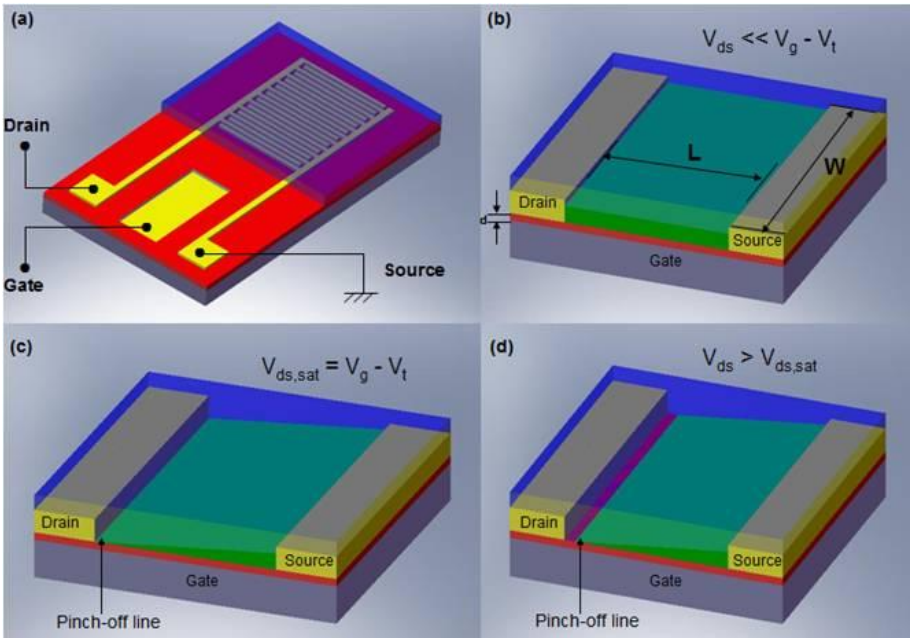

Figure 1.3: (a) Schematic configuration of a BC/BG OFET. (b) Linear regime. (c) Pinch-off at the beginning of the saturation regime. (d) Demonstration of the shift of pinch-off as entering into saturation regime further.

As the drain to source voltage V_{ds} increases further, finally leading to the potential difference between gate and drain being equal to the threshold voltage V_t, a depletion region then forms at the drain electrode, which is illustrated in Figure 1.3 (c). The local potential at the pinch-off line in this case is $V_{ds,sat}$, which equals to $V_g - V_t$.

If the drain to source voltage is further increased, the potential difference between gate and drain will be smaller than the threshold voltage, thus widening the depletion region, which is shown in Figure 1.3 (d). However, the local potential at the pinch-off line remains $V_g - V_t$, therefore the potential difference between this line and the source is unchanged. This is called the saturation regime. The drain to source current in saturation regime can be given by Eq. (1.3).

$$I_{ds,sat} = \frac{W}{2L} \cdot C_i \cdot \mu_{sat} \cdot \left(V_g - V_t\right)^2 . \qquad \text{Eq. (1.3)}$$

The detailed derivations of Eq. (1.2) and Eq. (1.3) are presented in Appendix B. The charge carrier mobility both in linear and saturation regimes can be calculated from Eq. (1.2) and Eq. (1.3), respectively, and this calculation will be introduced in the experimental section.

Based on the main charge carriers presented in the transistor channel, OFETs can be classified into p-type [54] and n-type unipolar transistors [56], as well as ambipolar transistors [53,57]. In unipolar transistors based on a fluorescent material, weak light emission could also be observed in the vicinity of one metal electrode, even though charge carriers of only one polarity dominate the transport along the transistor

channel [54]. This is because charge carriers of another polarity can tunnel through the high injection barrier and contribute to the radiative recombination. However, the output light is normally extremely weak due to the unbalanced charge carrier injection and exciton quenching at the metal electrode. In contrast, the light emission from ambipolar transistors, characterized by the comparable injection and transport of holes and electrons, can be optimized by varying the DC biasing voltage and be obtained in the center of the transistor channel, thus having balanced charge carrier recombination and negligible exciton quenching [53,58].

A novel biasing approach of OLET involving AC gate voltage was demonstrated by Yamao et al., which facilitated clear light emission both from amorphous films and single crystals [59-61]. In their work, the electroluminescence (EL) of the organic materials is assumed to be due to the recombination of holes and electrons injected from the source and drain electrode, respectively, during different half-periods of the AC gate voltage. However, the low resolution of the optical image of the electroluminescence they provided cannot well demonstrate and support their argument that an emission line between metal electrodes should exist due to recombination of the charge carriers injected from separate electrodes.

In contrast, we have demonstrated AC-driven light emission from a BC/BG OLET platform and observed light emission near an individual electrode as well as from both sides of the transistor channel. We revealed a device operating mechanism that combines hole injection and space-charge field (SCF) assisted electron tunneling from an individual metal electrode. Our proposed device operating mechanism can explain well the light emission from a unipolar transistor platform driven by AC gate voltage [62-65]. Similar electroluminescence from AC biased OLET was also reported by Ohtsuka et al. using a BC/TG transistor platform [66]. The detailed investigation is documented in the experimental section, and more discussion on the operation mechanism of AC-driven OLET will be presented later.

1.1.3 Organic phototransistors (OPTs)

In OPTs, in addition to the three terminals of a transistor platform, an external light source can be used as the fourth terminal in OPTs to control the density of photo carriers in the transistor channel, thus integrating electrical switching and light detection into an individual optoelectronic device. The possibility of realizing high sensitivity and low noise photoconductive systems render OPTs as an intensive research target, and various active organic semiconductors and metal/dielectric combinations have been investigated [67-71].

Various factors determine the performance of OPTs, such as the photoresponsivity, the spectrum response, etc. The photoresponsivity is usually denoted as R, and it can be defined as [67]

$$R = \frac{I_{ds,illum} - I_{ds,dark}}{A \cdot P_{inc}} \qquad \text{Eq. (1.4)}$$

where $I_{ds,illum}$ and $I_{ds,dark}$ are the drain-source current under illumination and in darkness, respectively, and A is the effective device area; P_{inc} is the intensity of the incident light. The photoresponsivity determines whether the OPT is an efficient photodetector, which means that a higher value of the photoresponsivity suggests better functionality of the OPT even under a weak illumination. The spectrum response is mainly determined by the intrinsic property of the active organic semiconductor. For instance, OPTs based on materials with small energy gap are only suitable for detecting visible light or infrared light, whereas OPTs based on materials with large energy gap may be also utilized to detect ultraviolet (UV) light. The energy gap will be introduced in the theoretical section later.

The performance of OPTs has been improved significantly. The highest responsivity reported until today observed by Cho et al. was 4300 AW^{-1} under illumination with a light intensity of 7 μW cm^{-2} by using soluble star-shaped oligothiophenes with four-armed π-conjugation paths [72]. Kim et al. reported that the current on-off ratio of a 6,13-bis(pentylphenylethynyl) pentacene-based OPT can be up to 10^7 [73]. However, only few studies in the literature have demonstrated OPTs made of organic crystalline structures [74-75], and particularly, the direct comparison of crystalline materials to amorphous-like thin film-based OPTs is rare [76-77]. Mukherjee et al. obtained 40 times higher photoresponsivity from n-type phototransistors based on solution grown ordered N,N´-dioctyl-3,4,9,10-perylene tetracarboxylic diimide (PTCDI-C8) nanowires compared with thin film-based OPTs of the same material [76]. Yu et al. observed that N,N´-bis(2-phenylethyl)-perylene-3,4:9,10-tetracarboxylic diimide (BPE-PTCDI) nanowire-based n-type OPTs exhibit more than 103 times larger photoresponsivity than that of thin film OPTs at a gate voltage of 50 V [77].

1.2 Materials

1.2.1 Molecules

In this thesis, we focus on small molecules-based organic materials. Among the vast variety of organic semiconductor based on small molecules, acene, phenylene and thiophene oligomers along with their derivatives have been intensively investigated [78-81]. In particular, pentacene is considered to be the organic material with the most outstanding transport properties both for crystalline and amorphous configurations [82-83]. Moreover, thiophene-phenylene co-oligomers [84] and naphthyl end-capped thiophenes [85] are also appealing materials to be applied in optoelectronic devices due to their various intermolecular packing and the ability to self-assembled into nanofibers [86].

Here, different organic oligomers, ranging from acenes, phenylenes, thiophene, thiophene-phenylene co-oligomers to naphthyl end-capped thiophenes, have been listed, and some of them have been chosen as the active organic semiconductor in OLET and OPT devices. Pentacene is treated as the benchmark to evaluate the transfer integral and reorganization energy. Figure 1.4 illustrates the molecular structure of the nine oligomers, namely pentacene, para-hexaphenylene (p6P), sexithiophene (6T), 2,5-Di-4-biphenyl-thiophene (PPTPP), 5,5'-di-4-biphenylyl-2-2'-bithiophene (PPTTPP), 4,4'-di-2,2'-bithienylbiphenyl (TTPPTT), 2,5-bis(naphthyl)-thiophene (NaT), 5,5'-bis(naphtha-2-yl)-2,2'-bithiophene (NaT2), and 5,5''-bis(naphtha-2-yl)-2,2':5',2''-terthiophene (NaT3). They are classified into five categories, i.e. acene, phenylene, thiophene, thiophene-phenylene co-oligomers, and naphthyl end-capped thiophenes, which are presented from Figure 1.4 (a) to (e), respectively.

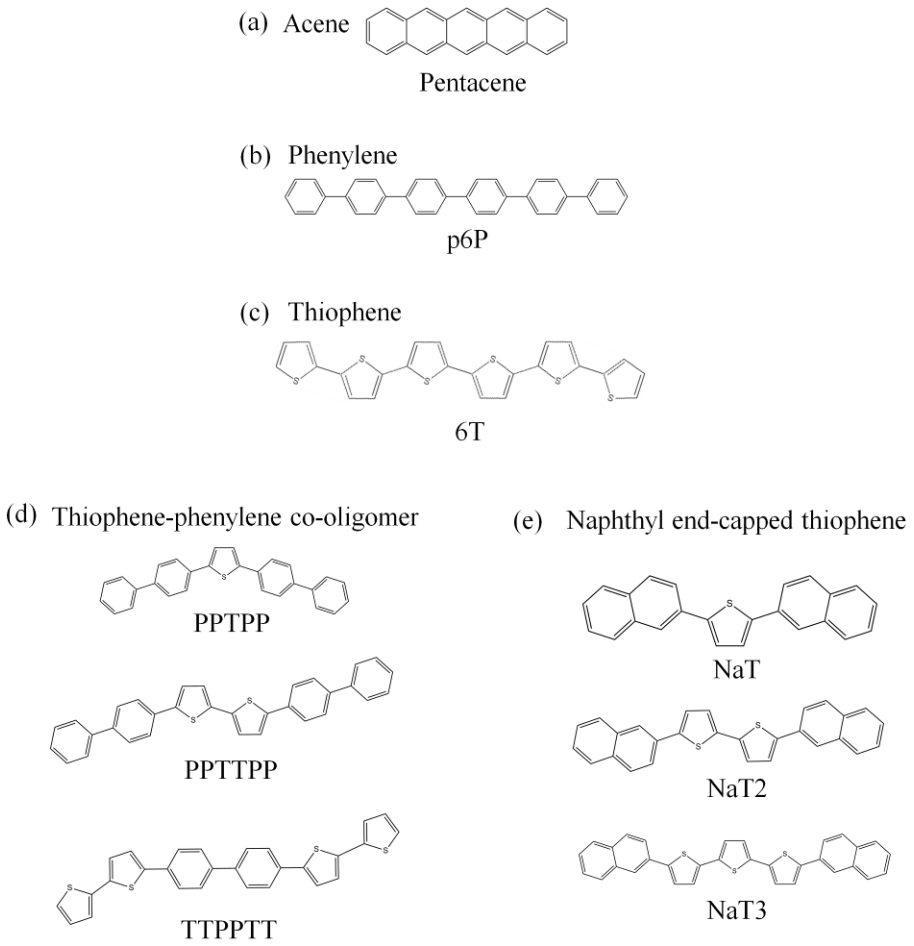

Figure 1.4: Molecular structures of (a) acene, (b) phenylene, (c) thiophene, (d) thiophene-phenylene co-oligomers and (e) naphthyl end-capped thiophenes.

Various optical and electronic properties of the series of the different materials are possible by tuning the backbone structure, e.g., adding or removing a thiophene, replacing two phenylenes with a naphthyl group. Besides, the electronic properties of

the organic crystals are also determined by the intermolecular interactions of oligomers coupled by the van der Waals force. The parameters governing the electronic transport characteristics will be discussed in Section 2.1.4.

1.2.2 Morphology: thin films and nanofibers

The morphology of organic semiconductors is usually the thin film. Organic thin films are normally prepared by thermal vacuum evaporation [27], spin-coating [26] or inkjet printing [28], which can lead to amorphous or semi-crystalline micro structure. It is widely known that the performance of these thin film-based optoelectronic devices can be affected by the presence of grain boundaries, charge carrier traps and defects.

Under certain conditions, the organic materials can exhibit well ordered crystalline structure, such as nanofibers. In contrast to the organic thin films, one-dimensional organic nanofibers possess superior defect-free and highly ordered crystalline micro structure, which are more suitable to be integrated into high-performance micro- or nano-scale optoelectronic devices [29-31]. They can be grown by thermal evaporation of organic small molecules under high vacuum conditions onto specific surfaces, e.g. muscovite mica [29,86] and potassium chloride (KCl) [87]. For instance, coulomb interaction occurs when two p6P oligomers approach to each other, leading to herring bone configuration in p6P nanofibers grown on mica surface, as shown in Figure 1.5.

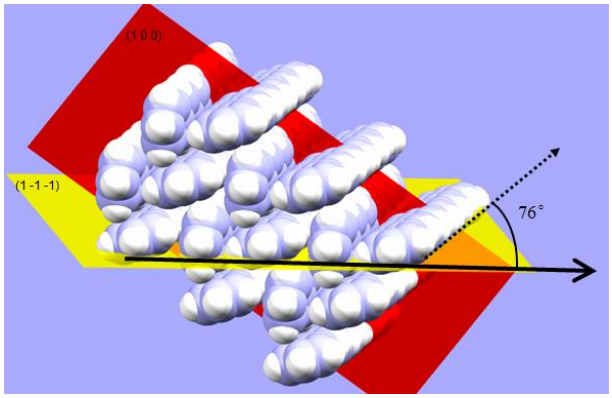

Figure 1.5: A segment of a p6P crystal. Dashed arrow: the axis of a p6P oligomer. Solid arrow: the nanofiber axis. Both of the arrows lie within the (1 -1 -1) plane.

The growing direction of the crystal is not completely perpendicular to the oligomer axis, with an angle of approximately 76 °in between [88]. The dashed arrow indicates the axis of p6P oligomer, and the solid arrow indicates the growing direction of crystal, both of which lie in the (1 -1 -1) plane. Figure 1.5 only illustrates a segment of a p6P nanofiber. Muscovite mica plays an important role in growing ideal p6P nanofibers. For other substrates with reduced interaction with p6P molecules, the molecules tend to stack along the (1 0 0) face, indicated by the red plane in Figure

1.5, resulting in layers of upright molecules [88]. In contrast to such substrates, the surface of muscovite mica has relatively high interaction with p6P molecules due to being positively charged and polar after cleavage. The p6P nanofiber dimension is normally several ten nanometers in height, several hundred nanometers in width and several micrometers in length. A sample with 5nm thick p6P nanofiber emitting polarized light after exposure to UV light is illustrated in Figure 1.6.

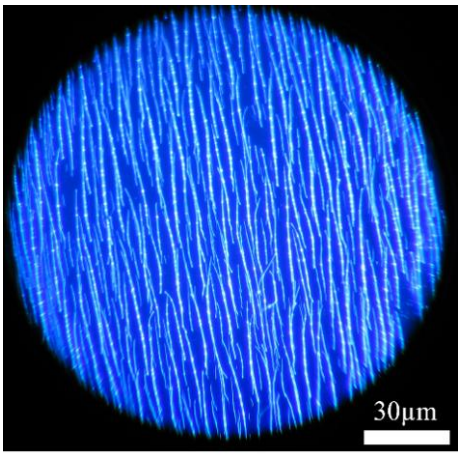

Figure 1.6: Fluorescence microscopic image of 5nm thick p6P nanofibers.

The nanofibers grown on mica surface can be subsequently transferred onto a transistor platform via a roll-over transfer process [89]. Alternatively, the nanofiber-based transistors can be also prepared based on in-situ deposition onto a nano-scale transistor platform under high vacuum conditions [65,90]. The detailed preparing process of the nanofiber-based devices will be elaborated in the experimental section.

1.3 Materials and devices used in this project

In this project, the light-emitting devices (i.e. OLETs) and photosensitive devices (i.e. OPTs) are based on substrates which are in a transistor configuration. The transistor platforms here can be divided into two types, namely micro-scale device platforms and nano-scale device platforms.

The micro-scale device platforms are fabricated using standard optical lithographic technique. The definition of "micro-scale" device is due to the fact that the channel length of these transistors is in the micro range, which is at least 2 µm. In comparison, the effective areas of the nano-scale device platforms are made by electron beam lithography (EBL) leading to transistor channel in sub-micro level. The preparation details of the platforms will be presented in the experimental section.

OLETs have been fabricated based on both of micro-scale and nano-scale substrates. As for the micro-scale OLETs, different types of organic thin films have been implemented: NaT and NaT2 thin films are used for the initial test of the OLETs driven by AC gate voltage; p6P thin films are used to investigate the operating

mechanism of AC biased OLET. Transferred p6P nanofibers have also been applied in the micro-scale OLETs for the initial test. Regarding the nano-scale devices, in-situ grown p6P and 6T nanofibers can bridge across the transistor channel directly due to the narrow sub-micro channel between the EBL fabricated electrodes.

OPTs have been fabricated only on micro-scale substrates, using both of NaT2 thin films and transferred NaT2 nanofibers. NaT2 thin film transistors are treated as the reference to compare with the crystalline nanofiber-based OPT devices.

For clarity, the organic semiconductors in different morphologies implemented in OLETs and OPTs are listed in Table 1.1.

Table 1.1: Organic semiconductors in different morphologies implemented in OLETs and OPTs.

	micro-scale OLET	nano-scale OLET	micro-scale OPT
thin films	NaT, NaT2, p6P,PPTPP	(none)	NaT2
transferred nanofibers	p6P	(none)	NaT2
in-situ grown nanofibers	(none)	p6P, 6T	(none)

1.4 Structure of the thesis

The thesis consists of six chapters, and brief descriptions of each chapter are as follows:

Chapter 1: This chapter has presented an overview of applications of organic optoelectronics, and in particular, OLEDs and OLETs as light sources, as well as OPTs as light detectors are introduced in more details. Afterwards, organic materials based on small molecules, which can form thin films with inferior molecular ordering and crystalline nanofibers as the building blocks of the optoelectronic devices, are described.

Chapter 2: This chapter presents a theoretical description of the charge carrier injection from metal electrodes to organic semiconductors, e.g., space-charge field assisted tunneling. It also provides a computational chemistry view of the molecular orbitals, energy levels and intrinsic charge transport in organic crystals.

Chapter 3: This chapter provides the detailed experimental work of micro-scale OLETs based on organic thin films and transferred nanofibers. It includes optical measurements of OLETs and related electrical measurements of OFETs. An operating mechanism of the AC biased OLETs, which involves space-charge field assisted charge carrier injection is proposed.

Chapter 4: The nano-scale OLETs based on in-situ grown nanofibers have been investigated. The proposed operating mechanism involving space-charge field assisted charge carrier injection can also be applied to nano-scale devices.

Chapter 5: This chapter provides the experimental work of the OPTs based on micro-scale transistor platforms. Both of organic thin films and nanofibers have been implemented as the active organic materials, and the device performance based on the materials with different morphologies has been compared.

Chapter 6: This chapter gives a summary of the theoretical and experimental work presented in this thesis, and it envisions possible improvement and potential novel applications of the organic optoelectronic devices.

Chapter 2: Charge injection and transport

The combination of metal electrodes and organic semiconductors is widely applied in organic optoelectronic devices. The interfacial electronic structure between metal and an organic material is therefore one critical factor to determine the device performance. The alignment between the metal work function and the organic energy level is essential in light-emitting mechanism.

The performance of optoelectronic devices depends on a large number of factors, such as the intrinsic properties of active organic materials, the device configuration, the characteristics of the semiconductor/insulator interface, etc. Among them, the intrinsic property of the active organic material is the prerequisite factor to determine the charge transport in the semiconductor device.

This chapter begins with a theoretical introduction of the charge injection and transport, which involves energy levels, different theoretical models regarding charge injection, calculation tools, and various intrinsic parameters (i.e., transfer integral, reorganization energy, and charge carrier mobility) regarding the charge transport. The corresponding calculations are subsequently provided.

2.1 Theory

2.1.1 Energy levels

In organic semiconductors, charge is localized on single molecules. The most important molecular orbitals of these molecules are the highest occupied molecular orbital (HOMO) and lowest unoccupied molecular orbital (LUMO), which can be regarded as being equivalent to the valence bands and the conduction bands in inorganic semiconductors, respectively [91]. The energy gap (E_g) of HOMO and LUMO levels, together with vibronic energy levels of each electronic energy level, determine the characteristics of the absorption and emission spectra of the organic material [92-94].

When the organic semiconductor of an organic transistor has intimate contact with metal electrodes, the band structure for the organic material and two metal electrodes can be simplified as Figure 2.1. The vacuum level is defined as the level from which electrons can escape from the atoms. The energy separation from HOMO level or LUMO level to the vacuum level is defined as the ionization energy and the electron affinity of the organic semiconductor, respectively. Under voltage bias, the holes or

electrons can be injected from the metal electrode to the organic semiconductor. If the HOMO level is shallower than the metal work function, the energy separation from the gold work function to the HOMO level of organic semiconductor is the hole injection barrier Φ_h. Likewise, if the LUMO level is higher than the metal work function, the energy separation from the metal work function to the LUMO level of organic semiconductor is the electron injection barrier Φ_e.

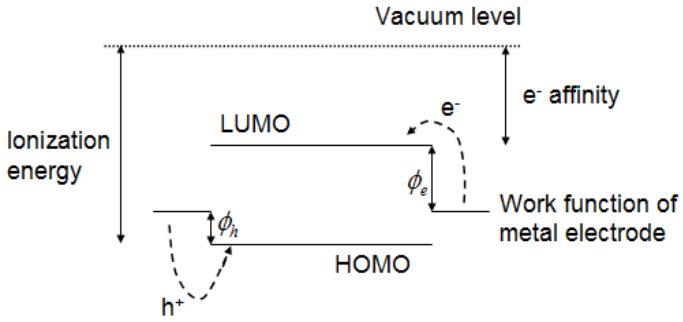

Figure 2.1: Schematic illustration of energy levels when the organic semiconductor and metal electrodes have contact. Φ_h and Φ_e are the energy barriers for hole and electron injection, respectively.

Based on the dominant charge carriers injected and transported in the transistor channel, the organic transistors can be classified as p-type (holes as main charge carriers) and n-type (electrons as main charge carriers). When the holes and electrons are nearly symmetrically injected from metal electrodes on both sides into organic semiconductor, it is denoted as the ambipolar transport [53]. If the work function of metal electrode is aligned with the LUMO or HOMO level of organic layer well, an ohmic contact is formed at the interface, which can facilitate efficient charge injection. However in practice, the work function of the metal electrode is usually misaligned with the energy levels of the organic semiconductor, a Schottky barrier is formed and the holes or electrons from metal electrodes should surmount the above-mentioned injection barrier so as to inject into the organic semiconductor [95-96].

Self-assembled monolayer (SAM) can be used to modify the metal electrodes in order to facilitate the charge carrier injection, and SAM deposition is especially suitable for transistors with BC/BG configuration due to the fact that the SAM can be prepared directly on the electrodes before deposition of the organic semiconductors [97-100]. For the surface of gold (Au) electrodes, alkanethiols are often used to modify the work function and affect the interface dipole because of the tight bond between thiol and Au [101-102]. In this work, two types of SAMs, i.e., octadecanethiol (ODT, linear formula: $CF_3(CH_2)_{17}SH$) and 1H,1H,2H,2H-Perfluorodecanethiol (PFDT, linear formula: $CF_3(CF_2)_7(CH_2)_2SH$) were utilized to modify the Au surface before depositing PPTPP organic thin films to investigate the change in charge injection in a transistor platform. Also, the SAM ODT and PFDT were applied to modify the Au/p6P thin film interface in OLETs. Due to opposite dipoles of the two monolayers, ODT is expected to lower the electrode work function,

while PFDT is expected to increase the electrode work function [103-105]. Therefore, in a view of charge injection from the Au electrode to organic semiconductor, the monolayer ODT will increase the hole injection barrier, while PFDT will decrease the injection barrier.

2.1.2 Theoretical approaches to charge injection

There have been a great number of investigations on the charge injection from metal electrodes to organic semiconductors [106-110]. The early theoretical investigations generally neglected the localized polarons formed by charge carriers in organic semiconductors. The theory developed by Richardson et al. considered the thermionic emission of electrons from a metal surface and the electrons are considered to be wave-like [111], which can only be generalized to the injection from a metal into a theoretically perfect crystalline semiconductor [5]. Bethe et al. investigated the case that charge carriers leave a crystalline semiconductor and enter a metal ballistically, and a counter flowing electron current was considered [109]. Schottky and Crowell considered the effect of scattering and diffusion, and a preexponential factor containing the charge density of states was utilized in their drift-diffusion equation [112-113].

Various models considering the energetic disorder of organic semiconductors have been developed [108,114-115], and the energy distributions follow a Gaussian density of states, as illustrated in Figure 2.2. Here, p6P and Au are treated as the organic semiconductor and metal electrode, respectively. The practical work function of the Au electrode is typically 5.1 eV [116], and the HOMO level of p6P is 6.0 eV [63]. Therefore a hole injection barrier of 0.9 eV can be expected. The charge injection in these models considering energetic disorders normally has two steps. The first step is that the charge carriers inject from the metal into the localized states of the organic semiconductor as shown in Figure 2.2; the second step is that the carriers either return to the metal or escape diffusively into the organic material.

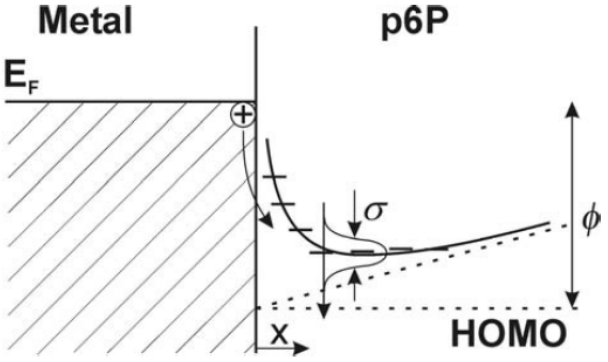

Figure 2.2: Schematic illustration of the hole injection from metal to a localized state into p6P. Reproduced from [30].

In this work, the model based on thermally assisted tunneling developed by Arkhipov et al. has been applied to study hole injection into the hopping state distribution of the organic semiconductor (p6P here) [108]. In this model, the hole injection occurs over/through a potential barrier *U(x)* given by

$$U(x) = \varphi - \frac{q^2}{16\pi\varepsilon_0\varepsilon_r x} - qFx \qquad \text{Eq. (2.1)}$$

where x is distance from the metal electrode, φ is the energy difference between the work function of Au and the HOMO level of p6P, $\varepsilon_0\varepsilon_r$ is the dielectric constant, q is the elementary charge, and F is the external field strength. The hole injection is considered including either the return of the charge-carrier to the metal electrode or the diffusive escape from the image potential to the semiconductor bulk. Therefore, the injected current I_{inj} can be described in terms of the tunneling probability $\exp(-2\bar{\Gamma}x_0)$ (x_0 is the distance from the contact the charge-carrier made the first jump) and the escape probability w_{exc} (x_0)

$$I_{inj} \propto \int_a^\infty dx_0 \exp(-2\bar{\Gamma}x_0) \cdot w_{esc}(x_0) \cdot \int_{-\infty}^{\infty} dE Bol(E) g[U(x_0) - E] \qquad \text{Eq. (2.2)}$$

where $\bar{\Gamma}$ is the inverse localization radius and a is the nearest neighbor distance. The escape probability w_{exc} (x_0) is the probability that a jumped carrier will avoid surface recombination, which is determined by

$$w_{exc}(x_0) = \frac{\int_a^{x_0} dx \cdot \exp[-\frac{e}{k_B T}(F \cdot x + \frac{e}{16\pi\varepsilon_r\varepsilon_0 x})]}{\int_a^{\infty} dx \cdot \exp[-\frac{e}{k_B T}(F \cdot x + \frac{e}{16\pi\varepsilon_r\varepsilon_0 x})]}. \qquad \text{Eq. (2.3)}$$

Bol(E) is a Boltzmann factor defined as

$$Bol(E) = \begin{cases} \exp(-\frac{E}{k_B T}) & E > 0; \\ 1 & E < 0. \end{cases} \qquad \text{Eq. (2.4)}$$

The Gaussian energy distribution with an energy width σ is given by

$$g(E) = \frac{N_0}{\sqrt{2\pi}\cdot\sigma} \cdot \exp(-\frac{E^2}{2\cdot\sigma^2}) \qquad \text{Eq. (2.5)}$$

where N_0 is the density of p6P molecules.

It should be noted that a model based on Fowler-Nordheim (F-N) tunneling is usually considered in terms of inorganic devices when extremely high electrical field is involved [117]. Even though an F-N plot can also be used to describe the relation between the current and stimulated electrical field in organic optoelectronic devices, the F-N tunneling is not part of the underlying operating mechanism [63-64].

2.1.3 Introduction of density functional theory (DFT) and basis sets

Quantum chemical modeling is useful to predict the intrinsic properties of organic semiconductors, so as to facilitate the synthesis and selection of novel organic optoelectronic materials. The powerful theoretical tool DFT is usually involved [93,118-122]. The basis of the quantum chemical calculations is the well-known Schrödinger equation [123]. It describes the changes of the quantum state of a physical system, with the general form

$$\{-\frac{\hbar}{2m}\nabla^2 + V\}\Psi(r,t) = i\hbar\frac{\partial\Psi(r,t)}{\partial t} \qquad \text{Eq. (2.6)}$$

where ∇^2 is the Laplace operator in three dimensions. The Schrödinger equation describes a single particle with mass m moving through space and time under the influence of an external field V. $\hbar$ is the reduced Planck's constant, Ψ is the wave function representing the probability amplitude for the particle to be found at position r and at time t. The Schrödinger equation can only be exactly solved for atoms with only one electron. Regarding a multi-electron system, no exact solutions can be found. In this case, the Hartree-Fock method can be used to solve the Schrödinger equation approximately. The Hartree-Fock method is based on the variation theorem, which states that any approximation will have an expectation energy value being greater than or equal to the true energy. Consequently, the better approximated wave function is obtained with the first derivative of the energy approaching to zero. More detailed can be found in Ref. [123].

The Hartree-Fock method provides the basis for the ab initio molecular orbital calculation, which refers to a quantum mechanical method in which only physical constants are provided as the calculation input. The most basic ab initio method assumes that the electrons move in an averaged potential of the other electrons without considering the instantaneous Coulombic repulsion among adjacent electrons.

Unlike the Hartree-Fock method, in DFT calculations, the properties of a multi-electron system can be expressed as functional, which is a function of another function, i.e. electron density. By doing so, the total electronic energy of a system and its overall electronic density are correlated, which transfers the study object from the wavefunctions of a N electron system with $3N$ spatial coordinates in Hartree-Fock method to the same N electron system with only 3 spatial coordinates for its electron density.

The basis sets used in the quantum chemical modeling are a set of trial orbitals, which can give another set of solutions after iteration during calculations, and then this set of solutions is used for the next iteration, likewise, until the convergence is achieved. The basis sets are typically a combination of Gaussian orbitals, which have the form of $x^a y^b z^c \exp(-\alpha \cdot r^2)$ in Cartesian coordinates, where α determines the degree

of spreading of the Gaussian function, e.g. a function with a small value of α spreads relatively far. The sum of a, b and c determines the type of orbital. For instance, $a+b+c=1$ indicates a p-orbital.

Since generally only the valence electrons take part in most of the molecular bonding, it is common to double the functions used to describe the valence orbitals, whereas the inner shells are represented by single functions. This is called split valence double zeta basis sets, with a typical notation of X-YZg, where X represents the number of Gaussian functions describing the core orbitals, Y and Z indicate that the valence orbitals are consisted of two basis functions, Y for contracted part and Z for diffuse part. For instance, 6-31g indicates that six Gaussian functions are used to describe the inner orbitals, while the valence orbitals are represented by three Gaussian functions for the contracted part and one Gaussian function for the diffuse part. Usually, polarization functions need to be added into the basis sets, which is indicated by one asterisk (*) for adding polarization only for heavy atoms, or two asterisks (**) for adding polarization both for heavy atoms and hydrogen atoms. When it comes to anions and other molecules with a significant amount of electron density away from the nuclear centers, highly diffuse functions are important to be introduced, which are denoted by one plus sign (+) for heavy atoms, or two plus signs (++) both for heavy atoms and hydrogen atoms.

The abovementioned basis sets are examples used in the computational chemistry software Gaussian 09 [124], while some similar basis sets can only be used in another computational type of software. For instance, Double Zeta Polarization (DZP) is implemented in Amsterdam Density Functional (ADF).

2.1.4 Intrinsic charge transport

In organic semiconductors, charges are localized on single molecule, and the charge transport in this localized system is mainly a hopping process from one molecule to a neighboring molecule. This hopping regime of charge transport in organic materials is important in determining the performance of optoelectronic devices. The intersite charge transfer rate k_{ij} in this hopping regime is given in the semi-classical approximation by the Marcus equation [125],

$$k_{ij} = t_{ij}^2 \sqrt{\frac{\pi}{\hbar^2 k_B T \lambda_{ij}}} \exp\left(-\frac{(\Delta E_{ij} - \lambda_{ij})^2}{4\lambda_{ij} k_B T}\right) \qquad \text{Eq. (2.7)}$$

where $\hbar$ is the reduced Planck's constant, ΔE_{ij} is the energy difference between the initial and final site energy, k_B and T are the Boltzmann constant and the temperature, respectively. The transfer integral t_{ij} and the reorganization energy λ_{ij} are the predominant factors to determine the charge transfer rate, whereas ΔE_{ij} is often insignificant [126].

The transfer integral describes the energy gained by electron delocalization among neighboring molecules, and it depends largely on orbital overlap [127]. The calculation of the transfer integral, considering the polarization effects between asymmetry molecules, is usually based on the Kohn-Sham equation [123]. The Kohn-Sham equation can be described in a matrix form when only a dimer is considered

$$HC = SCE \qquad \text{Eq. (2.8)}$$

where S is the overlap matrix and the Kohn-Sham matrix H is given by

$$H = \begin{pmatrix} e_1 & t_{12} \\ t_{12} & e_2 \end{pmatrix}. \qquad \text{Eq. (2.9)}$$

The elements of the Kohn-Sham matrix can be expressed as

$$H_{ij} = \left\langle \varphi_i \middle| \mathrm{H} \middle| \varphi_j \right\rangle \qquad \text{Eq. (2.10)}$$

where H is the Hamiltonian operator of the Kohn-Sham equation. In Eq. (2.10), H_{ij} stands for the site energy e when $i = j$; while H_{ij} is the transfer integral t when $i \neq j$.

The orbitals φ_i used in Eq. (2.10) are nonorthogonal. An orthogonal basis set is required and the effective transfer integral can be obtained using Löwdin's symmetric transformation [128] as

$$t_{12}^{eff} = \frac{t_{12} - \frac{1}{2}(e_1 + e_2)S_{12}}{1 - S_{12}^2}. \qquad \text{Eq. (2.11)}$$

Next, the matrix S is set to identity matrix, and Eq. (2.8) can be expressed in the orthonormal basis as a standard eigenvalue equation

$$H^{eff} C = CE. \qquad \text{Eq. (2.12)}$$

The reorganization energy is the energy cost accompanying the geometric relaxation of an oligomer associated with the charge transfer [127]. Assuming the transfer integral is constant, the charge transfer rate increases with decreasing reorganization energy. The reorganization energy consists of inter- and intra-molecule contributions. The inter-molecule reorganization energy is attributed to the electronic and nuclear polarization/relaxation of the surrounding environment, which means that the adjacent molecules with respect to the target molecule should also be considered during calculation. The intra-molecule reorganization energy results from the changes in equilibrium geometries of the donor and acceptor molecules during the charge transfer process. It can be determined by summing up two relaxation energies: the relaxation of the donor molecule upon going from the charged-state geometry to the neutral-state geometry, i.e., $\lambda_0 = E_{01} - E_{00}$; and the relaxation of the acceptor

molecule upon going from the neutral-state geometry to the charged-state geometry, i.e., $\lambda_1 = E_{10} - E_{11}$ [129]. As illustrated in Figure 2.3, E_{00} is the ground state energy of the neutral molecule, and E_{10} is the energy of charged state at the optimal neutral-state geometry; E_{11} is the ground state energy of the charged molecule, and E_{01} is the energy of the neutral state at the geometry of the charged molecule.

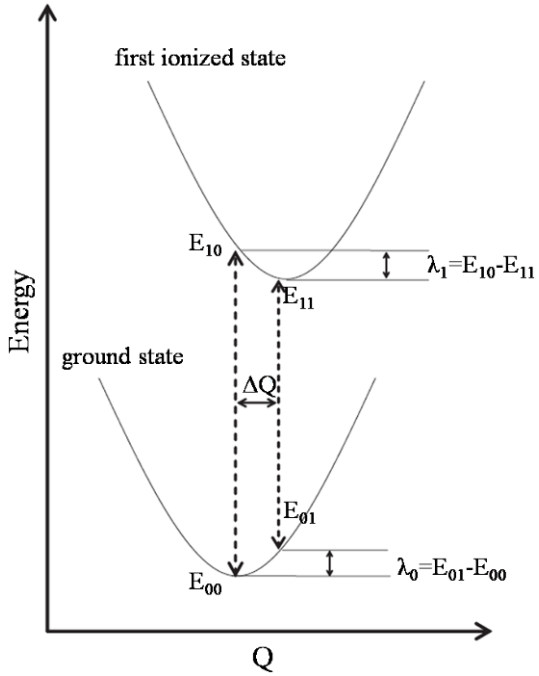

Figure 2.3: Schematic representation of potential surfaces related to electronic transfer, illustrating the vertical transitions, the normal mode displacement (ΔQ) and relaxation energies λ_0 and λ_1.

The intrinsic charge carrier mobility can be viewed as proportional to the charge transfer rate [127]. Since the organic semiconductors used in this work are mainly used in p-type OFETs, we will only focus on the hole mobility. The hole mobility can be correlated to the transfer rate via the diffusion coefficient of the charge carriers, and the diffusion coefficient D of the charge carriers can be expressed as

$$D = \frac{L^2 \cdot k_{ij}}{2} \qquad \text{Eq. (2.13)}$$

where L is the effective length of the charge transfer [130]. L is estimated as the center of mass distance of a dimer. Using Einstein relation [130-131], the charge mobility can be described as

$$\mu = \frac{qD}{k_B T} = \frac{qL^2 \cdot k_{ij}}{2k_B T} \qquad \text{Eq. (2.14)}$$

where q is the elementary charge.

2.2 Calculations

2.2.1 Energy levels

An appropriate organic semiconductor with suitable HOMO/LUMO level is very important for photosensitive devices, such as phototransistors. The energy gap E_g between HOMO and LUMO levels determines the range of incident light which can be absorbed or detected by the phototransistor, because only incident photons with higher energy than E_g can excite the electrons from the HOMO to the LUMO level [93,132-133]. The better alignment of HOMO/LUMO levels with metal work function is also important to the subsequent charge carrier collection through the metal electrodes.

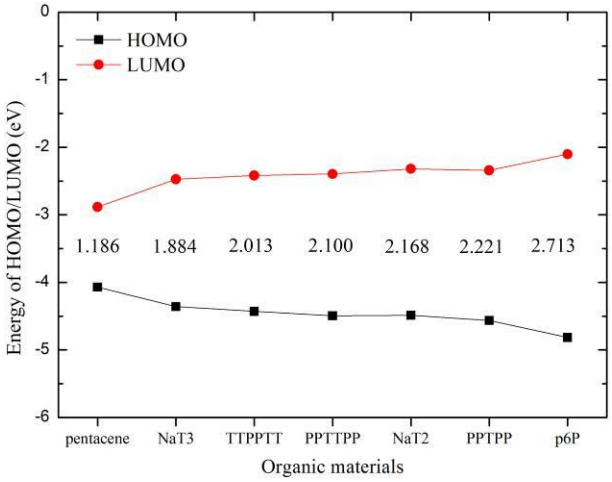

Figure 2.4: HOMO/LUMO of various materials calculated by PW91 using Gaussian 09. The values between HOMO and LUMO are the corresponding energy gap E_g.

To estimate the optical properties of the organic semiconductors used in this work, the HOMO/LUMO levels are calculated using the PW91 exchange-correlation functional together with the 6-31g* basis set. It has previously been shown that this combination provides reliable results for sulfur-contained materials [134], thus being suitable for calculations of thiophene-based materials. As shown in Figure 2.4, pentacene has the narrowest energy gap, indicating that pentacene can be suitable for long-wavelength light detection [132,135]. In contrast, p6P possesses the widest theoretical energy gap, which indicates that p6P might only be suitable for detecting UV light because of its higher requirement for the energy of incident photons. The energy gaps of other materials illustrated in Figure 2.4 suggest that the materials could be suitable for the detection of light with wavelength in the visible range. The schematic illustration of the orbitals is provided in Appendix C. For the OPT devices used in this work, NaT2 was chosen to be the active organic material due to its relative novelty [64,85]. It should be also noted that the HOMO/LUMO levels cannot be precisely predicted by the DFT approach. However, the theoretical energy gap can

be reliable. For instance, the theoretical energy gap of p6P is about 10% underestimated by the DFT calculations, in comparison with the experimental value (3.0 eV) [63].

2.2.2 Transfer integral

The transfer integral calculations were carried out using a combination of PW91/6-31g* level of theory. Since the transfer integral is assimilated to the electronic coupling among neighboring molecules during the hopping regime of the charge transfer process [127], it is largely dictated by the orbital overlap, which describes the overlap of particular obitals determined by the mutual separation and orientations of the neighboring molecules [136]. Therefore, larger values of transfer integral are usually expected along the direction in which the distance between the two neighboring molecules is nearer. In practice, this distance along the transverse direction of the dimmer is often the smallest, as shown in Figure 2.5. In Figure 2.5, only a NaT2 crystal structure containing five oligomers is provided to categorize the different charge transporting directions. The horizontal direction is denoted as *a*, whereas the direction which is perpendicular to the direction *a* is marked as *b*. The intermolecular distances from the centered oligomer to the other four peripheral oligomers (corresponding to the transverse direction of the dimers) are denoted as *d1*, *d2*, *d3*, and *d4*, respectively.

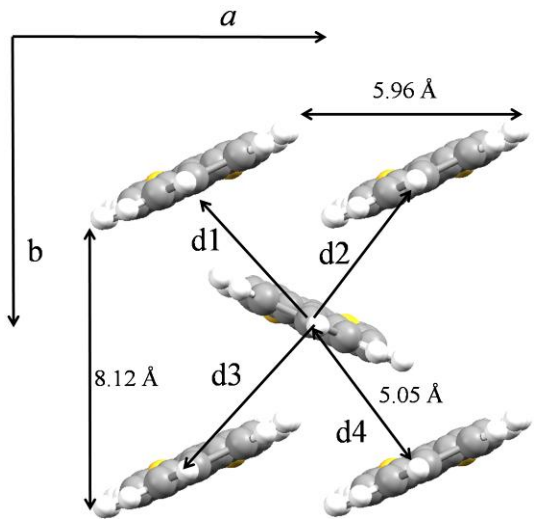

Figure 2.5: Crystal structure of NaT2 [85]. The arrows indicate the intermolecular overlap directions used in the theoretical calculation.

Table 2.1 presents the lattice constants of seven organic crystals. It should be noted that the measuring methods of gaps between transverse molecules for different materials are classified into three groups according to the backbone structure. For pentacene, p6P and NaT2, the gap among transverse molecules are measured between two virtual points which are averaged coordinates of part of the central atoms in each oligomer. In contrast, for other materials with relatively highly bent

backbone structure, the virtual points are averaged coordinates of all the atoms in each oligomer.

Table 2.1 Lattice constants in direction *a* and *b*, and distances between transverse molecules in various organic materials.

materials	lattice constant in direction *a* [Å]	lattice constant in direction *b* [Å]	gaps between transverse oligomers [Å]
pentacene	6.266	7.775	$d1=d4=4.76$; $d2=d3=5.21^{\#}$
p6P	5.568	8.091	$d1=d2=d3=d4=4.911^{*}$
PPTPP	5.793	7.497	$d1=d2=4.64$; $d3=d4=4.77^{\S}$
PPTTPP	5.708	7.604	$d1=d3=5.0$; $d2=d4=5.0^{\S}$
TTPPTT	5.824	7.294	$d1=d3=5.0$; $d2=d4=5.0^{\S}$
NaT2	5.964	8.120	$d1=d2=d3=d4=5.05^{*}$
NaT3	5.917	7.866	$d1=d3=4.74$; $d2=d4=5.10^{\S}$

#: The gap is measured as the distance between two virtual points of corresponding oligomers, and each virtual point is the averaged coordinate of the six carbon atoms in the center of each oligomer.
*: The gap is measured as the distance between two virtual points of corresponding oligomers, and each virtual point is the averaged coordinate of the two carbon atoms in the center of each oligomer.
§: The gap is measured as the distance between two virtual points of corresponding oligomers, and each virtual point is the averaged coordinate of all the atoms of each oligomer.

Since the transfer integral along the transverse direction is of great importance in determining charge transport properties of organic crystals, the transfer integrals for HOMO in direction *d* are listed in Table 2.2. It is necessary to be careful when dealing with different transverse direction in organic crystals, since the symmetry is not the same for different materials, as shown in Table 2.1. The symmetry determination for different materials listed in Table 2.1 is further verified by direct calculation of corresponding transfer integrals. For instance, the *d* directions of p6P are all identical due to the same distance of mass center between the central oligomer and the four peripheral oligomers, and this is confirmed by the fact that the transfer integrals in the four directions are exactly the same. In contrast, according to the distance measurement, the *d*1, *d*4 directions and the *d*2, *d*3 directions of the pentacene crystal are identical, respectively. This is also confirmed by the calculations that the transfer integrals of *d*1 and *d*4 direction of pentacene are the same, and the transfer integrals of *d*2 and *d*3 direction are the same. It is noteworthy that the effective transfer integral along *d*1 and *d*4 direction of pentacene is higher than that along *d*2 and *d*3 direction, hence the denotation of higher t_{HOMO}^{eff} and lower t_{HOMO}^{eff}, respectively, as shown in Table 2.2.

Table 2.2: Transfer integrals of various organic crystals in direction *d* (direction *d* here refers to the transverse direction along which higher transfer integrals for holes are expected, see Table 3.1).

materials	higher t_{HOMO}^{eff} [meV]	lower t_{HOMO}^{eff} [meV]
pentacene	77.1	47.0
p6P	4.3	4.3
PPTPP	24.0	11.1
PPTTPP	24.3	5.9
TTPPTT	32.0	26.7
NaT2	28.5	28.5
NaT3	20.1	11.9

Pentacene acts as a benchmark material with the transfer integral of 77.1 meV and 47 meV in two different transverse directions, respectively, which is in agreement with literature [137]. This agreement suggests that the transfer integral for the other materials calculated using the same method is reliable. Moreover, intuitively speaking, the molecules in a organic crystal could tend to align in a manner that the higher effective transfer integral t_{HOMO}^{eff} , instead of the lower t_{HOMO}^{eff}, listed in Table 2.2 plays an important role in contributing to the charge transport process, we will use the values of higher t_{HOMO}^{eff} for the mobility calculations later. However, it should be noted that this is only an assumption, and in practice the lower t_{HOMO}^{eff} could be more important. Nevertheless, this assumption will not affect the mobility calculations.

2.2.3 Reorganization energy

The reorganization energy calculations were performed at the B3LYP/6-31g* (for intra-molecule reorganization energy) and B3LYP/6-31g** (for inter-molecule reorganization energy considering a five-oligomer cluser) level of theory, since these combination of hybrid functional and basis set yields reorganization energy values closest to experiments [129,138]. The organic molecules in the gas phase exhibit considerable inter-ring torsion angles which usually are not observed in crystal structures, so the oligomers here are constrained into planar conformation for reorganization energy calculations. Table 2.3 provides the intra-molecule reorganization energy of various different oligomers. However, it is noteworthy that in practice, the oligomers in a neutral organic crystal usually exhibit bent conformations, but a planar configuration only for 1+ charged state [137]. Therefore, the calculations listed in Table 2.3 are only approximations, however, without

affecting the comparison of reorganization energy values of different materials [127,129].

Table 2.3: Intra-molecule reorganization energies for holes of various oligomers (constrained into planar configurations). The functional and basis sets B3LYP/6-31g* are implemented.

materials	relaxation energy λ_0 [meV]	relaxation energy λ_1 [meV]	reorganization energy λ [meV]
pentacene	47	47	94
p6P	83	80	163
PPTPP	109	107	216
PPTTPP	113	111	224
TTPPTT	99	96	195
NaT	107	104	211
NaT2	117	113	230
NaT3	119	115	234

In order to estimate the reorganization energy more precisely, the inter-molecule contribution should be taken into account, which considers the electronic and nuclear polarization of the surrounding environment of a central oligomer [137]. Table 2.4 presents the total reorganization of three types of organic materials calculated from a five-oligomer cluster (see Figure 2.5) in a B3LYP/6-31g** level. The central oligomer of each cluster is allowed to relax during the geometry optimization, while the four peripheral oligomers are fixed in their crystalline position. The resulting reorganization energies are significantly lower compared with those listed in Table 2.3, indicating a huge influence from inter-molecule interactions on the reorganization energy. However, the total reorganization energy of pentacene (80 meV) calculated using a five-oligomer cluster by Bromley et al. [137] is much larger than the corresponding value (23 meV) determined here, even though the calculation methods and processes are the same. Besides, different crystal structures of pentacene (from Bromley et al. [139] and at 90 K from Mattheus et al. [140]) are both tested in this work. The huge discrepancy could be due to the optimizer/grid differences in the two calculations [137,141].

Although the calculations of the reorganization energy using the five-oligomer approach is more precise due to the consideration of the inter-molecule interaction, the inclusion of more molecules means more computing time of the DFT calculations. Moreover, the five-oligomer approach is not applicable for the molecules composed of large number of atoms, e.g., the DFT calculations using the five-oligomer approach regarding the PPTTPP cluster cannot convergent. Therefore, the

calculations listed in Table 2.4 with successful convergence are only regarded as the reference to show the influence of the neighboring molecules interaction on the reorganization energy calculations. For the subsequent intrinsic mobility calculations, the values of intra-molecule reorganization energy listed in Table 2.3 will be considered.

Table 2.4: Reorganization energies of three types of molecules calculated from five-oligomer clusters. The functional and basis sets B3LYP/6-31g** are implemented.

materials	relaxation energy λ_0 [meV]	relaxation energy λ_1 [meV]	reorganization energy λ [meV]
pentacene	12	11	23
NaT2	26	20	46
NaT3	25	17	42

2.2.4 Intrinsic mobility

In many circumstances, the charge mobility obtained using Eq. (2.14) have been reported to be in reasonable agreement with experimental measurements [131,136,142-144]. However, the exact values of mobility are difficult to estimate precisely using this approach, partly due to the neglect the role of the interaction with lattice phonons and of the induced electronic polarization [127,145-146]. Therefore we only focus on the comparison of the mobility in the level of orders of magnitude and only estimate the increasing trend of the mobility of the organic semiconductors [129].

Since the transverse direction of organic crystals usually plays an important role in determining the charge transport properties, the higher effective transfer integral t_{HOMO}^{eff} in the *d* direction provided in Table 2.2, combined with the intra-molecule reorganization energies calculated from planar oligomers listed in Table 2.3, are utilized here to calculate the charge mobilities, which are listed in Table 2.5. The corresponding center of mass distances between two adjacent molecules in *d* direction can be referred to Table 2.1.

As mentioned above, the exact values of mobility are difficult to estimate precisely and we only focus on the comparison of the mobility on the level of orders of magnitude. As shown in Table 2.5, the hole mobility of pentacene is approximately two orders of magnitude higher than that of p6P, and about one order of magnitude higher than the other materials. This indicates p6P may be less suitable for the application of transistors, in comparison with other materials listed in the table. However, this is only a very rough estimation of the mobilities, because that the intra-molecule reorganization energy could differ greatly if bent conformation

oligomers are considered [137,147], and also the inter-molecule interaction is not considered in Table 2.5.

Table 2.5: Calculated transfer rate and mobility of various organic materials. The calculations are based on the data provided in Table 2.2 and Table 2.3.

materials	transfer rate k_{ij} [$\times 10^{11} s^{-1}$]	mobility [$cm^2V^{-1}s^{-1}$]
pentacene	1300	$\sim 10^0$
p6P	1.4	$\sim 10^2$
PPTPP	25	$\sim 10^1$
PPTTPP	23	$\sim 10^1$
TTPPTT	58	$\sim 10^1$
NaT2	31	$\sim 10^1$
NaT3	14	$\sim 10^1$

The charge carrier mobility can be significantly enhanced if the total reorganization energy calculated by the five-oligomer cluster is considered, since the reorganization energy is dramatically decreased with accounting the inter-molecule interaction. For instance, a transfer rate 400×10^{11} s^{-1} of NaT2 crystal can be obtained using the five-oligomer method, which is approximately one order of magnitude lower than the calculated transfer rate relevant for pentacene ($\sim 5000 \times 10^{11}$ s^{-1}), and hence predicts a hole mobilily of NaT2 one order of magnitude lower than the pentacene.

2.3 Chapter summary

The theoretical approaches regarding the charge injection and intrinsic charge transport are presented in this chapter. The alignment of metal work function with the HOMO level and the LUMO level is very important in the charge injection process from a metal electrode to organic materials. SAMs can be used to modify the work function of the metal electrode so as to facilitate the charge injection. A model based on SCF assisted tunneling has been introduced regarding the hole injection into the hopping state distribution of the organic semiconductor. As for the intrinsic charge transport, two main parameters, i.e. transfer integral and reorganization energy, are introduced, and they are critical to determine the charge mobility of the organic semiconductor. The corresponding DFT calculations are also provided in this chapter in terms of estimating the electrical and optical properties of the organic materials used in this project.

Chapter 3: OLETs based on thin films and transferred nanofibers

This chapter documents the experiments of micro-scale OLETs. In the beginning, the experiment details of AC-driven OLETs based on p6P thin films are presented. An operating mechanism of the AC driven OLETs is subsequently proposed, mainly based on the time-resolved study, low-temperature experiments and corresponding calculations. The electrical and optical characteristics of the OLETs modified by SAMs are also provided. Later, this operating mechanism based on SCF assisted injection of the charge carriers is also applied to OLETs based on PPTPP/NaT/NaT2 thin films, as well as transferred p6P nanofibers.

3.1 Photoluminescence (PL) of organic thin films

The PL spectra of four types of organic thin films are illustrated in Figure 3.1, as the reference to compare with the electroluminescence (EL) spectra in subsequent sections. The photoluminescence spectra of all the materials were collected by exciting the materials with a He-Cd laser (wavelength of 325 nm) and recording the spectra with an ARC SpectraPro-150 spectrometer in ambient air.

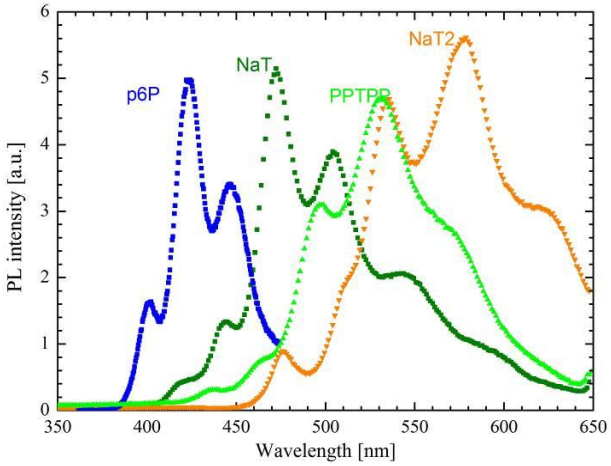

Figure 3.1: Photoluminescence spectra of four types of organic thin films based on small molecules.

The spectra indicate blue light emission from p6P, green-blue light emission from PPTPP and NaT, and yellow light emission from NaT_2. The peaks of the spectra can be attributed to the transition from the vibrational ground state of the electronic excited state to corresponding vibrational states of the electronic ground state. The gradually wider HOMO-LUMO gap from NaT2 to p6P suggested by the spectra in

Figure 3.1 is consistent with the HOMO-LUMO gap increasing trend calculated using DFT method, which are illustrated in Figure 2.4. It should be noted that NaT is not present in the theoretical calculations due to the lack of its crystal structure. However, it is already reported by Tian et al. that the HOMO-LUMO gap tends to decrease with the increasing number of thiophene rings in naphthyl end-capped oligothiophenes [85], which can explain the wider energy gap of NaT compared with NaT2 suggested in the photoluminescence spectra.

3.2 Operating mechanism

3.2.1 Preparation of micro-scale transistors

The substrates were prepared using standard cleanroom processes. Highly n-doped silicon (ρ = 0.025 Ω.cm) serves as the back gate electrode, on which 300 nm SiO_2 (C = 11.5 nF/cm^2) was thermally grown. Interdigitated array of titanium/gold (typically 2 nm/30 nm) source and drain electrodes were fabricated upon SiO_2 by optical lithography, metal evaporation (electron beam heating), and lift-off. The channel width W is 2.66 cm, and the channel length L varies from 2 μm to 25 μm. The substrate fabrication was completed by etching out a rectangular area (defined by photolithography) in the SiO_2 film using buffered hydrofluoric acid and then depositing titanium/gold (typically 10 nm/50 nm) as the contact pad to the back gate, which is depicted in Figure 3.2. The dimension of each chip is 3 mm long and 5mm wide. The detailed cleanroom processes to fabricate the micro-scale substrates are provided in Appendix D.

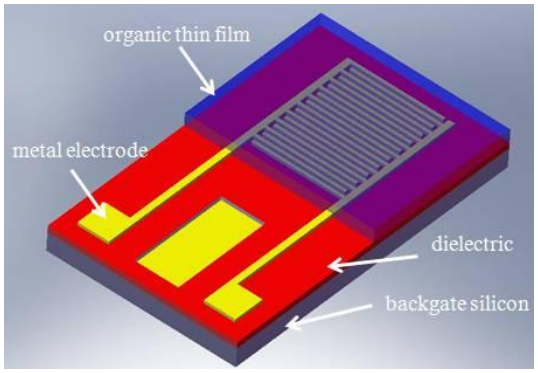

Figure 3.2: Schematic illustration of a micro-scale device deposited by an organic thin film layer.

The processed wafers were subsequently diced and cleaned by one minute ultrasonic agitation in acetone followed by five minutes flowing DI-water rinse. Afterwards the cleaned chips were put into vacuum chamber for deposition of organic materials immediately to avoid contamination.

Organic thin films with a thickness in the range of 30~50 nm were then deposited onto the substrates at room temperature and under a vacuum conditions (~10^{-7} mbar) at a rate of 0.1~0.4 Å/s. Since the organic thin films can be deposited at room

temperature, carbon taps which are vacuum compatible were directly put onto the sample holder to carry the transistor substrates, as shown in Figure 3.3.

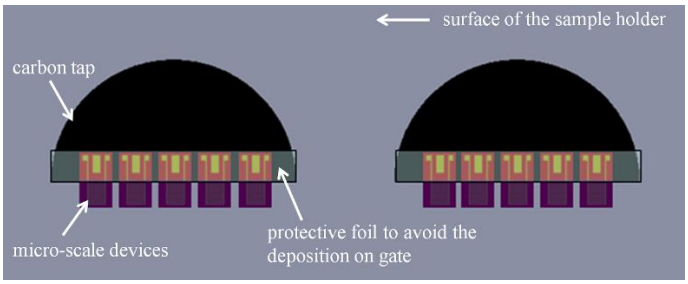

Figure 3.3: Schematic illustration of the micro-scale devices on the sample holder surface.

3.2.2 Electrical characteristics

In conventional DC-driven OLETs, electrons and holes are injected from opposite metal electrodes and subsequently recombine in the transistor channel, leading to light emission [53]. Sufficient injection and good transport of charge carriers are the prerequisite factor to influence the optical property of the OLETs. For AC-driven OLETs, electrons and holes can be injected from an individual metal electrode during different operating regimes of the AC gate voltage, leading to EL in the vicinity of one metal electrode [63-64,66]. The injection of electrons, for example, can be affected by the space-charge field formed by previously injected holes, and the injection of holes is the predominant factor to determine the AC-driven OLETs [63]. Therefore, the electrical characterization of the corresponding OFETs is necessary to evaluate the device performance of OLETs. In this project, The electrical measurement was made using a home-made setup based on a Labview-controlled data acquisition card in combination with a Stanford Research SR 570 current preamplifier and a Falco Systems WMA-280 voltage amplifier.

Figure 3.4 (a) and (b) show the p-type output characteristics of organic transistors based on p6P and PPTPP thin films, respectively. The drain-source voltage V_{ds} was biased from 0 V to -60 V, while gate voltage V_g was increased from 0 V to -60 V in steps of 10 V. It can be seen that the output characteristics of p6P thin film-based OFET illustrated in (a) are inferior compared to that of the PPTPP thin film-based OFET shown in (b), in terms of the threshold voltage. This indicates that the hole injection barrier in the p6P transistor can be higher than that in the p6P transistor, and there are more charge traps near the Au/p6P interface compared to the Au/PPTPP [53]. It should be noted that the maximum absolute current of p6P transistor is higher than that of the PPTPP transistor, which is due to the difference of the channel length of the p6P transistor (5 µm) and the PPTPP transistor (10 µm).

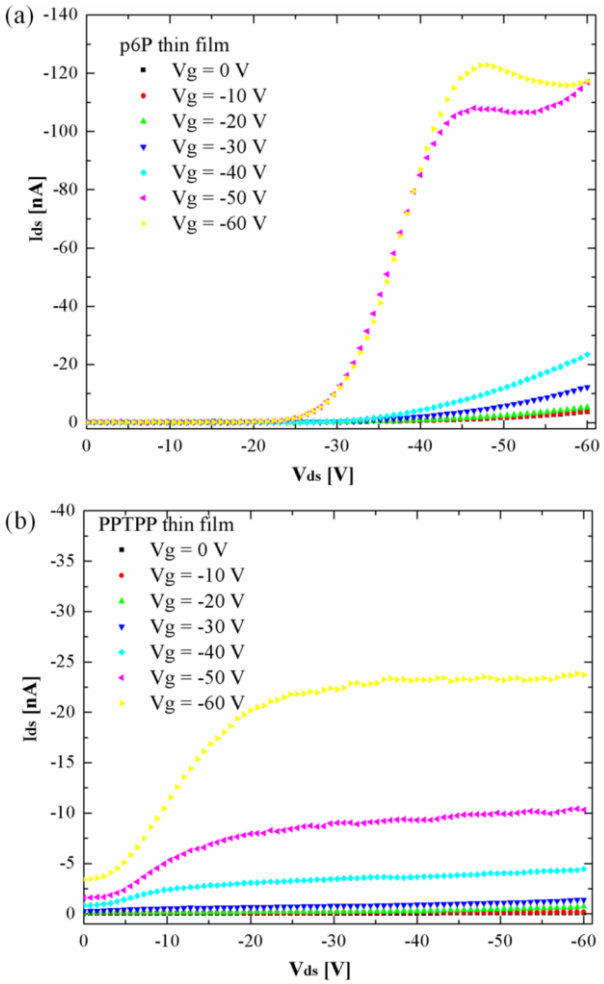

Figure 3.4: Output characteristics of organic transistors based on p6P thin films (a) and PPTPP thin films (b). The channel length is 5 µm and 10 µm for the p6P and PPTPP device, respectively. Drain-source voltage was biased from 0 V to -60 V, while gate voltage was increased from 0 V to -60 V in steps of 10 V.

In comparison, NaT2 thin film is better as an active organic semiconductor in transistors. Figure 3.5 (a) and (b) illustrate the output and transfer characteristics of a NaT2 thin film-based OFET operated at significantly lower voltages, respectively. The drain-source voltage V_{ds} was biased from 0 V to -8 V, while gate voltage V_g was increased from 0 V to -8 V in steps of 2 V. The better linear and saturation regimes in the output characteristics indicate that NaT2 is more suitable to be integrated into OFET, compared with p6P and PPTPP. A better charge trap condition in NaT2 thin film transistor can also be suggested from the corresponding transfer characteristics, in which the threshold voltage is shown to be nearly zero.

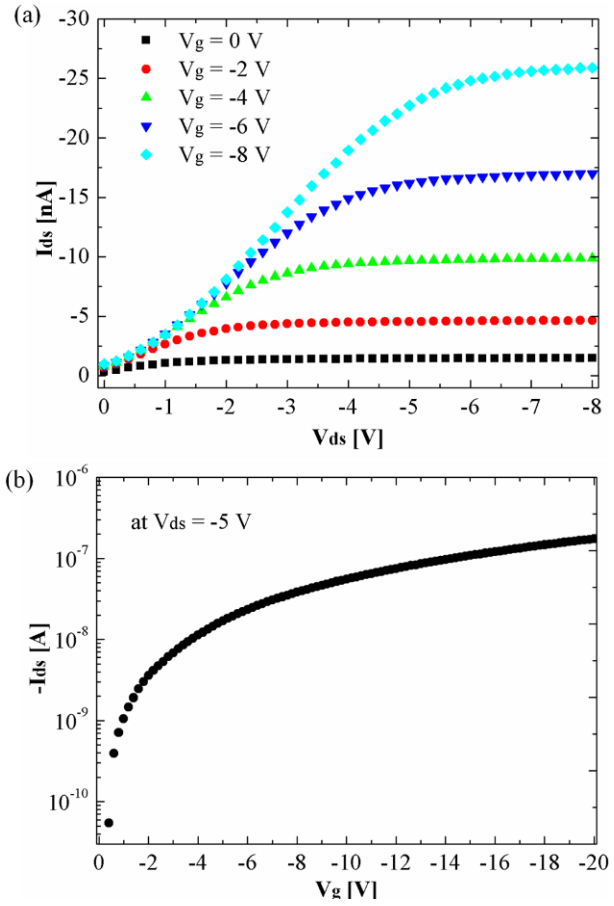

Figure 3.5: (a) Output characteristics of NaT2 thin film-based OFET. Drain-source voltage was biased from 0 V to -8 V, while gate voltage was increased from 0 V to -8 V in steps of 2V. (b) Transfer characteristics of the same NaT2 thin film-based OFET, with V_{ds} at -5 V.

3.2.3 Electroluminescence (EL) from p6P thin films and operating mechanism

Figure 3.6 (a) illustrates the device configuration of a p6P thin film-based OLET and the operating circuit used for light emission experiments. Although each metal contact is actually acting sequentially as electron "drain" and electron "source" during AC-driven operation, we have used the conventional terms "drain" and "source" as labels in order to distinguish between the metal contacts on the transistor platform. Figure 3.6 (b) and (c) show AC-driven light emission from a p6P film. In Figure 3.6 (b), only the drain electrode was biased while the source electrode was floating. This gives rise to light emission close to the interface between the drain electrode and the p6P film. When both the drain and the source electrodes were biased, light emission from both sides of the channel (i.e. from both electrode-p6P interfaces) can be observed as seen from Figure 3.6 (c). Figure 3.6 (d) shows the electroluminescence spectrum obtained with an amplitude of the sinusoidal gate voltage (V_p) of 62.5 V (frequency was 60 kHz and drain and source electrodes were grounded). A scaled PL spectrum is provided for comparison. The similarity of EL

and PL spectra with three main peaks at 401, 422, and 448 nm corresponding to the (0→0), (0→1), and (0→2) vibronic transitions [92], respectively, indicates that identical excitonic transitions take place in both cases although with different relative intensities. The spatial distribution of the emission in Figure 3.6 (b) and (c) was recorded by a camera mounted on a microscope while the spectra in Figure 3.6 (d) was recorded with an ARC SpectraPro-150 spectrometer.

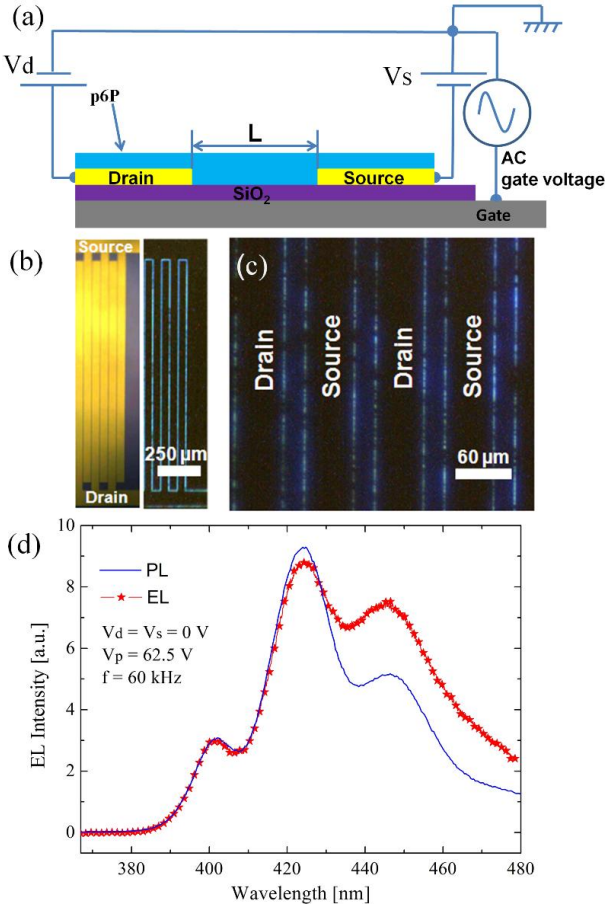

Figure 3.6: (a) Schematic diagram of the operating circuit for light emission experiments along with the device configuration. (b) Optical microscope image of AC-driven light emission when only the drain electrode is biased while the source electrode is floating. (c) AC-driven light emission when both the drain and source electrodes are biased (channel length is 25 µm). (d) EL spectrum from a p6P OLET under gate voltage amplitude of 62.5V. A scaled PL spectrum is shown for comparison.

Since the light emission in our devices occurs from the circumference of a single biased electrode and from both sides of the device channel when both electrodes are biased, this indicates that charge transport across the channel does not play a role in the light generation process. Instead, the emitted photons must be caused by the radiative recombination of holes and electrons injected from the same metal electrode. However, the work function of Au used for the electrode is 5.1 eV while the electron affinity of p6P is 3 eV; this leads to an estimated electron barrier height of more than 2 eV (neglecting a possible interface dipole). This suggests the hole injection probability is much higher than the electron injection probability. This is in

accordance with the previously reported transistor output characteristics, in which no n-type behaviour was observed, as shown in Figure 3.4 (a) [62]. The transistor therefore constitutes a unipolar device, however without any charge transport across the channel during AC operation.

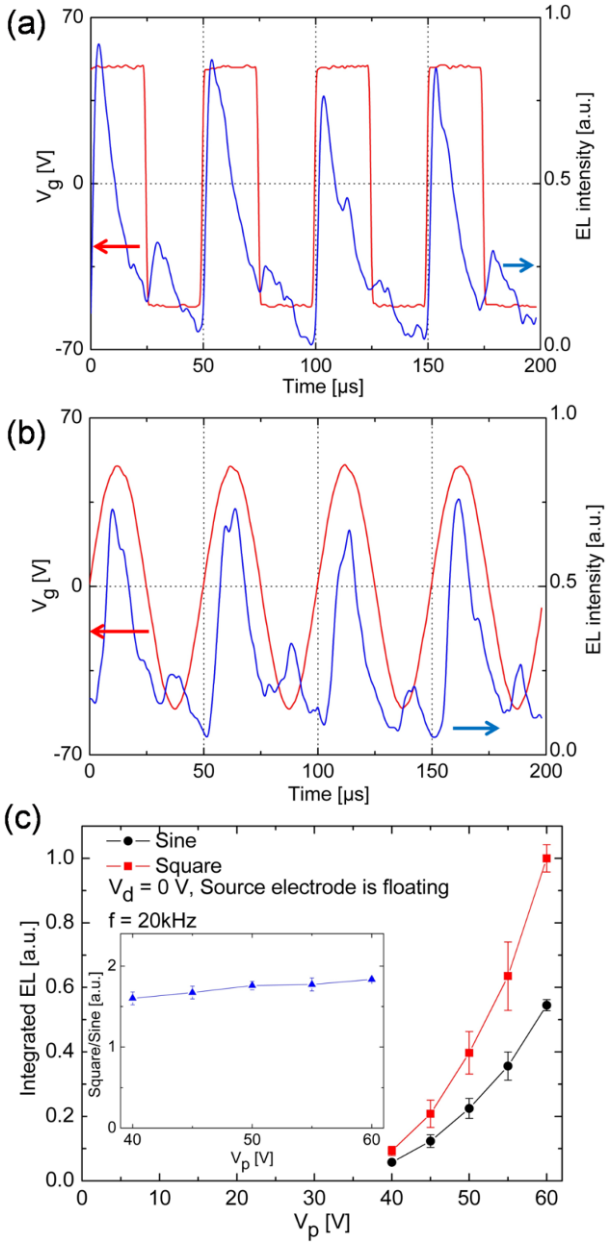

Figure 3.7: Time dependence of EL emission intensity (blue curve) as a function of (a) square wave gate voltage (red curve) and (b) sinusoidal gate voltage. (c) Integrated EL emission intensity as a function of (square wave and sinusoidal) gate voltage amplitude V_p. Inset: ratio of EL intensity obtained from square wave gate voltage to the intensity from sinusoidal gate voltage.

In order to show how the light emission is correlated to the instantaneous gate voltage, time-resolved EL intensity measurements were carried out, as illustrated in Figure 3.7 (a) and (b). The time-resolved data were recorded by a photo-multiplier tube (Hamamatsu R943-02) connected to a digital storage oscilloscope (Instek GDS-

2102) via a DC pre-amplifier (Hamamatsu C7319). The gate voltage waveforms in Figure 3.7 (a) and (b) are square wave and sinusoidal, respectively, and the amplitude in both cases is 62.5 V with a frequency of 20 kHz. Two distinct peaks can be observed within one period both for square wave and sinusoidal gate voltage. The larger EL peak appears when the gate voltage shifts from a negative to a positive value. In contrast, the smaller EL peak appears when the gate voltage shifts from a positive to a negative value. Using a light source with a known intensity, the photomultiplier set-up has been calibrated in order to quantify the emission intensity. The ratio of collected to emitted light was estimated by assuming a Lambertian emitter, while the emission area was found as the full width at half maximum of the emission zone multiplied by the emission zone length. This provides an estimate of the averaged intensity of 1×10^{-7} (estimated uncertainty: -3×10^{-8}, $+7 \times 10^{-8}$) W cm^{-2} for the data presented in Figure 3.7 (b). The detailed extraction of the emission intensity is provided in Appendix E.

To compare the averaged EL intensity generated from square wave and sinusoidal gate voltage, the amplitude of the gate voltage V_p was varied from 40 V to 60 V in steps of 5 V, while the drain electrode was grounded and the source electrode was floating. Figure 3.7 (c) shows how the EL intensity increases as V_p increases both for square wave and sinusoidal gate voltages. The EL intensity has been determined by summing up from 380 nm to 480 nm of the corresponding spectrum. The inset shows the ratio of the EL intensities for square wave to sinusoidal gate voltages. An approximated constant ratio of 1.73 is obtained. Since the effective value of a square wave is 1.41 times higher than the effective value of a sine wave with the same amplitude, a ratio higher than 1 is expected, however, this simplistic view cannot account for non-linear processes involved in charge injection across an energy barrier. A more appropriate analysis would be to study the effects of the gate voltage waveform using a theoretical model based on SCF assisted tunneling, which will be discussed later.

In order to investigate the influence of the drain voltage V_d on the emission intensity, a series of measurements were conducted, in which V_d was varied while the amplitude and frequency of the square wave gate voltage were fixed and the source electrode was floating. As shown in Figure 3.8, the integrated EL intensity increases when the drain electrode is positively biased while a negative drain potential causes a reduced EL intensity. Two measurement sequences were made in either direction: one from negative V_d to positive V_d and one in the other direction, and the corresponding values of the two measurement sequences were averaged, represented by the black square with error bar in Figure 3.8. This shows that the observed EL variations are indeed caused by the drain potential and are not due to a possible degradation effect.

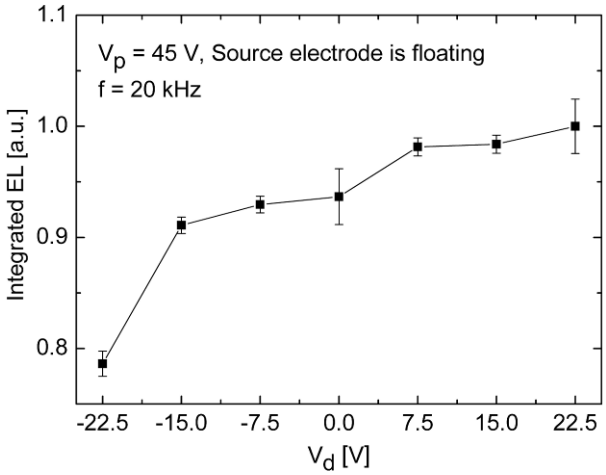

Figure 3.8: Integrated EL intensity as a function of drain electrode voltage V_d (source electrode was floating). The gate voltage amplitude was V_p = 45 V and the frequency was f = 20 kHz.

On the basis of the experiments presented before, an operating mechanism of the AC-driven OLET is proposed: Charge transport across the channel is not part of the light generation process. Rather, the two types of charge-carriers are sequentially injected from the same contact. This must mean that one type of charge is piled up in the organic film close to the electrode interface during one half-period of the gate voltage effectively forming a space-charge region at this position. During the subsequent half-period of the gate voltage, the opposite charge-carrier is injected, recombines with the first type of carrier, and thereby causes light emission. Since the injection of holes is much more probable than the injection of electrons in our device, the space-charge region must be formed by holes piling up either due to deep hole traps or short hole transport distance under high frequency operation. The positive space-charge region is therefore formed during the negative half-period of the gate voltage, as illustrated in Figure 3.9 (a).

In the next (positive) half-period, electrons are injected into the organic material to recombine with the previously injected holes. Since the injection barrier of electrons between Au and p6P is very high, the electrons are most likely to tunnel into the p6P. The electron tunneling process is primarily influenced by the positive space-charge region rather than the positive gate voltage, as shown in Figure 3.9 (b). This can be argued as follows: During the negative half-period of the gate voltage, holes are injected. If the DC potential of the drain electrode is increased (positive V_d), this leads to an increased hole injection and therefore a larger space-charge. In the following, positive half-period of the gate voltage, electrons are tunneling into the organic material. The positive value of V_d means that the drain to gate voltage difference is effectively reduced. If the main factor driving the electron tunneling would be the gate voltage, then the electron tunneling and thus also the emission intensity should be less than at zero V_d. On the contrary, if the main driving mechanism for electron injection is tunneling assisted by the positive space-charge

field (SCF), then the additionally injected holes caused by the positive V_d should enhance electron tunneling and thereby emission intensity. Since positive V_d causes increased EL intensity as previously shown in Figure 3.8, the second explanation must be correct.

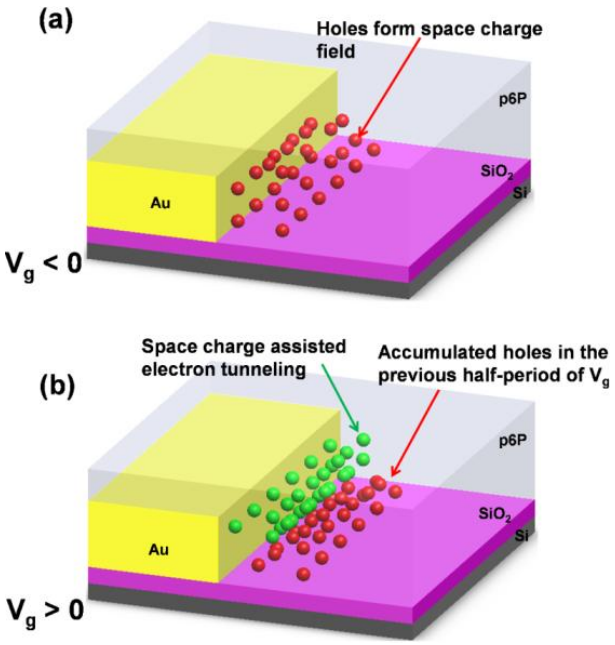

Figure 3.9: Schematic illustration of the device operating mechanism (red indicates holes; green indicates electrons). (a) Holes are injected from Au into semiconductor to form positive SCF. (b) In the next half-period of ac gate biasing, electrons tunnel into the semiconductor assisted by the previously formed positive SCF.

The time-resolved EL intensity illustrated in Figure 3.7 (a) and (b) can be explained by this model. The majority of the light emission occurs when the gate voltage shifts from a negative to a positive value, corresponding to the shift from hole to electron injection. This means the electron injection is significantly enhanced due to the positive SCF, which is formed by holes injected in the previous half-period of the AC gate voltage. The decay of the emission intensity after reaching its maximum must be caused by the recombination process that reduces the hole intensity. Upon elimination of the SCF by electron-hole recombination, electron injection continues at a lower rate caused only by the positive gate voltage. When the ac gate voltage shifts polarity, a smaller EL peak can be observed, which is caused by the recombination of the electrons injected in the previous positive gate regime and the holes injected during this negative gate bias.

Since the electron tunneling is enhanced by the positive SCF formed by previously injected holes, the hole injection is an important factor to determine the overall light emission of the p6P device. We therefore focus on the hole injection aspects in the following discussion and assume the EL intensity to be proportional to the magnitude of the hole injection. It was previously show that the relationship between the EL

intensity and the gate voltage amplitude corresponds to a straight line in a Fowler-Nordheim (F-N)-type plot [64]. However, F-N theory describes charge-carrier tunneling through an energy barrier into a delocalized state, which is typically not the case in organic materials, in which the charge-carriers form localized polarons. F-N theory is therefore not applicable for the present system [109].

Applying this model, we calculated the hole injection from a gold electrode to p6P with the external electric field generated either by a square wave or a sinusoidal gate voltage. The parameters (φ = 0.9 eV, σ = 0.27 eV, T = 295 K, ε_r = 1.9, a = 5.57 Å, $\bar{\Gamma}$ = (3Å)$^{-1}$, and N_0 = 1.71 × 10^{21} cm^{-3}) used in Eq. (2.1) to Eq. (2.5) were taken from Ref. [30]. Only one half-period of gate voltage is considered in the calculation due to the waveform repetition of the gate voltage. For simplicity, the external electric field near the vicinity of the injecting gold electrode was estimated simply as the gate voltage divided by the thickness of SiO_2 gate dielectric. We have performed finite element analysis calculations to verify that this assumption is reasonable. The amplitude of the gate voltage was varied from 40 V to 60 V, with steps of 5 V. The resulting ratio of hole injection generated by square wave gate voltage to that generated by sinusoidal gate voltage is approximately 2.2, which is 27 % larger than the experimental value shown in Figure 3.7 (c). This difference could be due to the neglect of the suppressing effect of the positive SCF on the further hole injection during the negative half-cycle of the AC gate voltage. This suppressing effect is larger for the square wave case resulting in an overestimation of the EL ratio.

In order to better understand the underlying operating mechanism, the temperature dependence of the PL and EL output was characterized. The low temperature measurements (down to 30 K) were made under vacuum conditions (~10^{-5} mbar) in a cryocooler (Sumitomo CNA-11 Helium Compressor Unit). As illustrated in Figure 3.10 (a), both the PL and EL intensity increase as the temperature decreases from 295 K to 30 K. With increasing temperature, the probability for coupling to phonon modes and thus in general for non-radiative decay process increases, as observed by an increase of the Huang-Rhys factor for p6P nanofiber films [148]. In addition, it can be seen that the PL increases more than the EL. The ratio of the normalized EL intensity to the normalized PL intensity $W_{EL}(T)/W_{PL}(T)$ is also shown in Figure 3.10 (a).

The temperature dependence of this ratio can be correlated with the temperature dependence of the hole injection as follows: The detected EL intensity $W_{EL}(T)$ is given by:

$$W_{EL}(T) = k_1 \cdot \eta_{ext}(T) \cdot I_{inj}(T) \qquad \text{Eq. (3.1)}$$

where $I_{inj}(T)$ is the injected current, $\eta_{ext}(T)$ is the temperature-dependent external quantum efficiency, and the temperature-independent proportionality constant k_1

includes the unit charge, the photon energy and collection efficiency of the detector. From [44] we describe $\eta_{ext}(T)$ by:

$$\eta_{ext}(T) = R_{st} \cdot \gamma \cdot \Phi_{outc} \cdot \Phi_{PL}(T) \qquad \text{Eq. (3.2)}$$

where $\Phi_{PL}(T)$ is the efficiency of radiative decay, R_{st} is the singlet to triplet ratio (typically 0.25), γ is the charge balance factor, Φ_{outc} is the outcoupling efficiency. The detected PL intensity $W_{PL}(T)$ is given by:

$$W_{PL}(T) = k_2 \cdot \Phi_{outc} \cdot \alpha(T) \cdot \Phi_{PL}(T) \qquad \text{Eq. (3.3)}$$

where the proportionality constant k_2 includes the intensity of the stimulating light, the photon energy, and the collection efficiency of the detector. Since the temperature dependence of the absorption cross section $\alpha(T)$ is very weak for p6P films [149], we neglect its temperature dependence here, i.e. $\alpha(T) = \alpha$. By combining Eq. (3.1), (3.2) and (3.3), the ratio of the EL and PL intensities is found to be

$$\frac{W_{EL}(T)}{W_{PL}(T)} = \frac{k_1}{k_2 \cdot \alpha} \cdot R_{st} \cdot \gamma \cdot I_{inj}(T). \qquad \text{Eq. (3.4)}$$

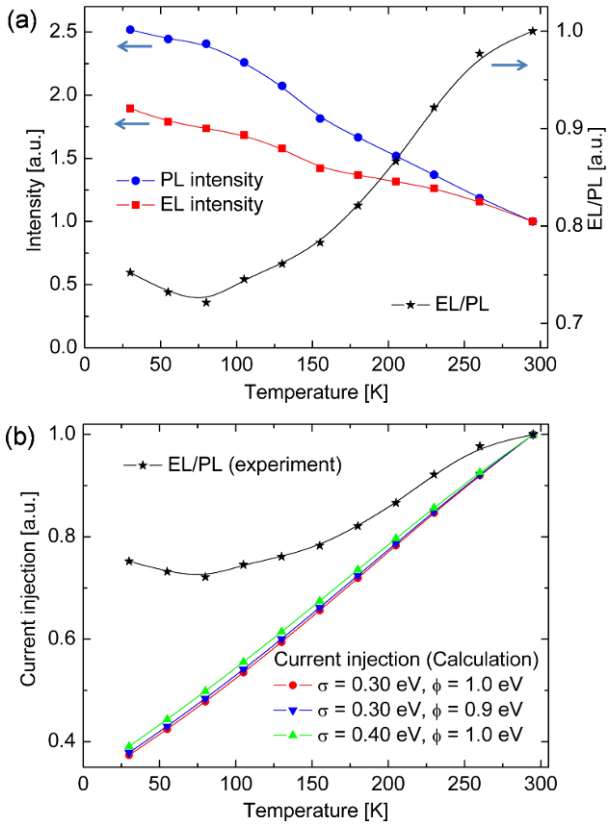

Figure 3.10: (a) Temperature dependence of PL and EL intensity (data have been normalized at T = 295 K) of a p6P light-emitting device. The square wave gate voltage amplitude was 37.5 V; the biasing frequency was 15 kHz. (b) Theoretical calculation of current injection compared with experiment.

Since all factors in Eq. (3.4) except the injected current have negligible temperature dependence, the ratio $W_{EL}(T)/W_{PL}(T)$ should therefore have the same temperature dependence as the injected current.

Figure 3.10 (b) shows the temperature dependence of the current injection calculated using the approach based on Arkhipov's model (see Section 2.1.2), and the ratio derived from experiment is again illustrated for comparison. The calculated current injection varies only slightly if the hole injection barrier ϕ or the energy width σ is varied. Also, it can be seen that the theory predicts a stronger temperature dependence than what is observed experimentally. This large deviation could be due to the inadequacy of the Gaussian energy distribution of the hopping state [150]. Nevertheless, the calculation based on Arkhipov's model reproduces qualitatively the trend observed experimentally, which is not captured by the F-N formalism.

We have focused on the hole injection between gold and p6P because the hole injection barrier in this case (typically 0.9 eV) is much lower than the electron injection barrier (2.1 eV). In contrast, electron injection should be mainly studied for the organic materials which possesses lower electron injection barrier with respect to the injecting electrodes.

To rule out the possibility that impact ionization could be involved in the light generation process, similar substrates but with aluminum rather than gold electrodes were fabricated. Since aluminum electrodes oxidize under ambient conditions, there will be an insulating layer of aluminum oxide between the electrode and the p6P, and light emission would under such circumstances only be possible via impact ionization [151]. Based on the sensitivity of our detection system, we estimate that the light emission from aluminum electrode devices is at least two orders of magnitude lower than that from gold electrode devices under similar biasing parameters, indicating that impact ionization plays an insignificant role for the light generation.

3.2.4 Self-assembled monolayer (SAM) modification

As described in Section 2.1.1, SAMs can be applied to modify the metal electrodes in order to facilitate the charge carrier injection. ODT (powder, 286.57g/mol) and PFDT (liquid, 480.18g/mol) were purchased from Aldrich and used without further purification. The micro-scale substrates with Au electrode were separated into two groups and rinsed in pure ethanol and 2-propanol, and blown dry with N_2. The two groups of substrates were subsequently immersed into ethanol solutions of ODT (10mg/20ml, i.e., 1.75 mM) and PFDT (0.011ml/20ml, i.e., 1.75 mM), respectively, for at least 16 hours. After the assembly process, the substrates were immediately rinsed in pure ethanol and 2-propanol, and dried with N_2 before the deposition of PPTPP or p6P thin films.

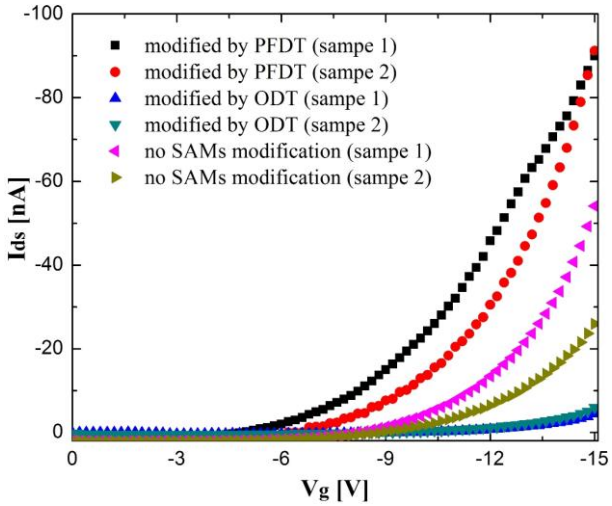

Figure 3.11: Transfer characteristics of PPTPP thin film-based OFET, modified by the SAMs PFDT and ODT. Characteristics of two samples without SAMs modification are shown as reference.

Figure 3.11 illustrates the transfer characteristics of six transistor devices based on PPTPP thin films, and the transistors are divided into three groups, i.e., two samples modified by ODT, two samples modified by PFDT, and the other two samples without SAMs modification. As seen in Figure 3.11, the maximum current and onset voltage of PFDT modified transistors are clearly better than the transistors without any modification, while the maximum current and onset voltage of ODT modified transistors are inferior compared with the transistors without modification. This is in good agreement with the fact that PFDT increases the Au work function, whereas ODT decreases the Au work function, leading to lower and higher hole injection barrier, respectively [103-105], as shown in Figure 3.12.

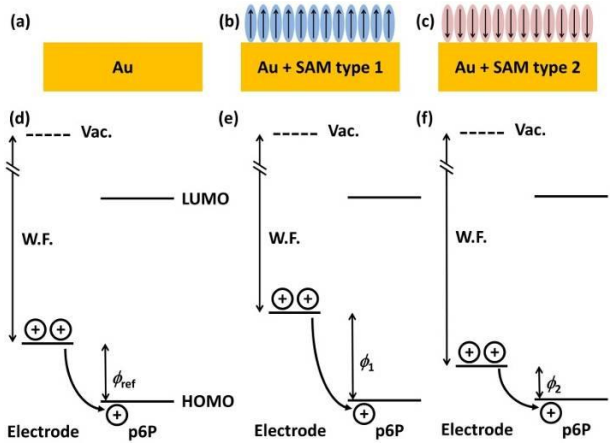

Figure 3.12: Schematic illustration of the variation of hole injection barrier from Au electrode to p6P. (a) and (d): No SAMs are applied. (b) and (e) Monolayers ODT have been applied to increase the hole injection barrier. (c) and (f) Monolayers PFDT have been applied to decrease the hole injection barrier. Reproduced from [105].

The SAM modified substrates with p6P thin films were used for the OLET investigation. Surprisingly, the light emission intensity of p6P-based OLETs

modified by ODT and PFDT can both be increased, as shown in Figure 3.13, even though the ODT monolayer was used to increase the hole injection barrier. This can be due to an improved interface microstructure resulted from the SAM modification [105].

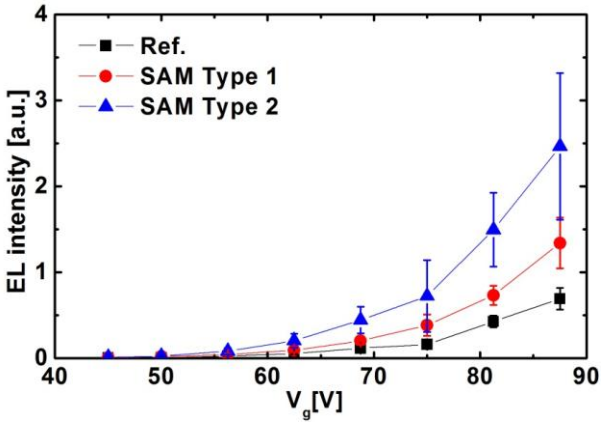

Figure 3.13: EL intensity versus amplitude of the sinusoidal gate voltage, and the frequency is 100 kHz. SAM type 1 represents ODT, and SAM type 2 represents PFDT. Reproduced from [105].

3.3 OLETs based on PPTPP, NaT and NaT2 thin films

The operating mechanism based of SCF assisted charge carrier injection can be also applied in OLETs of other organic thin films, such as PPTPP, NaT and NaT2. Figure 3.14 shows an optical microscope of the green-blue, green, and yellow EL from NaT, PPTPP, and NaT_2 thin films, respectively. The trend of the color variation is in agreement with the PL spectra illustrated in Figure 3.1. Figure 3.14 (a) shows a NaT device with 2.5 µm channel length emitting green-blue light generated by drain and source voltages of $V_d = -V_s = 10$ V and an AC gate voltage with a frequency of $f =$ 200 kHz and an amplitude of $V_p = 87.5$ V. Figure 3.14 (b) illustrates a PPTPP device with 2.5 µm channel length emitting green light generated by $V_d = -V_s = 10$ V and an AC gate voltage with a frequency of $f = 300$ kHz and an amplitude of $V_p = 75$ V. Electroluminescence of a NaT_2 device with 10 µm channel length is presented in Figure 3.14 (c) ($V_d = -V_s = 15$ V, $f = 200$ kHz, and $V_p = 62.5$ V). The inset of Figure 3.14 (c) demonstrates that electroluminescence can be observed from both sides of the channel close to the injecting contacts, and also occurs along the periphery of an individual electrode. However, light emission from opposing electrodes cannot be distinguished in devices with short channel lengths such as 2.5 µm and 5 µm.

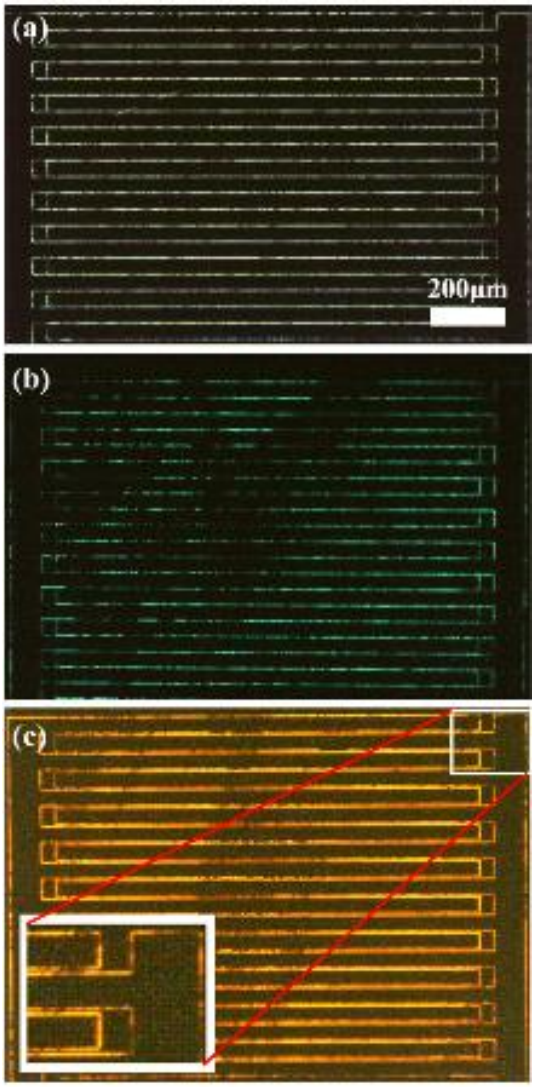

Figure 3.14: Optical microscope image of electroluminescence from a 52 nm thin film of NaT (a), a 42 nm PPTPP thin film (b), and a 52 nm thin film of NaT2 (c) operated by a sinusoidal AC gate voltage.

Figure 3.15 shows the electroluminescence spectra of a NaT device. The source and drain voltages are maintained at zero volts for the whole series of experiments while the frequency and the amplitude of the AC gate voltage are varied. A relative photoluminescence spectrum is also depicted in Figure 3.15 in order to compare to the electroluminescence spectra. Obviously, the intensity of the electroluminescence output increases with frequency and with voltage amplitude. The EL spectra contain some background noise due to their relatively low intensity, however, it is still clear that the peak positions corresponds to those observed in the PL spectrum and that the same electronic transistions are therefore responsible for the light emission.

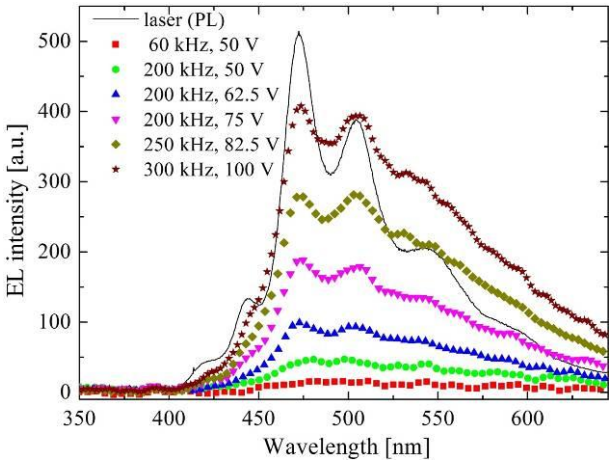

Figure 3.15: Electroluminescence spectra of 52 nm NaT thin film operated under drain and source voltages of V_d = -V_s = 0 V and an AC gate voltage with varying frequencies and amplitudes. The photoluminescence spectrum (scaled by a factor of 100) is also shown for comparison.

The light emission intensity from NaT2 is significantly higher than that of NaT, leading to more well-resolved electroluminescence peaks as demonstrated in Figure 3.16. Figure 3.16 (a) shows a clear dependence of the electroluminescence intensity on the AC gate voltage frequency. The initial linear relationship between intensity and the AC gate voltage frequency in Figure 3.16 (a) can be interpreted as a result of more holes and electrons recombining if more AC voltage cycles are accomplished within a fixed time interval. For a further increase in frequency, a deviation from the linear dependence is expected [62,117]. This can also be inferred from Figure 3.16 (b), which indicates that the EL intensity tends to deviate from a straight line at 200 kHz. This deviation could be caused by the short time period for injection at high frequencies. At the highest frequencies, sample degradation made it impossible to study further the high-frequency behavior.

Figure 3.16 (c) and (e) illustrate how the EL spectrum depends on the gate voltage amplitude and drain and source voltages, respectively. Figure 3.16 (b), (d), and (f) show the relationships between the total EL intensity and the various operating parameters. The points have been obtained by integrating the corresponding spectra in Figure 3.16 (a), (c), and (e), respectively, from 431 nm to 690 nm. The intensity increases approximately linearly with the frequency of the gate voltage (Figure 3.16 (b)) whereas it depends non-linearly on the gate voltage amplitude (Figure 3.16 (d)). The inset in Figure 3.16 (d) shows a Fowler-Nordhiem (F-N) type plot of the intensity vs. gate voltage amplitude including a fitted line. Strictly speaking, the F-N theory describes tunneling through a barrier into a delocalized state, which is not the case here where the charge carriers form trapped states (polarons) in the organic semiconductor and the charge transport occurs as incoherent hopping [152]. However, the excellent fit of the measured data points to the F-N behavior does suggest that the device current and thus the light intensity are governed by an

injection barrier at the metal-organic interface. The operating mechanism presented in Section 3.2.3 can well explain the EL dependence on the gate voltage and drain/source voltage, as provided from Figure 3.16 (c) to (f).

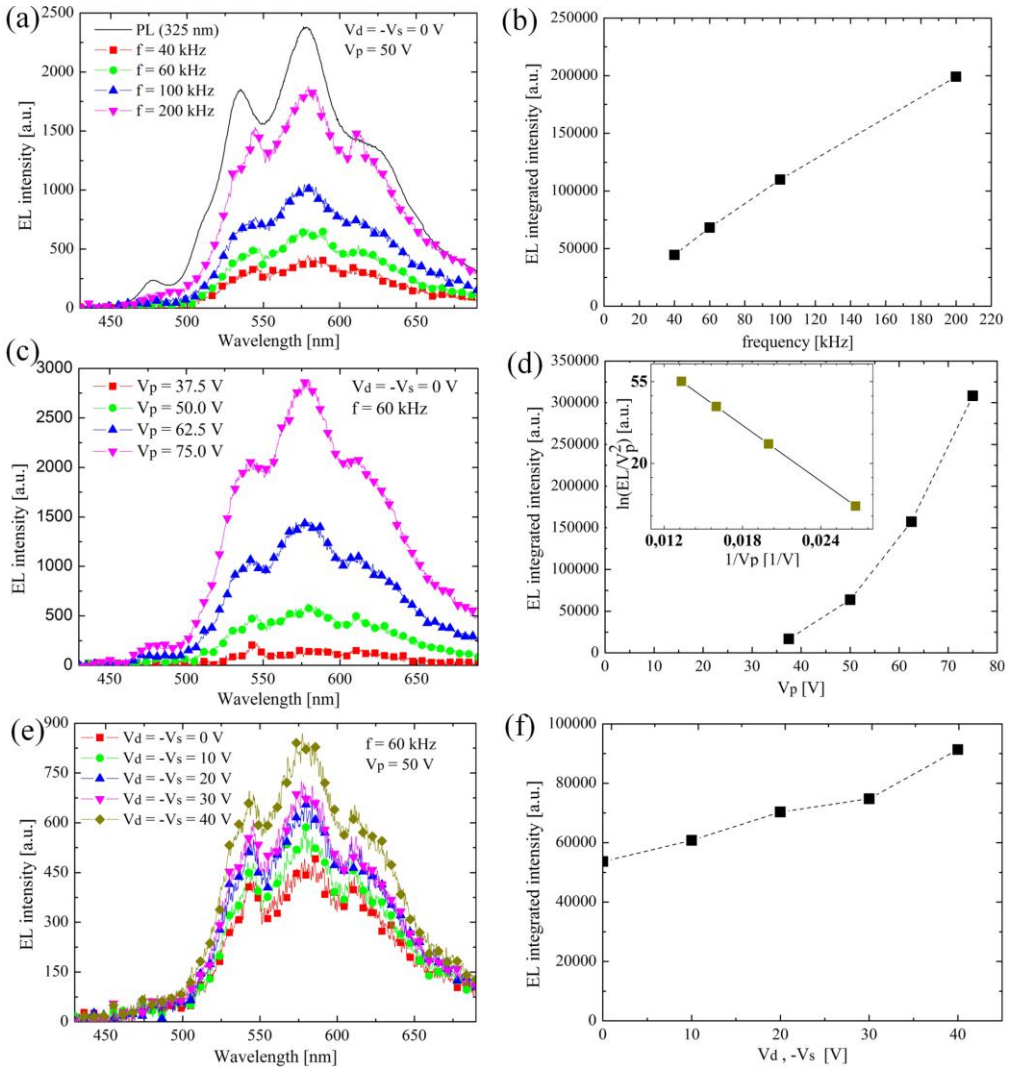

Figure 3.16: Electroluminescence spectra of 52 nm NaT2 thin film (channel length 5 µm) with variable frequency of AC gate voltage (a), AC gate voltage amplitude (c) and drain and source voltages (e). The graphs on the right side show the total intensity (spectra integrated from 431 nm to 690 nm) as a function of frequency (b), amplitude of AC gate voltage (d), and drain and source voltages (f). The inset in (d) is a Fowler-Nordheim type plot of the intensity vs. gate voltage amplitude.

3.4 OLETs based on transferred p6P nanofibers

The abovementioned SCF-involved operating mechanism of AC-driven OLETs is proposed based on thin film devices. This section presents that the same operating mechanism can also be applied in transferred nanofiber-based micro-scale devices.

3.4.1 Growth of nanofibers and transfer

Before the transfer process, the organic nanofibers are normally prepared on a heated muscovite mica by vapor deposition under high vacuum conditions (~10^{-8} mbar). The optimal substrate temperature during deposition is not the same for different materials, which should be optimized to obtain good nanofibers for subsequent device integration. For instance, the p6P nanofibers are typically deposited onto a freshly cleaved muscovite mica substrate at either 433 K to form small and dense fibers, or 453 K to form large and well-separated fibers [29]. The deposition rate is usually at ~0.1 Å s^{-1} to form a nanofiber layer with nominal thickness of 5 nm, and the molecules can self-assemble into mutually parallel p6P nanofibers, as shown in Figure 1.6.

Despite the poor processability of muscovite mica, it has been implemented as the gate dielectric of thin film-based OFET [153-154]. Recently, ultra thin layers of mica have been utilized as the flexible and transparent insulator for organic electronics through a mechanical exfoliation process [155-156]. However, this technique is only very useful and convenient for thin film-based OFET with mica as dielectric. When it comes to nanofiber-based OFET, it involves a very tedious transfer process to integrate the dielectric mica and semiconductor nanofiber into a device [155]. Therefore, mica is not utilized as the gate dielectric of a transistor in this work. Instead, nanofibers grown on a mica substrate are transferred to the micro-scale transistor substrate for subsequent utilization.

One transfer method is based on a gentle stamping process, which is controlled by a linear translation stage. During the transfer, the mica with nanofibers is pressed onto the target platform under controlled temperature and humidity [157]. Another transfer method is based on a roll-over process, in which the nanofibers can be maintained the intrinsic properties and mutual parallel alignment of the fragile nanofibers [89].

3.4.1 Low-temperature study of transferred nanofibers

A study of the PL characteristics at low temperature of the transferred p6P nanofibers has been carried out to investigate if any change occurred to the nanofiber property before and after the roll-over transfer process. Figure 3.17 shows PL spectra from transferred p6P nanofibers taken at various temperatures from 298 K to 6 K. In order to facilitate the comparison with data in literature, the unit of wavelength [nm] has been converted into energy [eV] in the figures of this low-temperature study. The spectra have been analyzed in terms of peak positions, peak widths and peak shifts as a function of temperature [158]. The values obtained are very similar to those found in literature for mica grown nanofibers [148], exhibiting distinct exciton peaks over the whole temperature range. Thus the transferred fibers show no sign of broadening

at intermediate temperatures (which would indicate a phase transition), and also no sign of defect emission. The only hint for an imperfection as compared to plain p6P nanofiber spectra is the low temperature appearance of an additional peak at 3.021 eV, which might be associated to growth contamination, i.e., a second molecular species in the grown nanofibers.

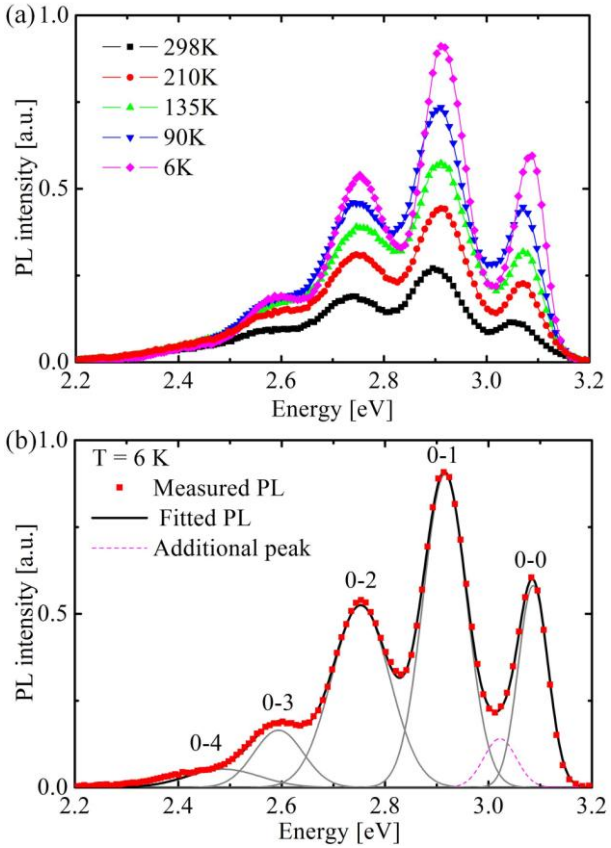

Figure 3.17 (a): PL spectra from transferred fibers recorded at different temperatures. (b): PL spectrum recorded at a temperature of 6 K together with the fitted spectrum consisting of four Gaussian functions and an additional peak as described in the text.

3.4.2 Electroluminescence from transferred nanofibers

The light emission from transferred nanofibers was detected with a Navitar microscope and a Lumenera Infinity1 camera. Figure 3.18 (a) shows the microscope image of a transistor substrate with nanofibers transferred using the stamping method controlled by a linear translation stage. Figure 3.18 (b) shows the light emission from the transferred nanofibers driven by a sinusoidal voltage with V_p = 66 V and f = 200 kHz. The image has been recorded with an integration time of 4 second which makes blue luminescence spots stand out from the background noise where nanofibers bridge across the electrode gap. This suggests that the nanofibers are indeed emitting light, but a more sensitive detection system is required to improve the imaging. This improvement was achieved using an Andor Luca DL-604 EMCCD camera for

OLETs based on roll-over transferred nanofibers [159] and in-situ grown nanofibers. The EL from in-situ grown nanofibers will be presented in the next chapter.

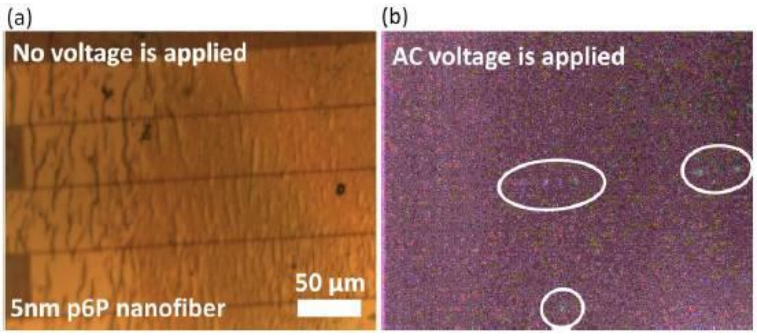

Figure 3.18: Microscope images of a transistor substrate with transferred p6P nanofibers via vertical stamping with light on (a) and observing of electroluminescence with the light off (b).

3.5 Chapter summary

This chapter begins with the light emission investigation using p6P thin film-based micro-scale OLETs, which are driven by AC gate voltage. An operating mechanism in basis of space-charge field assisted charge carrier injection is proposed, based on the time-resolved study, low-temperature experiments and corresponding calculations. The electrical and optical characteristics of the OLETs modified by SAMs are also briefly introduced to show that SAM modification is a promising approach to improve the device performance of the AC-driven OLETs. This operating mechanism can be also applied to OLETs based on other thin films, as well as transferred p6P nanofibers.

Chapter 4: Nano-scale OLETs

It is not straight-forward to transfer different types of organic nanofibers on the same device substrate without affecting the nanofibers mechanically and optically. An alternative approach is to make a transistor with a channel length in the nano-scale, which can facilitate the in-situ growth of nanofibers to bridge across the transistor channel. It has been previously shown that Si/SiO_2-based substrates with Au electrodes patterned by electron beam lithography (EBL) can be used as growth templates to form in-situ grown p6P nanofibers connected to metal electrodes, and that the resulting nanofiber-based OFET exhibits p-type transistor behavior [90]. In this chapter, we investigate the light emission from such in-situ grown nanofibers on EBL fabricated FET platforms [160]. Moreover, the nano-scale devices based on in-situ grown p6P/6T nanofibers are also investigated.

4.1 Preparation of nano-scale transistors

A mix-and-match process was used to fabricate the device platform, where large connecting electrodes and bonding pads were patterned by optical lithography on highly n-doped silicon with 200 nm thermally grown SiO_2 followed by metal evaporation (3 nm Ti/30 nm Au) and lift-off. A window to the underlying silicon, which should act as backgate, was defined by an extra optical lithography step, where SiO_2 was etched until the underlying silicon substrate was reached, followed by another metal evaporation (5 nm Ti/50 nm Au) and lift-off. Nano-scale drain and source electrodes were fabricated by EBL (with an acceleration voltage of 30 keV in 150 nm PMMA resist), metal evaporation (3 nm Ti/30 nm Au), and lift-off. The resulted electrode gap is 150 nm , as shown in Figure 4.1.

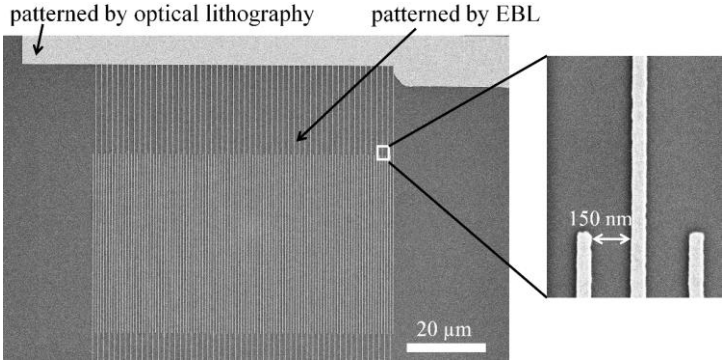

Figure 4.1: SEM (Scanning electron microscope) image of a nano-scale substrate with an electrode gap of 150 nm. The upper contact pad was made by optical lithography, while the interdigitated electrodes were made using EBL.

The substrates were then cleaned by one minute ultrasonic agitation in acetone followed by five minutes rinse in flowing DI-water. After substrate fabrication and cleaning, the p6P nanofibers were directly grown on the device substrates by physical vapor deposition under high-vacuum conditions (~10^{-9} mbar) at a rate of 0.1 Å/s from a Knudsen cell. The substrates were heated to 464 K and the nominal p6P thickness was measured to be 3.5 nm by a cooled quartz microbalance. To prepare substrates with both p6P and 6T nanofibers, the substrates with p6P nanofibers were subsequently transferred into the 6T deposition chamber through atmospheric air to grow the 6T nanofibers (pressure: ~10^{-7} mbar, rate: 0.05 Å/s, substrate temperature 417 K, 6T thickness: 7 nm).

The p6P nanofibers are well separated on the Au electrode structure, as seen in Figure 4.2 (a). The original position of p6P nanofibers cannot be altered by the following deposition of 6T molecules, and the 6T nanofibers can be well distinguished from the previously deposited p6P nanofibers since their morphology is different, as shown in Figure 4.2 (b).

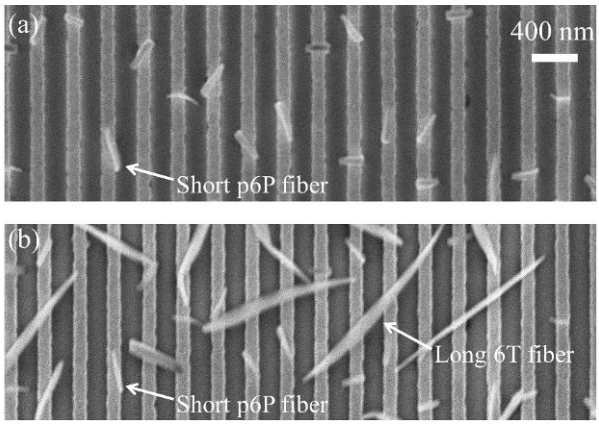

Figure 4.2: SEM images of in-situ grown nanofibers. (a) After p6P deposition. (b) After 6T deposition on the same area where p6P nanofibers had been grown.

Figure 4.3 (a) presents the fluorescence microscope image of in-situ grown p6P nanofibers on the device substrate. Figure 4.3 (b) shows the fluorescence image of the p6P/6T nanofiber device. The corresponding photoluminescence spectra of the p6P nanofiber sample and the p6P/6T nanofiber sample are provided in Figure 4.3 (c). The thickness of the 6T deposition was optimized to be 7 nm in order to obtain an intensity in the orange-red part of the spectrum of comparable magnitude to the p6P spectrum. The three main peaks in the blue regime at 401, 422, and 448 nm correspond to the (0-0), (0-1), and (0-2) vibronic transitions, respectively, in the p6P molecules, while the subsequent 6T molecule deposition results in additional peaks at 530 and 589 nm. The positions of the peaks in the 6T spectrum depend on substrate and deposition conditions, but the peak of 589 nm is likely to appear in all cases [161-163].

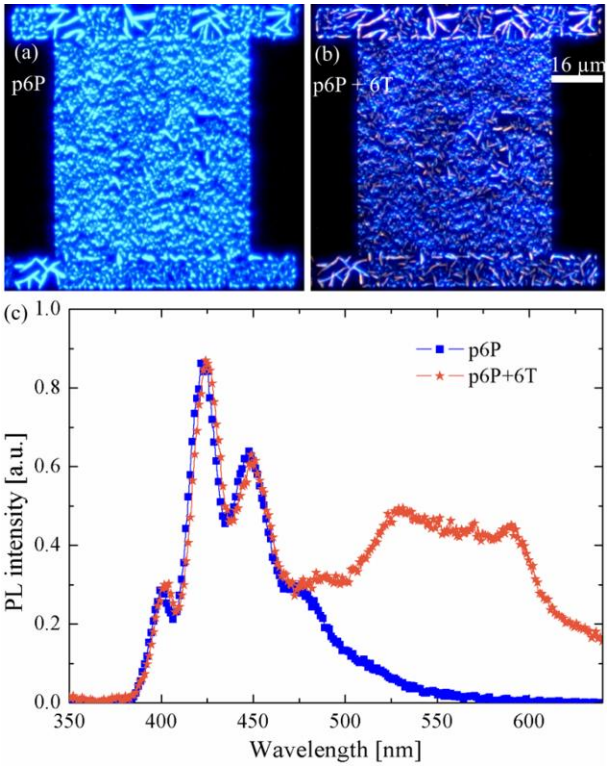

Figure 4.3: Fluorescence microscope image of a p6P nanofiber device (a), and a p6P/6T nanofiber device (b). (c) PL spectra from a p6P nanofiber device and from a p6P/6T nanofiber device after excitation with a 325 nm wavelength laser.

The PL from p6P/6T nanofibers suggest a method to widen the emission spectrum of the nanofiber devices and accurately mix clean colors simply by sequentially growing nanofibers of two different molecules on the same device substrate without changing the emission color of the first discontinuous organic layer. This cannot be accomplished using devices based on multilayer continuous organic thin films, since usually only the bottom continuous organic layer has contact with metal electrodes, and the upper continuous organic layer could partly block the light emission from the bottom layer.

4.2 Electroluminescence from in-situ grown nanofibers

It has been shown that the AC-driven light emission can be obtained from micro-scale OLETs based on organic thin films and transferred nanofibers. The similar operating process and mechanism can be also implemented in nano-scale devices based on in-situ grown nanofibers. The channel length of the nano-scale devices is in the sub-micro regime, which can facilitate the in-situ growth of nanofibers under high vacuum conditions. Figure 4.4 (a) shows the schematic diagram of the circuit along with a nanofiber based device. The electroluminescence was detected with a Navitar microscope and an Andor Luca DL-604 EMCCD camera. Figure 4.4 (b) shows light emission from p6P nanofibers stimulated by grounding source and drain electrodes and applying an AC gate voltage with amplitude of 62.5 V and frequency

of 60 kHz. A bandpass filter between 400 and 500 nm was utilized to confirm that the detected light emission is in the blue spectral range corresponding to the luminescence from p6P. The area marked by a white rectangle in Figure 4.4 (b) is shown in Figure 4.4 (c) as an SEM image, where short in-situ grown p6P nanofibers are scattered on the electrodes. In the lower part of Figure 4.4 (c), the gap between the electrode lines is 150 nm, while in the upper part, the gap is 500 nm. From Figure 4.4 (b) it is seen that light emission is detected only from the upper part where the electrode gap is large, while no light is detected in the area with the small gap. The light emission is the result of the subsequent injection of holes and electrons from the same electrode requiring sufficiently high field strength to be provided at the electrode edge by the gate voltage. Since the field strength depends on the electrode gap, the light intensity is seen to also strongly depend on gap size.

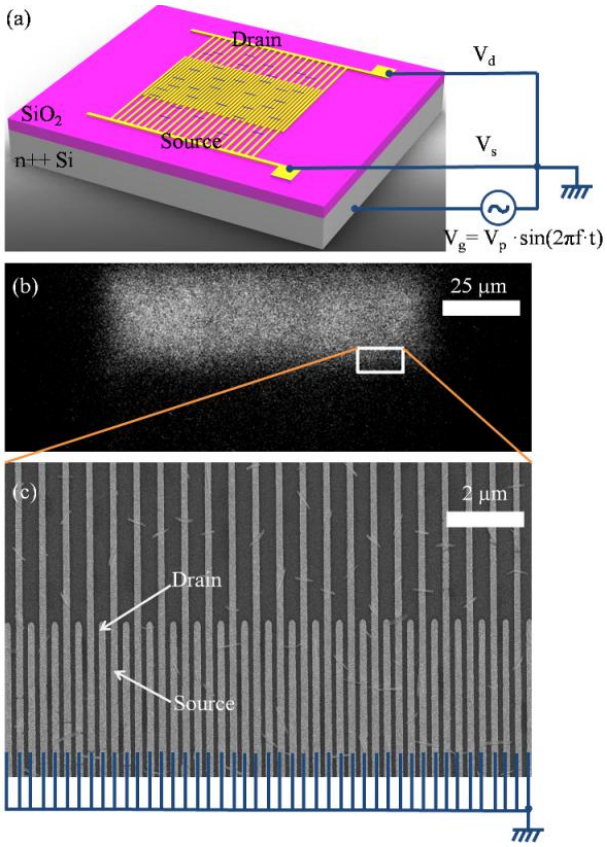

Figure 4.4: (a) Schematic diagram of the operating circuit, together with a p6P nanofiber based bottom contact/bottom gate OLET configuration. (b) Optical image of the device under AC gate voltage biasing while the EBL-fabricated source and drain electrodes were grounded. (c) SEM zoom-in view of the area marked by a white rectangle in (b).

As above mentioned, the light emission intensity from an organic thin film-based OLET depends on the AC gate voltage amplitude and frequency. Figure 4.5 illustrates that the light emission intensity from in-situ grown nanofibers exhibits similar dependencies as the thin film devices. In Figure 4.5 (a), the gate voltage amplitude V_p was varied from 25 V to 62.5 V in steps of 12.5V. The EL intensity

shows a non-linear dependence on the AC gate voltage amplitude. This indicates that an operating mechanism based on SCF assisted electron tunneling can explain the electroluminescence. In Figure 4.5 (b), the gate voltage frequency *f* was increased from 30 kHz to 150 kHz in steps of 30 kHz. The EL intensity increases approximately linearly with the AC gate voltage frequency. The linear dependence of the light emission on the frequency is due to more holes and electrons recombining if more AC voltage cycles are accomplished within a fixed time interval. In order to provide absolute values of EL intensity we have assumed the emission source to be a Lambertian emitter and have implemented the intensity recorded by EMCCD camera and the transmittance as well as the magnification of the optical system.

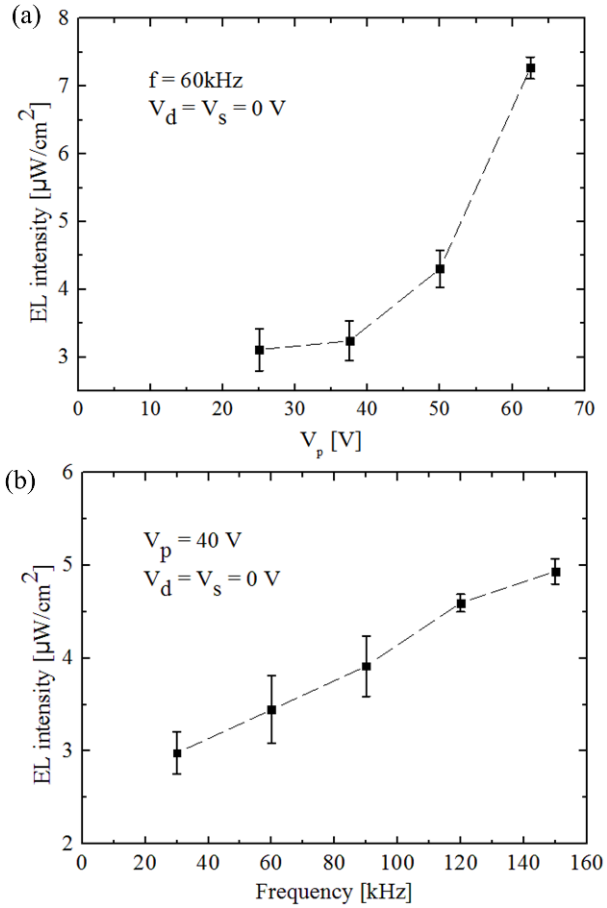

Figure 4.5: EL mission intensity as a function of AC gate voltage amplitude V_p (a) and frequency *f* (b). The measurements were made on one sample and the error bars represent the variation in spatial emission intensity.

Electroluminescence was also obtained from the p6P/6T nanofiber device by applying a gate voltage with amplitude of 45 V and a frequency of 60 kHz. Since the image take by the EMCCD camera appeared the same as that shown in Figure 4.4 (b), the image of the EL from p6P/6T nanofibers is omitted. The emission was characterized only by measuring the intensity due to the fact that the total emitted intensity from the small EBL-defined area was too weak to be reliably detected with

a spectrometer. Two intensity measurements were made, one of total emitted intensity, and one in which a Thorlabs FEL 500 filter (longpass, cut-off wavelength of 500 nm) was inserted into the optical path to detect the contribution from the 6T nanofibers. The contribution of 6T nanofibers was quantified by extracting and comparing the background-excluded signal from three different emission areas and it turned out that the intensity above 500 nm corresponds to approx. 0.6 of the total AC-driven light emission. As the spectrum in Figure 4.3 (c) shows, p6P has some spectral content at wavelengths higher than 500 nm, which would be detected through the filter. However, this part corresponds to only 0.1 of the total intensity. Since the EL data show that more than half of the intensity appears at wavelengths longer than 500 nm, this indicates that color tuning via subsequent in-situ growth of a second type of nanofiber is feasible. This might open up a way to make facile fabricated multi-color devices based on in-situ grown nanofibers, which are suitable for large-area light-emitting components.

4.3 Chapter summary

In-situ grown p6P nanofibers on EBL fabricated device substrates have been utilized to investigate AC-driven electroluminescence. The light emission depends non-linearly on the amplitude of the AC gate voltage and linearly on the frequency of the gate voltage. This similarity to the dependence extracted from thin film-based OLETs indicates that a model involving thermally assisted charge-carrier tunneling can be also applied to the nanofiber based devices. The subsequent in-situ growth of 6T nanofibers on a device substrate with previously deposited p6P nanofibers enables tuning of the photoluminescence spectrum and EL measurements indicate a similar spectral change. Further work could focus on optimizing the nanofiber in-situ growth on the EBL fabricated transistor substrate in order to achieve a higher growth density. A systematic investigation can be carried out on how the relative nominal thickness of the two types of organic materials affects the spectral content.

Chapter 5: OPTs based on thin films and nanofibers

OPTs have been introduced in Section 1.1.3, and the device performance has been greatly improved during the past decade. However, the operating voltage in aforementioned literature regarding OPTs was more than 30 V. In this work, p-type OPTs made of NaT2 nanofibers and thin films with inferior molecular ordering have been fabricated and compared, both of which can be operated at voltage as low as 8 V.

5.1 Experimental

The micro-scale substrate described in Chapter 3 is also used for the OPT application. Figure 5.1 shows the nanofiber OPT configuration and the operating circuit. The electrical characterization both in darkness and under illumination was made using a measurement setup based on a Labview-controlled data acquisition card in combination with a Stanford Research SR 570 current preamplifier and a Falco Systems WMA-280 voltage amplifier. An incandescent light source with a maximum light intensity of 15 mW cm^{-2} was used to characterize the OPTs under illumination. In addition, a He-Ne laser with wavelength of 632.8 nm and a GaN laser with wavelength of 405±5 nm were also used as light sources to characterize the photosensitivity of NaT2. The spectrum of the incandescent light source was recorded using an Ocean Optics spectrometer (Maya 2000Pro) coupled with an optical fiber (QP100-2-UV/VIS). The absorption spectrum of 40 nm NaT2 thin film deposited on quartz glass was measured using a spectroscopic ellipsometer in transmission mode (Ångstrom Sun Technologies SE200BM). All measurements were performed at room temperature in air.

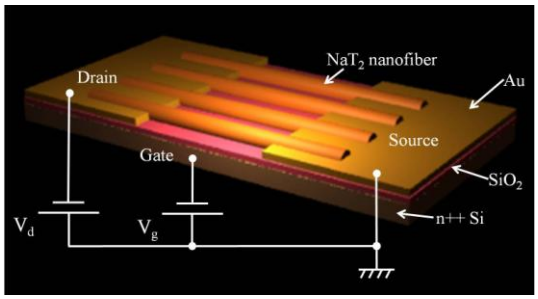

Figure 5.1: Schematic diagram of an OPT configuration based on transferred NaT2 nanofibers and the operating circuit.

Figure 5.2 (a) shows an AFM image of a roll-over transferred NaT2 nanofiber bridging across a transistor channel of an OPT device. The corresponding 3D image of the transferred NaT2 nanofiber in Figure 5.2 (b) illustrates that no obvious damage of nanofiber can be observed after this roll-transfer process.

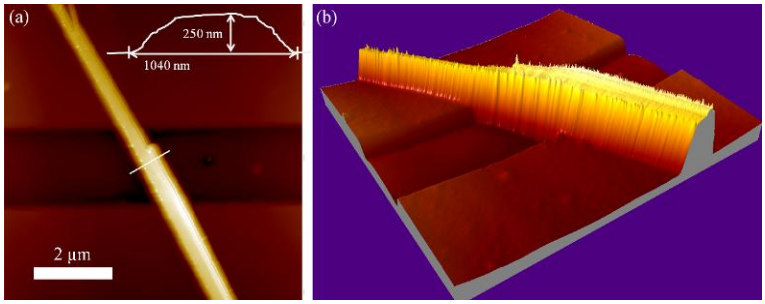

Figure 5.2: (a) AFM image of a transferred NaT2 nanofiber as the active organic semiconductor of an OPT device. Inset: cross section profile. (b) 3D image of the transferred NaT2 nanofiber.

Figure 5.3 (a) compares the output characteristics of a NaT2 nanofiber OPT in darkness and under illumination with the incandescent lamp and an intensity of 15 mW cm^{-2}. The effective channel width W (1.88 mm) of the nanofiber OPT was determined as the sum of the width of the individual nanofibers crossing the transistor channel. The average height of the NaT2 nanofibers was 270 nm as determined by AFM. The drain-source voltage V_{ds} was swept from 0 V to -8 V, and the gate voltage V_g was increased from 0 V to -8 V in steps of 2 V. The drain-source current I_{ds} saturates in this low-voltage operation regime both in darkness and under illumination. In particular, the maximum I_{ds} under illumination with an intensity of 15 mW cm^{-2} is nearly four times the maximum current in darkness, indicating a good photo-response of NaT2 nanofiber OPTs. This can be attributed mainly to the narrow energy gap between the HOMO and LUMO levels of NaT2, which ensures that the incident photons with energy equal to and larger than the energy gap of the semiconductor can be efficiently absorbed, generating pairs of electrons and holes, thus increasing the drain-source current value [67].

Figure 5.3 (b) presents the variation of I_{ds} under illumination with increasing light intensities, while keeping the gate voltage V_g at 0 V. Although current saturation cannot be obtained with V_g at 0 V, the obvious increase of I_{ds} with increasing light intensity clearly indicates that the light source can be regarded as an independent variable replacing the gate electrode to control the output of transistors [77].

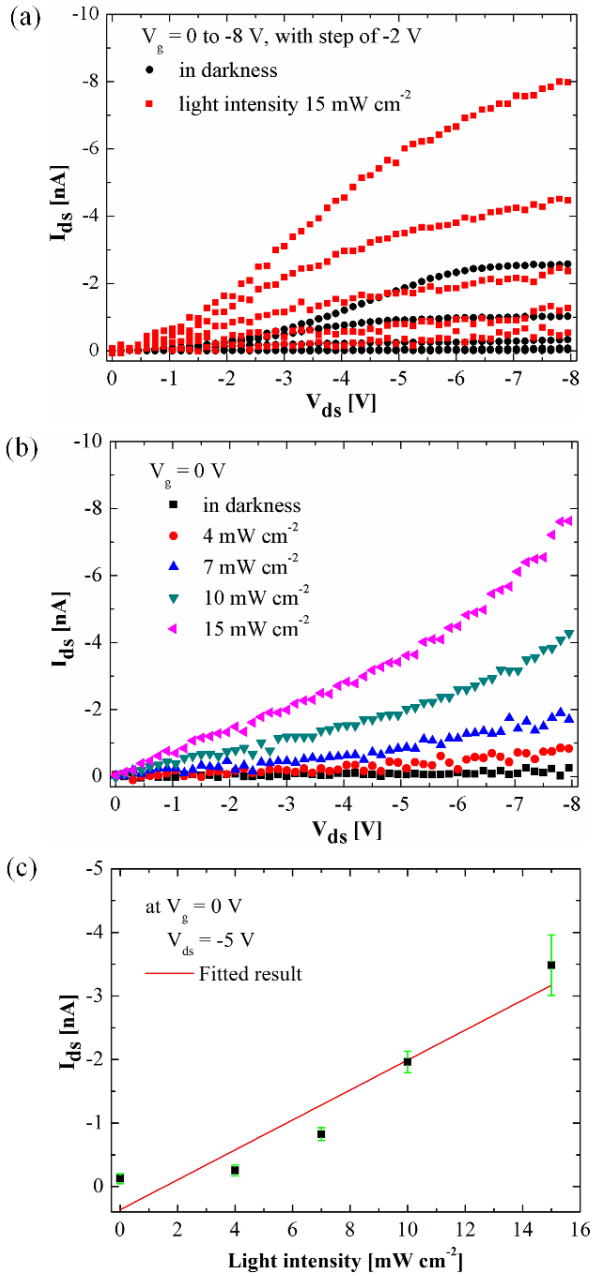

Figure 5.3: (a) Output characteristics of a NaT2 nanofiber OPT in darkness and under illumination with intensity of 15 mW cm^{-2}. (b) Drain-Source current under illumination with various intensities, keeping gate voltage at 0 V. (c) Photo induced drain-source current as a function of incident light power at V_g = 0 V. The error bars represents the variation of different measurements.

Figure 5.3 (c) shows the photo-induced drain-source current as a function of the incident light intensity. The fitted red straight line indicates that the photoconductive effect dominates during the operation by low-voltage biasing when V_g is maintained at 0 V, and the induced photocurrent can be described by $I_{ds} = (q\mu nE)\cdot wD = BP_{inc}$, where q is the elementary charge, μ the hole mobility, n the carrier density, E the electrical field in the transistor channel, w the gate width, D the thickness of the active layer, B the proportionality parameter, and P_{inc} the light intensity of the

incident light [67]. The value of B is determined to be 2.4×10^{-4} mA W^{-1} cm^2 at V_{ds} =-5V when the gate electrode is grounded. Here, the value of B can be correlated with the photoresponsivity (defined in Section 1.1.3) by dividing with the effective device area ($4.3\times10^{-5}cm^2$), which gives a photoresponsivity value of 5.6 mA W^{-1} at V_g = 0V and V_{ds} = -5V.

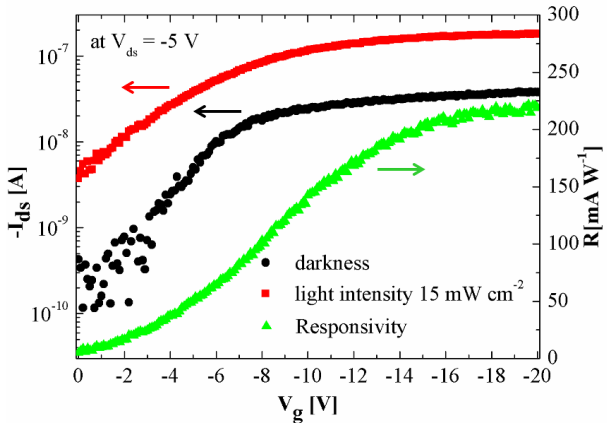

Figure 5.4: On-off current ratio and responsivity of a NaT2 nanofiber OPT.

The transfer characteristics of the NaT2 nanofiber OPTs, both in darkness and under illumination with intensity of 15 mW cm^{-2}, are illustrated in Figure 5.4. The gate voltage V_g was swept from 0 V to -20 V, while keeping the drain voltage V_d at a value of -5 V. The current on-off ratio was approximately 10^2 at the onset voltage V_{on}. The current on-off ratio can be dramatically increased if the drain voltage V_d is extended beyond the low-voltage regime [75-76]. However, the device was only biased in the low-voltage operation regime to avoid sample damage. The low onset voltage V_{on} indicates that charge traps in the vicinity of source electrode are negligible here [53]. The photoresponsivity R of the transferred NaT2 OPT is 5.1 mA W^{-1} at V_g = 0V and V_{ds} = -5V. This is in good agreement with the value (5.6 mA W^{-1}) deduced via the proportionality parameter B divided by the effective device area, illustrated in Figure 5.3 (c). The R value of the transferred NaT2 OPT is 100 mA W^{-1} at the gate voltage V_g = -8V of the low-voltage regime, and it can reach as high as 220 mA W^{-1} when the gate voltage is biased to -20 V. The photoresponsivity we report here is comparable with the values in the literature when the absolute value of the gate voltage is at the low operating regime. For instance, the photoresponsivity of OPTs based on PTCDI-C8 nanowires was approximately 800 mA W^{-1} at a gate voltage of 8 V [76], and the photoresponsivity of OPTs based on BPE-PTCDI nanowires was about 40 mA W^{-1} at V_g = -8V [77]. However, the absolute values of the drain-source voltage V_{ds} were as high as 40 V and 100 V in the literature [75,77], whereas the drain-source voltage we utilized was only 5 V. This suggests that in the low-voltage operation regime, NaT2 in the crystalline form is a competitive candidate to achieve high opto-performance in a transistor configuration.

The hole mobility in the linear regime (V_d = -5V) of the nanofiber OPT in darkness shown in Figure 5.4 can be derived by

$$\mu_{lin} = \frac{\partial I_{ds}}{\partial V_g} \cdot \frac{L}{W \cdot C \cdot V_{ds}} \qquad \text{Eq. (5.1)}$$

where C is the capacitance per unit area of the gate dielectric. The resulting hole mobility of NaT2 nanofiber OPT is ~10^{-5} $cm^2V^{-1}s^{-1}$ which is less than the theoretical prediction using DFT in Chapter 2. In the theoretical calculations, we estimated that the hole mobility of NaT2 should be one order of magnitude less than the hole mobility of pentacene, which has experimentally been shown to exhibit a hole mobility of 10^{-1}~10^{0} $cm^2V^{-1}s^{-1}$ at room temperature [164-165]. However, it should be noted that a perfect crystal with no traps and no defects was assumed in the theoretical calculations. In addition, the experimentally determined value of charge carrier mobility can depend strongly on the deposition parameters of the material and device measuring approaches and can therefore vary by orders of magnitude [54,166]. Moreover, the experimental low mobility can be also resulted from high contact resistance due to non-ohmic injection [95,167].

Thin film-based OPTs were also fabricated to compare with NaT2 nanofiber OPTs. Figure 5.5 (a) illustrates the transfer characteristics of a NaT2 thin film OPT in darkness and under white light illumination at V_{ds} = -5V. The current on-off ratio of the thin film OPTs was similar to that of the NaT2 nanofiber OPTs at the onset voltage. However, the responsivity R of the NaT2 thin film OPTs was only about 2 mA W^{-1} at V_g = -8V, and the responsivity of the NaT2 thin film OPT can only reach about 6 mA W^{-1} when the gate voltage was biased to -20 V. In comparison, the photoresponsivity of NaT2 nanofiber OPT was 100 mA W^{-1} at a gate voltage of V_g = -8V and 220 mA W^{-1} at V_g = -20V, which are approximately 50 times and 36 times higher, respectively, than its thin film counterpart.

The clear improvement of the responsivity of the nanofiber based OPT over the thin film device suggests that the nanofiber based OPTs are promising candidates for highly sensitive nano-scale photoconductive devices. This can be attributed to the enhanced electronic coupling among molecules in the more ordered crystalline structure of the nanofibers, which results in more efficient charge carrier transport [76]. Moreover, to check the effect of the light source wavelength on the photo-characteristics of the organic semiconductor device, the spectrum of the white light source and the absorption spectrum of 40 nm NaT2 thin film deposited on quartz glass have been recorded, as shown in Figure 5.5 (b). The theoretical energy gap of NaT2 corresponds to the wavelength of 564 nm, which is marked by the green dashed line in Figure 5.5 (b). The light intensity summing up from 425 nm to 564 nm of the white light source spectrum illustrated in Figure 5.5 (b) only accounts for 6.7% of the total light intensity, which means the photoresponsivity of the NaT2 nanofiber

OPTs can be significantly enhanced if a light source with a spectrum matched to the absorption is implemented here. To confirm this, in addition to the white light source, a He-Ne laser with an excitation wavelength of 632.8 nm (corresponding to 1.96 eV photon energy) and a GaN laser with a wavelength of 405±5 nm (corresponding to 3.06 eV photon energy) were also utilized to illuminate the OPT separately.

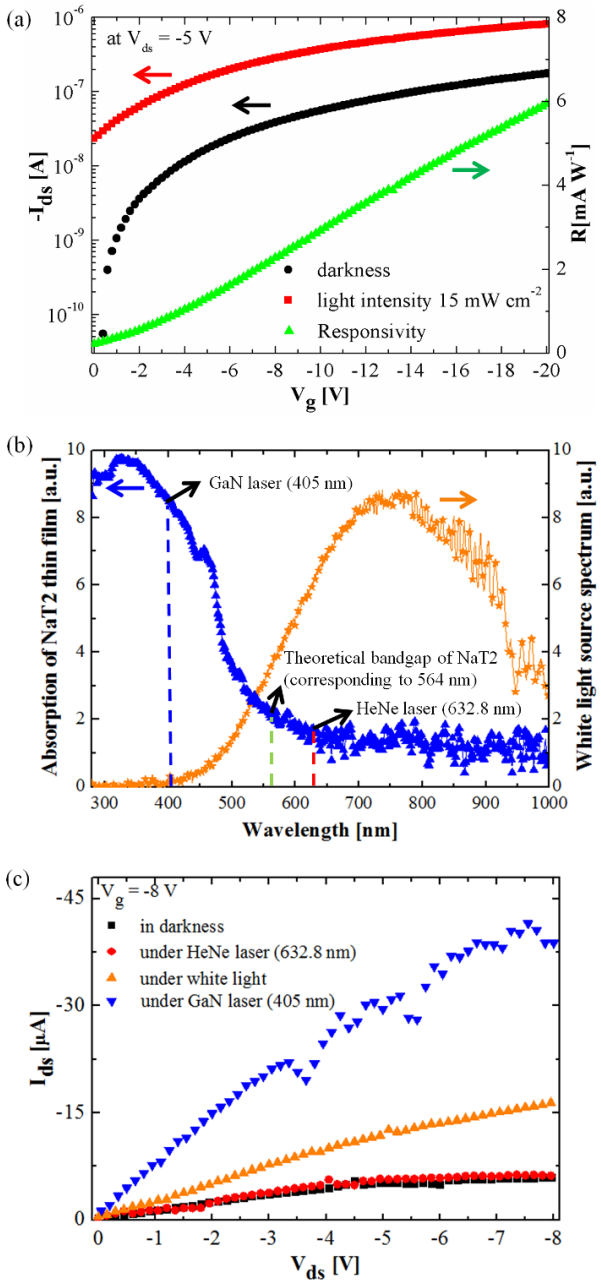

Figure 5.5: (a) Transfer characteristics and responsivity of a NaT2 thin film OPT. (b) Normalized spectrum of the white light source and the absorption spectrum of 40 nm NaT2 thin film deposited on quartz glass. Green line highlights the wavelength of 564 nm (corresponding to theoretical energy gap of NaT2). Blue and red dashed lines highlight the wavelengths of two types of laser source (405 nm and 632.8 nm, respectively). (c) Output characteristics of a NaT2 thin film OPT at V_g = -8V in darkness and under different illuminations.

As shown in the output characteristics in Figure 5.5 (c), under the illumination of the white light source, the drain-source current is more than doubled compared with that in darkness at V_{ds} = -8V. However, even though the intensity of the HeNe laser was tuned to be 24 mW cm^{-2}, which is 60% higher than the maximum light intensity of the white light source (15 mW cm^{-2}), no obvious difference of the drain-source current at V_{ds} = -8V can be observed between the output characteristics of the illuminated and non-illuminated NaT2 thin film-based OPT. This can be explained by the fact that a photon energy of 1.96 eV is not sufficient to generate additional photo carriers to contribute to the drain-source current in the transistor channel. When we utilized the GaN laser with a wavelength of 405 ± 5 nm as another independent light source, however, we could observe an approximately four-fold increase of the drain-source current compared to the current measured in darkness, even though the light intensity of the 405 nm diode laser was tuned to be 8 mW cm^{-2}, which is only half the maximum light intensity of the white light source. Thus, a good matching of the light source spectrum with the absorption spectrum of the organic semiconductor in OPTs is of great importance to maximize the device performance. In particular, a light source spectrum with wavelengths predominantly below 564 nm should be considered to fully match with the absorption spectrum of NaT2.

The ratio of GaN laser-induced drain-source current and the current induced by white light, which can be found from the data in Figure 5.5 (c) as $(I_{GaN} - I_{dark}) / (I_{WL} - I_{dark}) = 3.3 \pm 0.4$, can indicate that the HOMO/LUMO energy gap of NaT2 is underestimated by DFT calculation shown in Figure 2.4. This is because the input number of photons per second and the illumination induced number of holes per second can be correlated as

$$\frac{P_{GaN}}{e_{GaN}} \cdot \alpha_{GaN} = \frac{I_{GaN} - I_{dark}}{q} \qquad \text{Eq. (5.2)}$$

$$\frac{P_{WL}}{e_{WL}} \cdot \alpha_{WL} = \frac{I_{WL} - I_{dark}}{q} \qquad \text{Eq. (5.3)}$$

where P is the input power of the GaN laser or the white light, e is the photon energy, α is the absorption coefficient, I is drain-source current under different illuminating conditions, and q is the elementary charge. From Eq. (5.2) and (5.3), the following equation can be obtained

$$\frac{P_{GaN}}{P_{WL}} \cdot \frac{\alpha_{GaN} / e_{GaN}}{\alpha_{WL} / e_{WL}} = \frac{I_{GaN} - I_{dark}}{I_{WL} - I_{dark}}. \qquad \text{Eq. (5.4)}$$

Since the light intensity integrated from 425 nm to 564 nm of the white light source spectrum in Figure 5.5 (b) only accounts for 6.7% of the total light intensity, the

input power ratio P_{GaN} / P_{WL} is equal to the light intensity ratio $P_{inc}^{GaN} / P_{inc}^{WL}$, which is $8/(15\times 0.067) = 7.96$. The ratio of $(\alpha_{GaN} / e_{GaN}) / (\alpha_{WL} / e_{WL})$ can be determined by integration of the absorption spectrum corresponding to the GaN laser (from 400 nm to 410 nm) and the white light source (from 425 nm to 564 nm), respectively, and this ratio is found to be 0.14. Therefore, using the DFT calculated energy gap (corresponding to 564 nm) of NaT2, the left-hand side of Eq. (5.4) can be determined to be $7.96\times 0.14 \approx 1.1$, which is only 33% of the current ratio. However, as mentioned previously, the theoretical value of the NaT2 energy gap could be underestimated by roughly 10%. Thus, we took the wavelength of 512 nm, corresponding to 2.2×(1+0.1) eV, as another reference point and repeat the above integration process. Following this approach the left-hand side of Eq. (5.4) is determined to be $22.42\times 0.17 \approx 3.8$, which is only 15% larger than the value of the current ratio $(I_{GaN} - I_{dark}) / (I_{WL} - I_{dark})$. Therefore, this suggests that the DFT calculations underestimate the energy gap of NaT2. Moreover, it reveals that the light source wavelength plays an important role in determining the phototransistor performance.

5.2 Chapter summary

OPTs based on transferred NaT2 nanofibers with highly crystallinity and NaT2 thin films with lower molecular ordering have been fabricated and characterized in darkness and under illumination. The obvious superior responsivity of the nanofiber-based OPTs compared with thin film OPTs clearly demonstrates that the transferred NaT2 nanofiber have great potential for high-performance photosensitive devices, mainly attributed to the highly ordered molecular packing in the crystalline structures.

Chapter 6: Conclusions and outlook

Organic light-emitting transistors (OLETs) have the potential to replace organic light-emitting diodes (OLEDs) as the critical components of the next generation light-emitting devices. In the planar configuration of a bottom contact transistor platform, the electroluminescence from recombination of charge carriers can be directly extracted without being blocked by a top metal electrode. The transistor configuration also provides an excellent platform to investigate the charge injection from metal electrode to organic semiconductor.

Organic materials based on small molecules both in the form of thin films and nanofibers have been used in this work as the active organic semiconductor in the transistor platform. The organic thin films can be directly deposited on transistor substrates under high vacuum conditions to form amorphous-like semiconductors. The nanofibers are mainly deposited on particular surface, namely the surface of muscovite mica, to form one dimensional nano-aggregates, and then transferred onto transistor substrates via a directly vertical stamping or a roll-on transfer technique. The photoluminescence from the organic thin films and nanofibers have been characterized mainly using fluorescence microscopy and spectrometer. The main peaks of the photoluminescence spectra are in agreement with the energy difference between HOMO/LUMO levels and their corresponding vibrational energy levels. The emission spectra of transferred p6P nanofibers have also been studied in a temperature dependent manner to show that the nanofibers resemble the good fiber arrays after transfer.

Theoretical investigations have been carried out regarding various small-molecule based organic materials. Density functional theory (DFT) calculations have been performed to estimate and compare the charge carrier transport property and the optical property of the organic materials.

Conventional OLETs are driven by a DC gate voltage together with DC voltage applied to metal electrodes. Electrons and holes are injected from opposite metal electrodes to recombine in the transistor channel to give rise to electroluminescence. Unlike the DC biasing method, the OLETs driven by AC gate voltage have been investigated. In the AC-driven OLETs, charge carriers of opposite polarities can be injected from an individual metal electrode in the different operating regimes of the AC voltage. The injection of one type of charge carriers is facilitated by the space-charge field formed by previously injected charge carriers of the other polarity.

Organic thin films are mainly applied as the active organic semiconductors in the transistor platform to investigate the operating mechanism of the AC-driven OLETs. This operating mechanism is also valid in the organic nanofiber-based OLETs.

Organic phototransistors (OPTs) as the light detectors can be integrated into novel optoelectronic devices, particularly in an OLET-included lab-on-a-chip system. OPTs based on organic nanofibers and thin films have been fabricated and characterized in darkness and under illumination. The obvious superior photoresponsivity of the nanofiber-based OPTs compared with thin film OPTs demonstrates that nanofibers have great potential for high-performance photosensitive devices, mainly attributed to the highly ordered molecular packing in the crystalline structures.

Future work could involve more integration of self-assembled monolayers (SAMs), both in modifying the metal electrode and the semiconductor/dielectric interface, so as to optimize the charge carrier injection and transport. The spatial variation of the emission zone in AC-driven OLETs could be also optimized by the SAMs modification.

The gate dielectric in transistor used in this work is mainly silicon dioxide which prohibits the integration of flexible substrates. In the future, apart from the possibility of utilizing polymer dielectric, ultra thin layers of muscovite mica could be implemented as the gate dielectric of organic nanofiber-based transistors. For fabricating this type of transistors, it is not necessary to firstly deposit organic nanofibers on mica and subsequently transfer the fibers onto transistor platform. Instead, the organic nanofibers can be in-situ grown onto the transistor substrates with thin layers of mica as the dielectric.

As for the application of OPTs, a top contact transistor configuration can be implemented in future work to enhance the charge carrier mobility under low-voltage operation. Besides, a better matching of the light source spectrum with the absorption spectrum of the organic semiconductor should be realized to optimize the device performance.

Appendices

A: List of publications

- *Conduction and electroluminescence from organic continuous and nanofiber thin films*, Jakob Kjelstrup-Hansen, Xuhai Liu, Henrik H. Henrichsen, Kasper Thilsing-Hansen, and Horst-Günter Rubahn, **Physica Status Solidi C**, Vol. 7, Nr. 11-12, 2763-2766 (2010).
- *AC-biased organic light-emitting field-effect transistors from naphthyl end-capped oligothiophenes*, Xuhai Liu, Ivonne Wallmann, Henri Boudinov, Jakob Kjelstrup-Hansen, Manuela Schiek, Arne Lützen, and Horst-Günter Rubahn, **Organic Electronics**, Vol. 11, 1096-1102 (2010).
- *Charge-carrier injection assisted by space-charge field in AC-driven organic light-emitting transistors*, Xuhai Liu, Jakob Kjelstrup-Hansen, Henri Boudinov, and Horst-Günter Rubahn, **Organic Electronics**, Vol. 12, 1724-1730 (2011).
- *Optical properties of microstructured surface-grown and transferred organic nanofibers*, Jakob Kjelstrup-Hansen, Luciana Tavares, Roana Melina de Oliveira Hansen, Xuhai Liu, Kirill Bordo, and Horst-Günter Rubahn, **Journal of Nanophotonics**, Vol. 5, Nr. 051701 (2011).
- *A strain sensor based on an aligned carbon particle string in a UV-cured polymer matrix*, Henrik Høyer, Matti Knaapila, Jakob Kjelstrup-Hansen, Xuhai Liu, and Geir Helgesen, **Applied Physics Letters**, Vol. 99, Nr. 213106 (2011).
- *AC-driven light emission from in-situ grown organic nanofibers*, Xuhai Liu, Jakob Kjelstrup-Hansen, Roana Melina de Oliveira Hansen, Morten Madsen, and Horst-Günter Rubahn, **Proceedings of SPIE**, the International Society for Optical Engineering, Vol. 8435, Nr. 843524 (2012).
- *Organic light-emitting transistors optimized by self-assembled monolayers*, Fei Liu, Jakob Kjelstrup-Hansen, Xuhai Liu, and Horst-Günter Rubahn, **Proceedings of SPIE**, the International Society for Optical Engineering, Vol. 8435, s. 84351C/1-7 (2012).
- *Individual strings of conducting carbon cones and discs in a polymer matrix: Electric field-induced alignment and their use as a strain sensor*, Henrik Høyer, Matti Knaapila, Jakob Kjelstrup-Hansen, Xuhai Liu, and Geir Helgesen, **Journal of Polymer Science, Part B, Polymer Physics**, Vol. 50, Nr. 7, 477-483 (2012).

A.1: Conference participation

- TNT 2009 Trends in NanoTechnology
  Barcelona, Spain Sep. 07-11, 2009
  Presented a poster on “Conduction and electroluminescence from organic continuous and nanofiber thin films”.

- 12th Conference “Advanced Materials and Technologies” and summer school “European Doctorate in Physics and Chemistry of Advanced Materials”
  Palanga, Lithuania Aug. 27-31, 2010
  Presented a poster on “Space-charge assisted electron tunneling in AC-driven organic light emitting transistors”.

- E-MRS Spring Meeting 2011
  Nice, France May. 9-13, 2011
  Oral presentation on “Light emission from organic thin film transistors”.

- SPIE 2012 Photonics Europe
  Brussels, Belgium Apr. 16-19, 2012
  Presented a poster on “AC-driven light emission from in-situ grown organic nanofibers”.

B: Derivations of drain-source current

The drain-source current both in linear and saturation regime of OFETs mentioned in Section 1.1 is derived in the following. The drift current density of organic semiconductors can be determined by Eq. (B.1), in which both of holes and electrons are taken into consideration

$$J = \sigma \cdot E = q \cdot \left(\mu_e N_e + \mu_h N_h \right) \cdot E \qquad \text{Eq. (B.1)}$$

where σ is given by

$$\sigma = \frac{1}{\rho} = q \cdot \left(\mu_e N_e + \mu_h N_h \right). \qquad \text{Eq. (B.2)}$$

σ and ρ are the conductivity and resistivity, respectively; q is the elementary charge; μ_e and μ_h are the electron mobility and the hole mobility, respectively; N_e and N_h are respectively the electron concentration and hole concentration.

Since p-type channel is much more common in practice, it is assumed here that $N_h >> N_e$.

Therefore, we have

$$\rho = \frac{1}{q \cdot \left(\mu_e N_e + \mu_h N_h \right)} \approx \frac{1}{q \cdot \mu_h N_h} \qquad \text{Eq. (B.3)}$$

and

$$J = \sigma \cdot E = \frac{1}{\rho} \cdot E = q \cdot \mu_h N_h \cdot E \,. \qquad \text{Eq. (B.4)}$$

The basic current density is given by the following equations

$$J_e = q \cdot \mu_e N_e E + q D_e \nabla N_e \,, \qquad \text{Eq. (B.5)}$$

$$J_h = q \cdot \mu_h N_h E - q D_h \nabla N_h \,, \qquad \text{Eq. (B.6)}$$

$$J_{total} = J_e + J_h \,. \qquad \text{Eq. (B.7)}$$

The second terms on right-hand side of Eq. (B.5) and Eq. (B.6) are the diffusion components due to the carrier concentration gradient within the channel, which are neglected in above derivations for simplicity.

To further simplify the following discussion, Eq. (B.4) is turned to

$$J = q \cdot \mu \cdot N \cdot E \,. \qquad \text{Eq. (B.8)}$$

Again, neglect the carrier concentration gradient in the channel, the total mobile charge carriers are assumed to occupy a rectangular object with height *H*, and the length and width are the channel length *L* and channel width *W*, respectively. Then, the mobile charge Q_i induced by gate voltage V_g per unit area is

$$Q_i = \frac{Q}{W \cdot L}. \qquad \text{Eq. (B.9)}$$

The mobile charge Q_v per unit volume is

$$Q_v = \frac{Q}{W \cdot L \cdot H} \qquad \text{Eq. (B.10)}$$

where *Q* is the total mobile charge.

On the other hand, the mobile charge Q_v can be defined as

$$Q_v = q \cdot N. \qquad \text{Eq. (B.11)}$$

Combine the above four equations from Eq. (B.8) to Eq. (B.11), we obtain

$$J = q \cdot \mu \cdot N \cdot E = Q_v \cdot \mu \cdot E = \frac{Q_i}{H} \cdot \mu \cdot E = \frac{W \cdot Q_i}{W \cdot H} \cdot \mu \cdot E. \qquad \text{Eq. (B.12)}$$

Finally, the drain to source current can be determined by the following equation

$$I_{ds} = J \cdot W \cdot H = W \cdot Q_i \cdot \mu \cdot E. \qquad \text{Eq. (B.13)}$$

The definition of mobile charge per unit area can be represented by

$$Q_i = C_i \cdot \left(V_g - V_t\right) \qquad \text{Eq. (B.14)}$$

where $V_g - V_t$ is the effective gate voltage.

Take the local potential into consideration, and combining Eq. (B.13) and Eq. (B.14), we obtain

$$I_{ds} = W \cdot C_i \cdot \left(V_g - V_t - V(x)\right) \cdot \mu \cdot \frac{dV}{dx}. \qquad \text{Eq. (B.15)}$$

Move the term *dx* to the left side of this equation and then conduct integration, we get

$$I_{ds} \cdot L = W \cdot C_i \cdot \mu \cdot \left[\left(V_g - V_t\right) \Big|_0^{V_{ds}} - \frac{V^2(x)}{2} \Big|_0^{V_{ds}} \right]. \qquad \text{Eq. (B.16)}$$

Move *L* back to the right hand side,

$$I_{ds} = \frac{W}{L} \cdot C_i \cdot \mu \cdot \left[\left(V_g - V_t\right) \cdot V_{ds} - \frac{V_{ds}^2}{2} \right]. \qquad \text{Eq. (B.17)}$$

Since V_{ds} is much less than V_g in the linear regime, Eq. (B.17) can be simplified by neglecting the second component in the square brackets, hence Eq. (1.2) as follows.

$$I_{ds} = \frac{W}{L} \cdot C_i \cdot \mu_{lin} \cdot \left(V_g - V_t\right) \cdot V_{ds} . \qquad \text{Eq. (1.2)}$$

When it comes to the saturation regime, $V_g - V_t$ can replace V_{ds} due to the channel being pinch-off in Eq. (B.17), therefore the saturation current is obtained

$$I_{ds,sat} = \frac{W}{2L} \cdot C_i \cdot \mu_{sat} \cdot \left(V_g - V_t\right)^2 . \qquad \text{Eq. (1.3)}$$

C: HOMO and LUMO orbitals

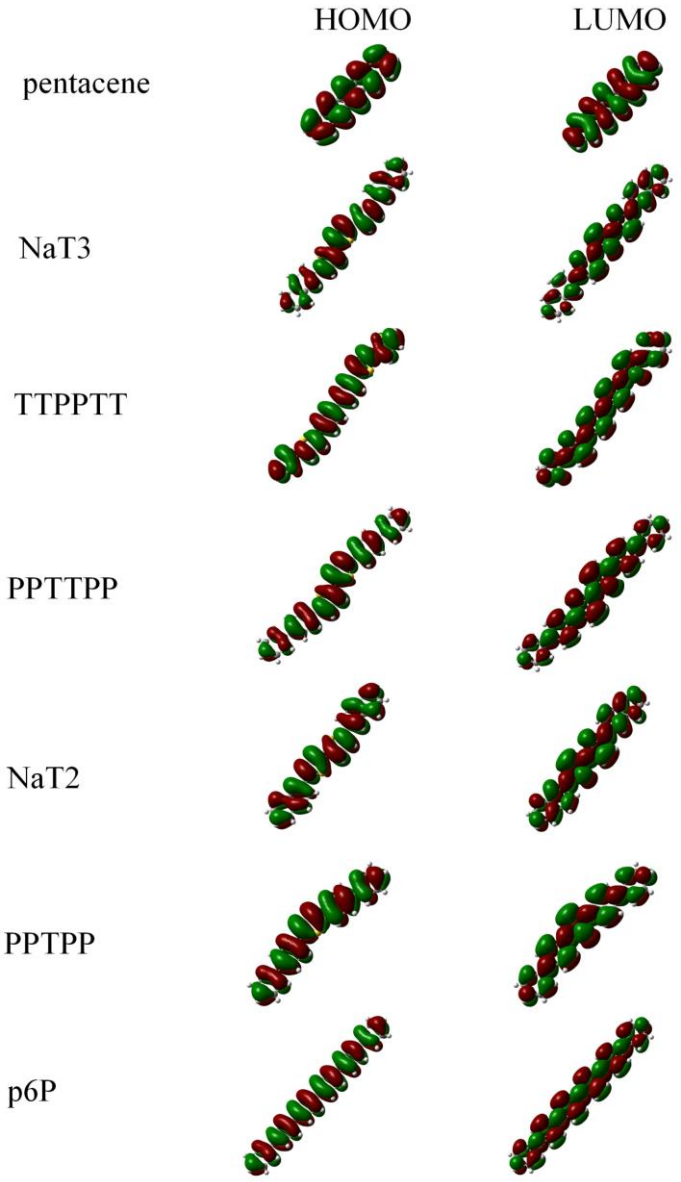

Figure C.1: HOMO and LUMO orbitals of various organic molecules corresponding to the values provided in Section 2.2.1. Green and red color represent the positive and negative orbital isosurfaces, respectively.

D: Micro-scale device fabrication recipe

The micro-scale transistor substrate which is started with a 4-inch Si/SiO2 wafer, is patterned by optical lithography and fabricated through standard cleanroom process. The recipe of making Au electrode is described in the following.

- Hexamethyldisilane (HMDS) treatment for 30 min. in HMDS oven. The HMDS monolayer is the adhesion promoter between SiO2 of the wafer and subsequently deposited photoresist.
- Spincoat of an image reversal photoresist AZ 5214 (paras: 500 rpm for 5 sec.; 4000 rpm for 30 sec.).
- Pre-bake the wafer on hotplate at 100 ℃ for 60 sec.
- UV exposure of the photoresist for 2.5 sec on mask aligner. Note that the exposure time could be altered after equipment maintenance, and new optimized exposure time should be tested in this case.
- Post-bake the wafer on hotplate at 120 ℃ for 100 sec, to make the exposed soluble photoresist insoluble in developer.
- Flood exposure of the photoresist for 30 sec, to make the previously unexposed photoresist soluble in developer.
- Development in AZ 351B at 22 ℃ for 1 min., which is followed by 2 min. water rinse.
- Spin-dry the wafer and deposit Ti/Au using an e-beam evaporator (Cryofox 600) at a rate of 2 Å/sec.
- Lift-off in acetone wet bench, then repeat the rinse and spin-dry process.

The process to fabricate the back gate electrode (see Figure 3.2) is generally the same as the above procedure, except that the SiO2 corresponding to the gate contact pad has to be etched using buffered HF before depositing Ti/Au

E: Extraction of emission intensity of p6P thin film based OLET

The extraction of emission intensity of p6P-based OLET in Section 3.2.3 is presented in the following.

Firstly, a photomultiplier tube (PMT) (Hamamatsu R943-02) as the light detector was calibrated. A He-Ne laser with wavelength of 632.8 nm (input power: 3000 μW) was used as the known light source. A group of filters (three Neutral Density filters and one VBA-200 beam splitter) were used to reduce the laser light input into the PMT. The input number of photons per second and the output number of electrons per second can be correlated as

$$\frac{P_{\text{int}}}{e_0} \cdot G \cdot \eta = \frac{I}{q} \qquad \text{Eq. (E.1)}$$

where P_{int} is the input power, e_0 is the energy of one photon (632.8 nm), q is the elementary charge, I is the output current (monitored by a 610C Solid State Electrometer), η is the quantum efficiency of the PMT. The calibrated gain of the PMT is thus written as

$$G = \frac{I}{P_{\text{int}}} \cdot \frac{e_0}{q} \cdot \frac{1}{\eta} \qquad \text{Eq. (E.2)}$$

where $e_0 = 1.96 \times 1.6 \times 10^{-19}$ J, $I = 1.1 \times 10^{-6}$ A (directly read from the electrometer when the PMT was powered by a voltage of 900 V), η = 14% at the wavelength of 632.8 nm, $q = 1.6 \times 10^{-19}$ A s. P_{int} is the laser power after passing through the filters. Based on the above parameters, the calibrated PMT gain is G = 2600 ±600.

Next, the collecting efficiency of the incident light was estimated. The p6P-based device is assumed as a Lambert emitter, and the luminous intensity of the p6P emitter is defined by the well-known Lambert's cosine law, with peak luminous intensity in the normal direction. The collecting efficiency σ is defined as

$$\sigma = \frac{F_{eff}}{F_{total}} \qquad \text{Eq. (E.3)}$$

where F_{total} is the total luminous flux, which is

$$F_{total} = 2\pi \cdot I_{\max} \int_0^{\pi/2} \frac{\sin(2\theta)}{2} d\theta \qquad \text{Eq. (E.4)}$$

I_{max} is the peak luminous intensity, and θ is the angle between the observer's line of sight and the surface normal. Since the diameter of the collecting lens is 3.5 cm, and the distance between the lens and the p6P emitter is 5 ± 0.5 cm. Therefore, $\theta = 19°$ and the collection efficiency is calculated to be $11 \pm 2\%$ using Eq. (E.3) and (E.4).

Afterwards, the emission area of the p6P device is estimated as follows. The emission area was found as the emission zone length multiplied by the full width at half maximum (FWHM) of the emission zone. The total emission zone length is 3 cm, which was estimated based on the layout of the device effective area. The FWHM was defined as follows: an area was cropped in the optical photograph showing the light emission from a p6P OLET, as illustrated in Figure E.1. This area includes three emission lines (two from both sides of the transistor channel, and the upper one from another side of the metal electrode). Therefore, the distance between the upper and the lower emission lines can be correlated to the number of pixels (M2-M1), which is the sum of one channel length and one metal electrode width (25 μm + 50 μm). Next, the number of pixels corresponding to FWHM was measured, which was then expressed in μm. Three measurements have been performed for relatively bright area, and an average FWHM 4 μm has been determined to be a suitable estimation. Therefore, the total emission area is $3\text{cm} \times 4\mu\text{m} \approx 1 \times 10^{-3}$ cm^2.

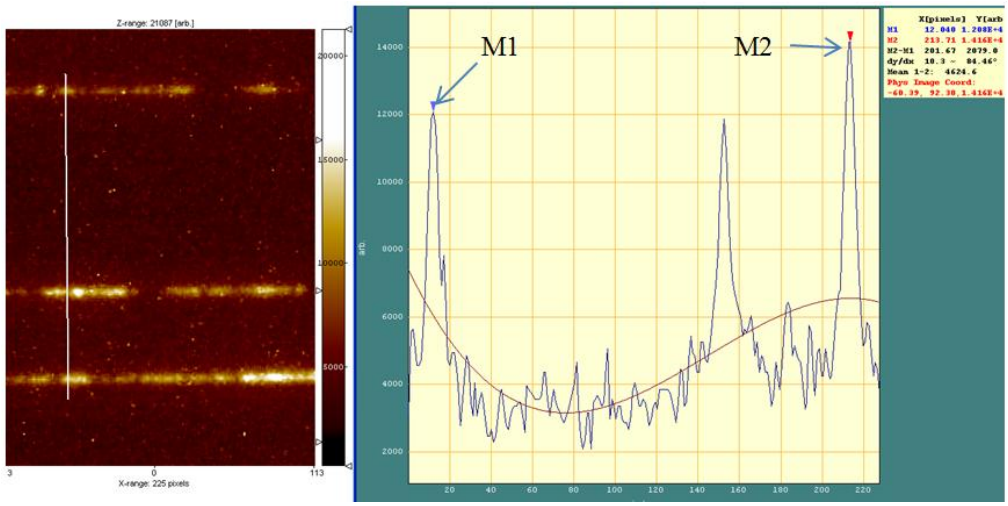

Figure E.1: Light emission from a p6P device read by SPIP.

Finally, the emission output power and the power intensity are calculated in the following. Figure E.2 illustrates the experiment setup to estimate the output power of the light emission from a p6P-based OLET. We focus on the pathway from the p6P emitter to the channel 1 of the oscilloscope, in order to estimate the output power.

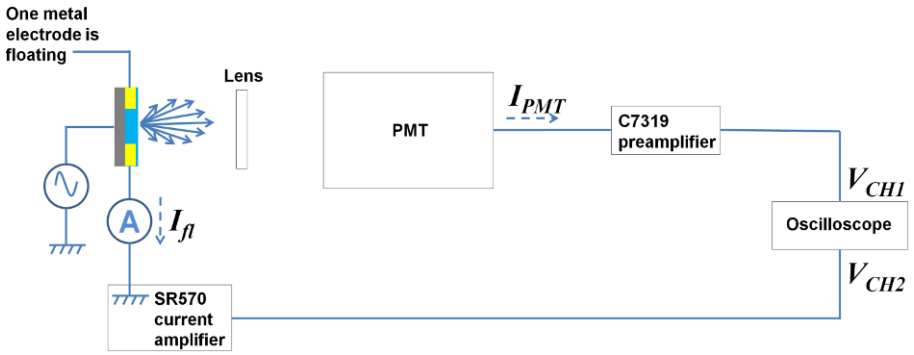

Figure E.2: Schematic illustration of the experimental setup to estimate the output power of the light emission from a p6P-based device.

The input optical power into the PMT can be correlated to the monitored current as follows:

$$P_{\text{int}} = e_0 \cdot N_{photon} = \frac{e_0}{G \cdot \eta \cdot \sigma} \cdot N_{electron} \qquad \text{Eq. (E.5)}$$

where N_{photon} is the number of input photons, and $N_{electron}$ is the number of monitored electrons.

Therefore,

$$P_{\text{int}} = \frac{e_0}{G \cdot \eta \cdot \sigma} \cdot \frac{I}{q} \qquad \text{Eq. (E.6)}$$

Since the wavelength of the main peak of p6P light emission is approximately 425 nm, this gives the energy of one photon $2.92 \times 1.6 \times 10^{-19}$ J. The PMT gain when the PMT was powered by 900 V has already been calibrated as 2600 ± 600. The quantum efficiency of PMT at the wavelength of approximately 425 nm was estimated to be $19 \pm 2\%$, according to the datasheet of the PMT. The collection efficiency has already been calculated to be $11 \pm 2\%$. The elementary charge is 1.6×10^{-19} A s. The output current was integrated during one AC period from the data monitored by oscilloscope. The unit of the readout signal was converted from voltage to current, and the gain of the C7319 DC preamplifier is 10^7 (V/A). The monitored current in one AC period was estimated to be 2×10^{-9} A. Plug the parameters into Eq. (E.6), the P_{int} of the p6P emitter was estimated to be 1×10^{-10} W, which was then divided by the total emission area of 1×10^{-3} cm^2 , so the power intensity is estimated to be 1×10^{-7} W cm^{-2}.

Bibliography

1 Huang, M. H., Mao, S., Feick, H., Yan, H. Q., Wu, Y. Y., Kind, H., Weber, E., Russo, R. & Yang, P. D. Room-temperature ultraviolet nanowire nanolasers. *Science* **292**, 1897-1899, (2001).

2 Huang, Y., Duan, X. F. & Lieber, C. M. Nanowires for integrated multicolor nanophotonics. *Small* **1**, 142-147, (2005).

3 Pettersson, H., Tragardh, J., Persson, A. I., Landin, L., Hessman, D. & Samuelson, L. Infrared photodetectors in heterostructure nanowires. *Nano Letters* **6**, 229-232, (2006).

4 Wang, Z. L. Progress in Piezotronics and Piezo-Phototronics. *Advanced Materials* **24**, 4632-4646, (2012).

5 Sze, S. E. Semiconductor devices: Physics and technology, 2nd ed. *John Wiley&Sons, New York*, (2002).

6 Lee, H., Yoo, G., Yoo, J. S. & Kanicki, J. Asymmetric electrical properties of fork a-Si:H thin-film transistor and its application to flat panel displays. *Journal of Applied Physics* **105**, (2009).

7 Kuo, A., Won, T. K. & Kanicki, J. Advanced amorphous silicon thin-film transistors for AM-OLEDs: Electrical performance and stability. *Ieee Transactions on Electron Devices* **55**, 1621-1629, (2008).

8 Cherenack, K. H., Hekmatshoar, B., Sturm, J. C. & Wagner, S. Self-Aligned Amorphous Silicon Thin-Film Transistors Fabricated on Clear Plastic at 300 degrees C. *Ieee Transactions on Electron Devices* **57**, 2381-2389, (2010).

9 Zhang, D., Choy, W. C. H., Xie, F. X. & Li, X. C. Large-area, high-quality self-assembly electron transport layer for organic optoelectronic devices. *Organic Electronics* **13**, 2042-2046, (2012).

10 Wright, M. & Uddin, A. Organic-inorganic hybrid solar cells: A comparative review. *Sol. Energy Mater. Sol. Cells* **107**, 87-111, (2012).

11 Sirringhaus, H., Tessler, N. & Friend, R. H. Integrated optoelectronic devices based on conjugated polymers. *Science* **280**, 1741-1744, (1998).

12 Sessolo, M. & Bolink, H. J. Hybrid Organic-Inorganic Light-Emitting Diodes. *Advanced Materials* **23**, 1829-1845, (2011).

13 Lipomi, D. J., Lee, J. A., Vosgueritchian, M., Tee, B. C. K., Bolander, J. A. & Bao, Z. A. Electronic Properties of Transparent Conductive Films of PEDOT:PSS on Stretchable Substrates. *Chem. Mat.* **24**, 373-382, (2012).

14 Henson, Z. B., Mullen, K. & Bazan, G. C. Design strategies for organic semiconductors beyond the molecular formula. *Nat. Chem.* **4**, 699-704, (2012).

15 Irimia-Vladu, M., Marjanovic, N., Vlad, A., Ramil, A. M., Hernandez-Sosa, G., Schwodiauer, R., Bauer, S. & Sariciftci, N. S. Vacuum-Processed Polyaniline-C-60 Organic Field Effect Transistors. *Advanced Materials* **20**, 3887-+, (2008).

16 Zhao, Q., Kim, T. H., Park, J. W., Kim, S. O., Jung, S. O., Kim, J. W., Ahn, T., Kim, Y. H., Yi, M. H. & Kwon, S. K. High-Performance Semiconductors based on Alkoxylnaphthyl End-Capped Oligomers for Organic Thin-Film Transistors. *Advanced Materials* **20**, 4868-+, (2008).

17 Sandberg, H. G. O., Backlund, T. G., Osterbacka, R. & Stubb, H. High-performance all-polymer transistor utilizing a hygroscopic insulator. *Advanced Materials* **16**, 1112-+, (2004).

18 Wang, S. H., Kappl, M., Liebewirth, I., Muller, M., Kirchhoff, K., Pisula, W. & Mullen, K. Organic Field-Effect Transistors based on Highly Ordered Single Polymer Fibers. *Advanced Materials* **24**, 417-+, (2012).

19 Cooper, K. P. & Tms. *MATERIALS AND MANUFACTURING CHALLENGES IN HYBRID FLEXIBLE ELECTRONICS*. (Minerals, Metals & Materials Soc, 2010).

20 Fujisaki, Y., Nakajima, Y., Takei, T., Fukagawa, H., Yamamoto, T. & Fujikake, H. Flexible Active-Matrix Organic Light-Emitting Diode Display Using Air-Stable Organic Semiconductor of Dinaphtho 2, 3-b: 2 ', 3 '-f thieno 3, 2-b - thiophene. *Ieee Transactions on Electron Devices* **59**, 3442-3449, (2012).

21 Ramuz, M., Tee, B. C. K., Tok, J. B. H. & Bao, Z. N. Transparent, Optical, Pressure-Sensitive Artificial Skin for Large-Area Stretchable Electronics. *Advanced Materials* **24**, 3223-3227, (2012).

22 Lipomi, D. J., Vosgueritchian, M., Tee, B. C. K., Hellstrom, S. L., Lee, J. A., Fox, C. H. & Bao, Z. N. Skin-like pressure and strain sensors based on transparent elastic films of carbon nanotubes. *Nature Nanotechnology* **6**, 788-792, (2011).

23 Shang, S. M., Zeng, W. & Tao, X. M. High stretchable MWNTs/polyurethane conductive nanocomposites. *Journal of Materials Chemistry* **21**, 7274-7280, (2011).

24 Pais, A., Banerjee, A., Klotzkin, D. & Papautsky, I. High-sensitivity, disposable lab-on-a-chip with thin-film organic electronics for fluorescence detection. *Lab Chip* **8**, 794-800, (2008).

25 Sun, Q. J., Dong, G. F., Wang, L. D. & Qiu, Y. Organic optocouplers. *Sci. China-Chem.* **54**, 1017-1026, (2011).

26 Anthopoulos, T. D., Tanase, C., Setayesh, S., Meijer, E. J., Hummelen, J. C., Blom, P. W. M. & de Leeuw, D. M. Ambipolar organic field-effect transistors based on a solution-processed methanofullerene. *Advanced Materials* **16**, 2174-+, (2004).

27 Baeg, K. J., Noh, Y. Y., Ghim, J., Kang, S. J., Lee, H. & Kim, D. Y. Organic non-volatile memory based on pentacene field-effect transistors using a polymeric gate electret. *Advanced Materials* **18**, 3179-+, (2006).

28 Madec, M. B., Morrison, J. J., Sanchez-Romaguera, V., Turner, M. L. & Yeates, S. G. Organic field effect transistors from ambient solution processed poly(triarylamine)-insulator blends. *Journal of Materials Chemistry* **19**, 6750-6755, (2009).

29 Balzer, F. & Rubahn, H. G. Growth control and optics of organic nanoaggregates. *Advanced Functional Materials* **15**, 17-24, (2005).

30 Kjelstrup-Hansen, J., Boggild, P. & Rubahn, H. G. Charge Injection and Transport in Organic Nanofibers. *Proceedings of the International Conference on Nanoscience and Technology* **61**, 565-569, (2007).

31 Schiek, M., Lutzen, A., Koch, R., Al-Shamery, K., Balzer, F., Frese, R. & Rubahn, H. G. Nanofibers from functionalized para-phenylene molecules. *Applied Physics Letters* **86**, (2005).

32 Bernanose, A. ELECTROLUMINESCENCE OF ORGANIC COMPOUNDS. *British Journal of Applied Physics*, S54-S56, (1955).

33 Bernanose, A., Comte, M. & Vouaux, P. *SUR UN NOUVEAU MODE DEMISSION LUMINEUSE CHEZ CERTAINS COMPOSES ORGANIQUES. *J. Chim. Phys.-Chim. Biol.* **50**, 64-68, (1953).

34 Bernanose, A. & Vouaux, P. *ELECTROLUMINESCENCE ORGANIQUE - ETUDE DU MODE DEMISSION. *J. Chim. Phys.-Chim. Biol.* **50**, 261-&, (1953).

35 Pope, M., Magnante, P. & Kallmann, H. P. ELECTROLUMINESCENCE IN ORGANIC CRYSTALS. *J. Chem. Phys.* **38**, 2042-&, (1963).

36 Tang, C. W. & Vanslyke, S. A. ORGANIC ELECTROLUMINESCENT DIODES. *Applied Physics Letters* **51**, 913-915, (1987).

37 Burroughes, J. H., Bradley, D. D. C., Brown, A. R., Marks, R. N., Mackay, K., Friend, R. H., Burns, P. L. & Holmes, A. B. LIGHT-EMITTING-DIODES BASED ON CONJUGATED POLYMERS. *Nature* **347**, 539-541, (1990).

38 Braun, D. & Heeger, A. J. VISIBLE-LIGHT EMISSION FROM SEMICONDUCTING POLYMER DIODES. *Applied Physics Letters* **58**, 1982-1984, (1991).

39 Braun, D., Moses, D., Zhang, C. & Heeger, A. J. NANOSECOND TRANSIENT ELECTROLUMINESCENCE FROM POLYMER LIGHT-EMITTING-DIODES. *Applied Physics Letters* **61**, 3092-3094, (1992).

40 Sariciftci, N. S., Braun, D., Zhang, C., Srdanov, V. I., Heeger, A. J., Stucky, G. & Wudl, F. SEMICONDUCTING POLYMER-BUCKMINSTERFULLERENE HETEROJUNCTIONS - DIODES, PHOTODIODES, AND PHOTOVOLTAIC CELLS. *Applied Physics Letters* **62**, 585-587, (1993).

41 Budzelaar, F. P. M., Cordes, C. N., Hoppenbrouwers, J. J. L., van der Vaart, N. C., van Beek, W. H. M., Vossen, F. J., Hoevenaars, A. A. M. & Boom, R. G. H. Video processing for active-matrix polymer OLED TV. *J. Soc. Inf. Disp.* **14**, 461-466, (2006).

42 Chen, S. Z., Peng, S. H., Ting, T. Y., Wu, P. S., Lin, C. H., Chang, C. Y., Shyue, J. J. & Jou, J. H. Organic light-emitting diodes with direct contact-printed red, green, blue, and white light-emitting layers. *Applied Physics Letters* **101**, (2012).

43 Fyfe, D. Organic displays come of age. *Nat. Photonics* **3**, 453-455, (2009).

44 Adachi, C., Baldo, M. A., Thompson, M. E. & Forrest, S. R. Nearly 100% internal phosphorescence efficiency in an organic light-emitting device. *Journal of Applied Physics* **90**, 5048-5051, (2001).

45 Cao, Y., Parker, I. D., Yu, G., Zhang, C. & Heeger, A. J. Improved quantum efficiency for electroluminescence in semiconducting polymers. *Nature* **397**, 414-417, (1999).

46 Baldo, M. A., Lamansky, S., Burrows, P. E., Thompson, M. E. & Forrest, S. R. Very high-efficiency green organic light-emitting devices based on electrophosphorescence. *Applied Physics Letters* **75**, 4-6, (1999).

47 Endo, A., Ogasawara, M., Takahashi, A., Yokoyama, D., Kato, Y. & Adachi, C. Thermally Activated Delayed Fluorescence from Sn4+-Porphyrin Complexes

and Their Application to Organic Light-Emitting Diodes - A Novel Mechanism for Electroluminescence. *Advanced Materials* **21**, 4802-+, (2009).

48 Endo, A., Sato, K., Yoshimura, K., Kai, T., Kawada, A., Miyazaki, H. & Adachi, C. Efficient up-conversion of triplet excitons into a singlet state and its application for organic light emitting diodes. *Applied Physics Letters* **98**, (2011).

49 Uoyama, H., Goushi, K., Shizu, K., Nomura, H. & Adachi, C. Highly efficient organic light-emitting diodes from delayed fluorescence. *Nature* **492**, 234-+, (2012).

50 Mizukami, M., Hirohata, N., Iseki, T., Ohtawara, K., Tada, T., Yagyu, S., Abe, T., Suzuki, T., Fujisaki, Y., Inoue, Y., Tokito, S. & Kurita, T. Flexible AM OLED panel driven by bottom-contact OTFTs. *IEEE Electron Device Lett.* **27**, 249-251, (2006).

51 Zhou, L. S., Park, S. N., Bai, B., Sun, J., Wu, S. C., Jackson, T. N., Nelson, S., Freeman, D. & Hong, Y. Pentacene TFT driven AM OLED displays. *IEEE Electron Device Lett.* **26**, 640-642, (2005).

52 Muccini, M. A bright future for organic field-effect transistors. *Nature Materials* **5**, 605-613, (2006).

53 Zaumseil, J. & Sirringhaus, H. Electron and ambipolar transport in organic field-effect transistors. *Chemical Reviews* **107**, 1296-1323, (2007).

54 Hepp, A., Heil, H., Weise, W., Ahles, M., Schmechel, R. & von Seggern, H. Light-Emitting Field-Effect Transistor Based on a Tetracene Thin Film. *Physical Review Letters* **91**, 157406, (2003).

55 Capelli, R., Toffanin, S., Generali, G., Usta, H., Facchetti, A. & Muccini, M. Organic light-emitting transistors with an efficiency that outperforms the equivalent light-emitting diodes. *Nature Materials* **9**, 496-503, (2010).

56 Anthopoulos, T. D., Singh, B., Marjanovic, N., Sariciftci, N. S., Ramil, A. M., Sitter, H., Colle, M. & de Leeuw, D. M. High performance n-channel organic field-effect transistors and ring oscillators based on C-60 fullerene films. *Applied Physics Letters* **89**, (2006).

57 Babel, A., Wind, J. D. & Jenekhe, S. A. Ambipolar charge transport in air-stable polymer blend thin-film transistors. *Advanced Functional Materials* **14**, 891-898, (2004).

58 Zaumseil, J., Friend, R. H. & Sirringhaus, H. Spatial control of the recombination zone in an ambipolar light-emitting organic transistor. *Nature Materials* **5**, 69-74, (2006).

59 Yamao, T., Shimizu, Y., Terasaki, K. & Hotta, S. Organic Light-Emitting Field-Effect Transistors Operated by Alternating-Current Gate Voltages. *Advanced Materials* **20**, 4109-+, (2008).

60 Yamao, T., Sakurai, Y., Terasaki, K., Shimizu, Y., Jinnai, H. & Hotta, S. Current-Injected Spectrally-Narrowed Emissions from an Organic Transistor. *Advanced Materials* **22**, 3708-+, (2010).

61 Yamao, T., Terasaki, K., Shimizu, Y. & Hotta, S. Organic-Crystal Light-Emitting Field-Effect Transistors Driven by Square-Wave Gate Voltages. *Journal of Nanoscience and Nanotechnology* **10**, 1017-1020, (2010).

62 Kjelstrup-Hansen, J., Liu, X., Henrichsen, H. H., Thilsing-Hansen, K. & Rubahn, H.-G. Conduction and electroluminescence from organic continuous and nanofiber thin films. *physica status solidi (c)* **7**, 2763-2766, (2010).

63 Liu, X., Kjelstrup-Hansen, J., Boudinov, H. & Rubahn, H.-G. Charge-carrier injection assisted by space-charge field in AC-driven organic light-emitting transistors. *Organic Electronics* **12**, 1724-1730, (2011).

64 Liu, X., Wallmann, I., Boudinov, H., Kjelstrup-Hansen, J., Schiek, M., Luetzen, A. & Rubahn, H.-G. AC-biased organic light-emitting field-effect transistors from naphthyl end-capped oligothiophenes. *Organic Electronics* **11**, 1096-1102, (2010).

65 Liu, X. H., Kjelstrup-Hansen, J., Hansen, R. M. D., Madsen, M. & Rubahn, H. G. AC-driven light emission from in-situ grown organic nanofibers. *Proceedings of SPIE* **8435**, 843524, (2012).

66 Ohtsuka, Y., Ishizumi, A. & Yanagi, H. Light-emitting field-effect transistors with pi-conjugated liquid crystalline polymer driven by AC-gate voltages. *Organic Electronics* **13**, 1710-1715, (2012).

67 Dong, H. L., Li, H. X., Wang, E. J., Nakashima, H., Torimitsu, K. & Hu, W. P. Phototransistors of a Rigid Rod Conjugated Polymer. *Journal of Physical Chemistry C* **112**, 19690-19693, (2008).

68 Guo, X. F., Xiao, S. X., Myers, M., Miao, Q., Steigerwald, M. L. & Nuckolls, C. Photoresponsive nanoscale columnar transistors. *Proceedings of the National Academy of Sciences of the United States of America* **106**, 691-696, (2009).

69 Konstantatos, G., Badioli, M., Gaudreau, L., Osmond, J., Bernechea, M., de Arquer, F. P. G., Gatti, F. & Koppens, F. H. L. Hybrid graphene-quantum dot phototransistors with ultrahigh gain. *Nature Nanotechnology* **7**, 363-368, (2012).

70 Noh, Y. Y., Kim, D. Y., Yoshida, Y., Yase, K., Jung, B. J., Lim, E. & Shim, H. K. High-photosensitivity p-channel organic phototransistors based on a biphenyl end-capped fused bithiophene oligomer. *Applied Physics Letters* **86**, (2005).

71 Saragi, T. P. I., Pudzich, R., Fuhrmann, T. & Salbeck, J. Organic phototransistor based on intramolecular charge transfer in a bifunctional spiro compound. *Applied Physics Letters* **84**, 2334-2336, (2004).

72 Cho, M. Y., Kim, S. J., Han, Y. D., Park, D. H., Kim, K. H., Choi, D. H. & Joo, J. Highly Sensitive, Photocontrolled, Organic Thin-Film Transistors Using Soluble Star-shaped Conjugated Molecules. *Advanced Functional Materials* **18**, 2905-2912, (2008).

73 Kim, C. H., Kim, S. H., Lee, S. H., Han, S. H., Choi, M. H., Jeon, T. W. & Jang, J. Bimolecular recombination in solution-processed 6, 13-bis(pentylphenylethynyl) pentacene thin-film transistor. *Applied Physics Letters* **94**, (2009).

74 Mas-Torrent, M., Hadley, P., Crivillers, N., Veciana, J. & Rovira, C. Large photoresponsivity in high-mobility single-crystal organic field-effect phototransistors. *ChemPhysChem* **7**, 86-88, (2006).

75 Tang, Q. X., Li, L. Q., Song, Y. B., Liu, Y. L., Li, H. X., Xu, W., Liu, Y. Q., Hu, W. P. & Zhu, D. B. Photoswitches and phototransistors from organic single-crystalline sub-micro/nanometer ribbons. *Advanced Materials* **19**, 2624-+, (2007).

76 Mukherjee, B., Sim, K., Shin, T. J., Lee, J., Mukherjee, M., Ree, M. & Pyo, S. Organic phototransistors based on solution grown, ordered single crystalline arrays of a pi-conjugated molecule. *Journal of Materials Chemistry* **22**, 3192-3200, (2012).

77 Yu, H., Bao, Z. & Oh, J. H. High-performace phototransistors based on single-crystalline n-channel organic nanowires and photogenerated charge-carrier behaviors. *Adv. Funct. Mater.*, (2012).

78 Ito, K., Suzuki, T., Sakamoto, Y., Kubota, D., Inoue, Y., Sato, F. & Tokito, S. Oligo(2,6-anthrylene)s: Acene-oligomer approach for organic field-effect transistors. *Angew. Chem.-Int. Edit.* **42**, 1159-1162, (2003).

79 Simonsen, A. C. & Rubahn, H. G. Local spectroscopy of individual hexaphenyl nanofibers. *Nano Letters* **2**, 1379-1382, (2002).

80 Sundar, V. C., Zaumseil, J., Podzorov, V., Menard, E., Willett, R. L., Someya, T., Gershenson, M. E. & Rogers, J. A. Elastomeric transistor stamps: Reversible probing of charge transport in organic crystals. *Science* **303**, 1644-1646, (2004).

81 Mizokuro, T., Takeuchi, K., Heck, C., Aota, H. & Tanigaki, N. Orientation management of alpha-sexithiophene layer for the application in organic photovoltaic devices. *Organic Electronics* **13**, 3130-3137, (2012).

82 Jurchescu, O. D., Baas, J. & Palstra, T. T. M. Effect of impurities on the mobility of single crystal pentacene. *Applied Physics Letters* **84**, 3061-3063, (2004).

83 Klauk, H., Halik, M., Zschieschang, U., Schmid, G., Radlik, W. & Weber, W. High-mobility polymer gate dielectric pentacene thin film transistors. *Journal of Applied Physics* **92**, 5259-5263, (2002).

84 Hotta, S. & Yamao, T. The thiophene/phenylene co-oligomers: exotic molecular semiconductors integrating high-performance electronic and optical functionalities. *Journal of Materials Chemistry* **21**, 1295-1304, (2011).

85 Tian, H., Shi, J., He, B., Hu, N., Dong, S., Yan, D., Zhang, J., Geng, Y. & Wang, F. Naphthyl and thionaphthyl end-capped oligothiophenes as organic semiconductors: Effect of chain length and end-capping groups. *Advanced Functional Materials* **17**, 1940-1951, (2007).

86 Schiek, M., Balzer, F., Al-Shamery, K., Lutzen, A. & Rubahn, H. G. Nanoaggregates from Thiophene/Phenylene Co-Oligomers. *Journal of Physical Chemistry C* **113**, 9601-9608, (2009).

87 Yanagi, H., Araki, Y., Ohara, T., Hotta, S., Ichikawa, M. & Taniguchi, Y. Comparative carrier transport characteristics in organic field-effect transistors with vapor-deposited thin films and epitaxially grown crystals of biphenyl-capped thiophene oligomers. *Advanced Functional Materials* **13**, 767-773, (2003).

88 Shamery, K. A., Rubahn, H. G. & Sitter, H. Organic Nanostructures for Next Generation Devices. *Springer ISBN 978-3-540-71922-9*, (2008).

89 Tavares, L., Kjelstrup-Hansen, J. & Rubahn, H. G. Efficient Roll-On Transfer Technique for Well-Aligned Organic Nanofibers. *Small* **7**, 2460-2463, (2011).

90 Hansen, R. M. d. O., Madsen, M., Kjelstrup-Hansen, J. & Rubahn, H.-G. In situ-Directed Growth of Organic Nanofibers and Nanoflakes: Electrical and Morphological Properties. *Nanoscale Research Letters* **6:11**, (2011).

91 Ishii, H., Sugiyama, K., Ito, E. & Seki, K. Energy level alignment and interfacial electronic structures at organic metal and organic organic interfaces. *Advanced Materials* **11**, 605-+, (1999).

92 Guha, S., Rice, J. D., Yau, Y. T., Martin, C. M., Chandrasekhar, M., Chandrasekhar, H. R., Guentner, R., de Freitas, P. S. & Scherf, U. Temperature-dependent photoluminescence of organic semiconductors with varying backbone conformation. *Physical Review B* **67**, (2003).

93 Sanchez-Carrera, R. S., Delgado, M. C. R., Ferron, C. C., Osuna, R. M., Hernandez, V., Navarrete, J. T. L. & Aspuru-Guzik, A. Optical absorption and emission properties of end-capped oligothienoacenes: A joint theoretical and experimental study. *Organic Electronics* **11**, 1701-1712, (2010).

94 Pope, M. Electronic processes in organic crystals and polymers; 2nd ed. *Oxford University Press ISBN: 978-0195129632*, (1999).

95 Gruber, M., Schurrer, F. & Zojer, K. Relation between injection barrier and contact resistance in top-contact organic thin-film transistors. *Organic Electronics* **13**, 1887-1899, (2012).

96 Scheinert, S. & Paasch, G. Interdependence of contact properties and field- and density-dependent mobility in organic field-effect transistors. *Journal of Applied Physics* **105**, (2009).

97 Acton, O., Dubey, M., Weidner, T., O'Malley, K. M., Kim, T. W., Ting, G. G., Hutchins, D., Baio, J. E., Lovejoy, T. C., Gage, A. H., Castner, D. G., Ma, H. & Jen, A. K. Y. Simultaneous Modification of Bottom-Contact Electrode and Dielectric Surfaces for Organic Thin-Film Transistors Through Single-Component Spin-Cast Monolayers. *Advanced Functional Materials* **21**, 1476-1488, (2011).

98 Cheng, X. Y., Noh, Y. Y., Wang, J. P., Tello, M., Frisch, J., Blum, R. P., Vollmer, A., Rabe, J. P., Koch, N. & Sirringhaus, H. Controlling Electron and Hole Charge Injection in Ambipolar Organic Field-Effect Transistors by Self-Assembled Monolayers. *Advanced Functional Materials* **19**, 2407-2415, (2009).

99 Nouchi, R. & Kubozono, Y. Anomalous hysteresis in organic field-effect transistors with SAM-modified electrodes: Structural switching of SAMs by electric field. *Organic Electronics* **11**, 1025-1030, (2010).

100 de Boer, B., Hadipour, A., Mandoc, M. M., van Woudenbergh, T. & Blom, P. W. M. Tuning of metal work functions with self-assembled monolayers. *Advanced Materials* **17**, 621-+, (2005).

101 Noh, J., Kato, H. S., Kawai, M. & Hara, M. Surface structure and interface dynamics of alkanethiol self-assembled monolayers on Au(111). *J. Phys. Chem. B* **110**, 2793-2797, (2006).

102 Oncins, G., Vericat, C. & Sanz, F. Mechanical properties of alkanethiol monolayers studied by force spectroscopy. *J. Chem. Phys.* **128**, (2008).

103 Ge, Y. & Whitten, J. E. Interfacial electronic properties of thiophene and sexithiophene adsorbed on a fluorinated alkanethiol monolayer. *Journal of Physical Chemistry C* **112**, 1174-1182, (2008).

104 Iwami, Y., Hobara, D., Yamamoto, M. & Kakiuchi, T. Determination of the potential of zero charge of Au(111) electrodes modified with thiol self-assembled monolayers using a potential-controlled sessile drop method. *J. Electroanal. Chem.* **564**, 77-83, (2004).

105 Liu, F., Kjelstrup-Hansen, J., Liu, X. H. & Rubahn, H. G. Organic light-emitting transistors optimized by self-assembled monolayers. *Proceedings of SPIE* **8435**, (2012).

106 Hwang, J., Wan, A. & Kahn, A. Energetics of metal-organic interfaces: New experiments and assessment of the field. *Mater. Sci. Eng. R-Rep.* **64**, 1-31, (2009).

107 Kahn, A., Koch, N. & Gao, W. Y. Electronic structure and electrical properties of interfaces between metals and pi-conjugated molecular films. *J. Polym. Sci. Pt. B-Polym. Phys.* **41**, 2529-2548, (2003).

108 Arkhipov, V. I., Wolf, U. & Bassler, H. Current injection from a metal to a disordered hopping system. II. Comparison between analytic theory and simulation. *Physical Review B* **59**, 7514-7520, (1999).

109 Scott, J. C. Metal-organic interface and charge injection in organic electronic devices. *Journal of Vacuum Science & Technology A* **21**, 521-531, (2003).

110 Shen, Y. L., Hosseini, A. R., Wong, M. H. & Malliaras, G. G. How to make ohmic contacts to organic semiconductors. *ChemPhysChem* **5**, 16-25, (2004).

111 Richardson, O. W. The distribution of the molecules of a gas in a field of force, with applications to the theory of electrons. *Philos. Mag.* **28**, 633-647, (1914).

112 Crowell, C. R. & Sze, S. M. CURRENT TRANSPORT IN METAL-SEMICONDUCTOR BARRIERS. *Solid-State Electron.* **9**, 1035-&, (1966).

113 Schottky, W. Simplified and advanced Theory of the Boundary Layer Rectifiers. *Z. Phys.* **118**, 539-592, (1942).

114 Arkhipov, V. I., Emelianova, E. V., Tak, Y. H. & Bassler, H. Charge injection into light-emitting diodes: Theory and experiment. *Journal of Applied Physics* **84**, 848-856, (1998).

115 Bassler, H. CHARGE TRANSPORT IN DISORDERED ORGANIC PHOTOCONDUCTORS - A MONTE-CARLO SIMULATION STUDY. *Phys. Status Solidi B-Basic Res.* **175**, 15-56, (1993).

116 Wan, A., Hwang, J., Amy, F. & Kahn, A. Impact of electrode contamination on the alpha-NPD/Au hole injection barrier. *Organic Electronics* **6**, 47-54, (2005).

117 Walters, R. J., Bourianoff, G. I. & Atwater, H. A. Field-effect electroluminescence in silicon nanocrystals. *Nature Materials* **4**, 143-146, (2005).

118 Blouin, N., Michaud, A., Gendron, D., Wakim, S., Blair, E., Neagu-Plesu, R., Belletete, M., Durocher, G., Tao, Y. & Leclerc, M. Toward a rational design of poly(2,7-carbazole) derivatives for solar cells. *Journal of the American Chemical Society* **130**, 732-742, (2008).

119 Irfan, A., Ijaz, F., Al-Sehemi, A. G. & Asiri, A. M. Quantum chemical approach toward rational designing of highly efficient oxadiazole based oligomers used in organic field effect transistors. *J. Comput. Electron.* **11**, 374-384, (2012).

120 Lin, B. C., Cheng, C. P. & Lao, Z. P. M. Reorganization energies in the transports of holes and electrons in organic amines in organic electroluminescence studied by density functional theory. *J. Phys. Chem. A* **107**, 5241-5251, (2003).

121 Podzorov, V. & Gershenson, M. E. Photoinduced charge transfer across the interface between organic molecular crystals and polymers. *Physical Review Letters* **95**, (2005).

122 Toufik, H., Bouzzine, S. M., Ninis, O., Lamchouri, F., Aberkane, M., Hamidi, M. & Bouachrine, M. Opto-electronic properties and molecular design of new materials based on pyrrole studied by DFT. *Res. Chem. Intermed.* **38**, 1375-1388, (2012).

123 Jensen, F. Introduction to computational chemistry, 2nd ed. *Wiley ISBN: 978-0470011874* (2007).

124 Gaussian 09, R. A., M. J. Frisch, G. W. Trucks, H. B. Schlegel, G. E. Scuseria, M. A. Robb, J. R. Cheeseman, G. Scalmani, V. Barone, B. Mennucci, G. A. Petersson, H. Nakatsuji, M. Caricato, X. Li, H. P. Hratchian, A. F. Izmaylov, J. Bloino, G. Zheng, J. L. Sonnenberg, M. Hada, M. Ehara, K. Toyota, R. Fukuda,

J. Hasegawa, M. Ishida, T. Nakajima, Y. Honda, O. Kitao, H. Nakai, T. Vreven, J. A. Montgomery, Jr., J. E. Peralta, F. Ogliaro, M. Bearpark, J. J. Heyd, E. Brothers, K. N. Kudin, V. N. Staroverov, R. Kobayashi, J. Normand, K. Raghavachari, A. Rendell, J. C. Burant, S. S. Iyengar, J. Tomasi, M. Cossi, N. Rega, J. M. Millam, M. Klene, J. E. Knox, J. B. Cross, V. Bakken, C. Adamo, J. Jaramillo, R. Gomperts, R. E. Stratmann, O. Yazyev, A. J. Austin, R. Cammi, C. Pomelli, J. W. Ochterski, R. L. Martin, K. Morokuma, V. G. Zakrzewski, G. A. Voth, P. Salvador, J. J. Dannenberg, S. Dapprich, A. D. Daniels, O. Farkas, J. B. Foresman, J. V. Ortiz, J. Cioslowski, D. J. Fox. *Gaussian, Inc., Wallingford CT*, (2009).

125 Marcus, R. A. ELECTRON-TRANSFER REACTIONS IN CHEMISTRY - THEORY AND EXPERIMENT. *Reviews of Modern Physics* **65**, 599-610, (1993).

126 Valeev, E. F., Coropceanu, V., da Silva, D. A., Salman, S. & Bredas, J. L. Effect of electronic polarization on charge-transport parameters in molecular organic semiconductors. *Journal of the American Chemical Society* **128**, 9882-9886, (2006).

127 Bredas, J. L., Beljonne, D., Coropceanu, V. & Cornil, J. Charge-transfer and energy-transfer processes in pi-conjugated oligomers and polymers: A molecular picture. *Chemical Reviews* **104**, 4971-5003, (2004).

128 Lowdin, P. O. ON THE NON-ORTHOGONALITY PROBLEM CONNECTED WITH THE USE OF ATOMIC WAVE FUNCTIONS IN THE THEORY OF MOLECULES AND CRYSTALS. *J. Chem. Phys.* **18**, 365-375, (1950).

129 Kjelstrup-Hansen, J., Norton, J. E., da Silva, D. A., Bredas, J. L. & Rubahn, H. G. Charge transport in oligo phenylene and phenylene-thiophene nanofibers. *Organic Electronics* **10**, 1228-1234, (2009).

130 Kuo, M.-Y., Chen, H.-Y. & Chao, I. Cyanation: Providing a three-in-one advantage for the design of n-type organic field-effect transistors. *Chemistry-a European Journal* **13**, 4750-4758, (2007).

131 Hutchison, G. R., Ratner, M. A. & Marks, T. J. Hopping transport in conductive heterocyclic oligomers: Reorganization energies and substituent effects. *Journal of the American Chemical Society* **127**, 2339-2350, (2005).

132 Noh, Y. Y. & Kim, D. Y. Organic phototransistor based on pentacene as an efficient red light sensor. *Solid-State Electron.* **51**, 1052-1055, (2007).

133 Wang, X. H., Wasapinyokul, K., De Tan, W., Rawcliffe, R., Campbell, A. J. & Bradley, D. D. C. Device physics of highly sensitive thin film polyfluorene copolymer organic phototransistors. *Journal of Applied Physics* **107**, (2010).

134 Huang, J. S. & Kertesz, M. Validation of intermolecular transfer integral and bandwidth calculations for organic molecular materials. *J. Chem. Phys.* **122**, (2005).

135 Chang, S., Chung, M. H., Kwon, J. H., Shin, S. I., Oh, T. Y., Dong, K. Y., Lee, S. J., Cho, K. H., Nahm, S. & Ju, B. K. Low-Voltage-Driven Pentacene Thin-Film Transistors with Cross-Linked Poly(4-vinylphenol)/High-k Bi5Nb3O15 Hybrid Dielectric for Phototransistor. *Journal of Nanoscience and Nanotechnology* **12**, 3355-3359, (2012).

136 Hutchison, G. R., Ratner, M. A. & Marks, T. J. Intermolecular charge transfer between heterocyclic oligomers. Effects of heteroatom and molecular packing on hopping transport in organic semiconductors. *Journal of the American Chemical Society* **127**, 16866-16881, (2005).

137 Bromley, S. T., Mas-Torrent, M., Hadley, P. & Rovira, C. Importance of intermolecular interactions in assessing hopping mobilities in organic field effect transistors: Pentacene versus dithiophene-tetrathiafulvalene. *Journal of the American Chemical Society* **126**, 6544-6545, (2004).

138 Sokolov, A. N., Atahan-Evrenk, S., Mondal, R., Akkerman, H. B., Sanchez-Carrera, R. S., Granados-Focil, S., Schrier, J., Mannsfeld, S. C. B., Zoombelt, A. P., Bao, Z. N. & Aspuru-Guzik, A. From computational discovery to experimental characterization of a high hole mobility organic crystal. *Nature Communications* **2**, (2011).

139 Cornil, J., Calbert, J. P. & Bredas, J. L. Electronic structure of the pentacene single crystal: Relation to transport properties. *Journal of the American Chemical Society* **123**, 1250-1251, (2001).

140 Mattheus, C. C., Dros, A. B., Baas, J., Meetsma, A., de Boer, J. L. & Palstra, T. T. M. Polymorphism in pentacene. *Acta Crystallographica Section C-Crystal Structure Communications* **57**, 939-941, (2001).

141 Gruhn, N. E., da Silva, D. A., Bill, T. G., Malagoli, M., Coropceanu, V., Kahn, A. & Bredas, J. L. The vibrational reorganization energy in pentacene: Molecular influences on charge transport. *Journal of the American Chemical Society* **124**, 7918-7919, (2002).

142 Cornil, J., Lemaur, V., Calbert, J. P. & Bredas, J. L. Charge transport in discotic liquid crystals: A molecular scale description. *Advanced Materials* **14**, 726-+, (2002).

143 Deng, W. Q. & Goddard, W. A. Predictions of hole mobilities in oligoacene organic semiconductors from quantum mechanical calculations. *J. Phys. Chem. B* **108**, 8614-8621, (2004).

144 Lemaur, V., Da Silva Filho, D. A., Coropceanu, V., Lehmann, M., Geerts, Y., Piris, J., Debije, M. G., Van de Craats, A. M., Senthilkumar, K., Siebbeles, L. D. A., Warman, J. M., Bredas, J. L. & Cornil, J. Charge transport properties in discotic liquid crystals: A quantum-chemical insight into structure-property relationships. *Journal of the American Chemical Society* **126**, 3271-3279, (2004).

145 Hannewald, K. & Bobbert, P. A. Anisotropy effects in phonon-assisted charge-carrier transport in organic molecular crystals. *Physical Review B* **69**, (2004).

146 Stojanovic, V. M., Bobbert, P. A. & Michels, M. A. J. Nonlocal electron-phonon coupling: Consequences for the nature of polaron states. *Physical Review B* **69**, (2004).

147 Demiralp, E. & Goddard, W. A. Structures and energetics study of tetrathiafulvalene-based donors of organic superconductors. *J. Phys. Chem. A* **101**, 8128-8131, (1997).

148 Balzer, F., Pogantsch, A. & Rubahn, H. G. Temperature dependent analysis of three classes of fluorescence spectra from p-6P nanofiber films. *Journal of Luminescence* **129**, 784-789, (2009).

149 Piaggi, A., Lanzani, G., Bongiovanni, G., Mura, A., Graupner, W., Meghdadi, F., Leising, G. & Nisoli, M. Emission properties of para-hexaphenyl polycrystalline films. *Physical Review B* **56**, 10133-10137, (1997).

150 Hanwell, M. D., Madison, T. A. & Hutchison, G. R. Charge Transport in Imperfect Organic Field Effect Transistors: Effects of Explicit Defects and Electrostatics. *Journal of Physical Chemistry C* **114**, 20417-20423, (2010).

151 Kalinowski, J. Electronic processes in organic electroluminescence, in: Miyata, S., Nalwa H.S. (Eds.). *Organic electroluminescent materials and devices, OPA, Amsterdam*, 1-72, (1997).

152 Hamadani, B. H., Corley, D. A., Ciszek, J. W., Tour, J. M. & Natelson, D. Controlling charge injection in organic field-effect transistors using self-assembled monolayers. *Nano Letters* **6**, 1303-1306, (2006).

153 Lu, X. F., Majewski, L. A. & Song, A. M. Electrical characterization of mica as an insulator for organic field-effect transistors. *Organic Electronics* **9**, 473-480, (2008).

154 Matsumoto, A., Onoki, R., Ueno, K., Ikeda, S. & Saiki, K. Fabrication of an organic field-effect transistor on a mica gate dielectric. *Chemistry Letters* **35**, 354-355, (2006).

155 He, Y. D., Dong, H. L., Meng, Q., Jiang, L., Shao, W., He, L. F. & Hu, W. P. Mica, a Potential Two-Dimensional-Crystal Gate Insulator for Organic Field-Effect Transistors. *Advanced Materials* **23**, 5502-+, (2011).

156 Low, C. G. & Zhang, Q. Ultra-thin and Flat Mica as Gate Dielectric Layers. *Small* **8**, 2178-2183, (2012).

157 Thilsing-Hansen, K. Growth and integration of organic nanofibers in devices. *University of Southern Denmark, Ph.D. Thesis*, (2010).

158 Kjelstrup-Hansen, J., Tavares, L., Hansen, R. M. D., Liu, X. H., Bordo, K. & Rubahn, H. G. Optical properties of microstructured surface-grown and transferred organic nanofibers. *Journal of Nanophotonics* **5**, 05170, (2011).

159 Tavares, L., Kjelstrup-Hansen, J. & Rubahn, H. G. Localized and guided electroluminescence from roll printed organic nanofibres. *Nanotechnology* **23**, 425203, (2012).

160 Hansen, R. M. d. O., Kjelstrup-Hansen, J. & Rubahn, H.-G. Light-emission from in-situ grown organic nanostructures. *Proceedings of SPIE* **8102**, 81020M, (2011).

161 Huisman, C. L., Huijser, A., Donker, H., Schoonman, J. & Goossens, A. UV polymerization of oligothiophenes and their application in nanostructured heterojunction solar cells. *Macromolecules* **37**, 5557-5564, (2004).

162 Simbrunner, C., Quochi, F., Hernandez-Sosa, G., Oehzelt, M., Resel, R., Hesser, G., Arndt, M., Saba, M., Mura, A., Bongiovanni, G. & Sitter, H. Organic-Organic Heteroepitaxy of Red-, Green-, and Blue-Emitting Nanofibers. *Acs Nano* **4**, 6244-6250, (2010).

163 Yassar, A., Horowitz, G., Valat, P., Wintgens, V., Hmyene, M., Deloffre, F., Srivastava, P., Lang, P. & Garnier, F. EXCITON COUPLING EFFECTS IN THE ABSORPTION AND PHOTOLUMINESCENCE OF SEXITHIOPHENE DERIVATIVES. *Journal of Physical Chemistry* **99**, 9155-9159, (1995).

164 Goldmann, C., Haas, S., Krellner, C., Pernstich, K. P., Gundlach, D. J. & Batlogg, B. Hole mobility in organic single crystals measured by a "flip-crystal" field-effect technique. *Journal of Applied Physics* **96**, 2080-2086, (2004).

165 Takeya, J., Goldmann, C., Haas, S., Pernstich, K. P., Ketterer, B. & Batlogg, B. Field-induced charge transport at the surface of pentacene single crystals: A method to study charge dynamics of two-dimensional electron systems in organic crystals. *Journal of Applied Physics* **94**, 5800-5804, (2003).

166 de Boer, R. W. I., Jochemsen, M., Klapwijk, T. M., Morpurgo, A. F., Niemax, J., Tripathi, A. K. & Pflaum, J. Space charge limited transport and time of flight measurements in tetracene single crystals: A comparative study. *Journal of Applied Physics* **95**, 1196-1202, (2004).

167 Weis, M., Lin, J., Taguchi, D., Manaka, T. & Iwamoto, M. Insight into the contact resistance problem by direct probing of the potential drop in organic field-effect transistors. *Applied Physics Letters* **97**, (2010).